ELONGATIONAL FLOW EXFOLIATION OF GRAPHITE IN A NOVEL SINGLE SCREW BATCH MIXER DESIGNED FOR CONTINUOUS CHEMICAL FUNCTIONALIZATION

By

JUSTIN WALLACE HENDRIX

A dissertation submitted to the

School of Graduate Studies

Rutgers, The State University of New Jersey

In partial fulfillment of the requirements

For the degree of

Doctor of Philosophy

Graduate Program in Chemical and Biochemical Engineering

Written under the direction of

Thomas J. Nosker

And approved by:

_____

_____

_____

_____

New Brunswick, New Jersey

October, 2020

Abstract of the Dissertation

Elongational Flow Exfoliation of Graphite in a Novel Single Screw Batch Mixer Designed for Continuous Chemical Functionalization

By Justin W Hendrix

Dissertation Directors: Professor Nosker & Professor Masanori Hara

Graphene has been publicized as the next generation material of this millennium. In the past two decades, the 2D material has been researched for use in such applications as thermal management, environmental remediation, biotechnology, and lightweight, structural materials, due to its exceptional mechanical properties. Exfoliation methods have already been developed for the production of un-oxidized graphene flakes, including electrochemistry, chemical oxidation and expansion, and liquid phase synthesis. All these approaches eventually yield graphene, but at a tremendous sacrifice to cost, process complexity, and desired properties. Majority of these methods create graphene by the use of a multistep processes, and produce harmful byproducts due to extraction from wasted matrices. As a consequence, defects are often introduced within the surface, which greatly diminish their properties. The key challenge is finding a de-convoluted process

competitive enough to reduce cost and maintain pristine structure through all developing stages.

Under high speed extensional flow of graphite and a high polymer matrix, the conditions to fully convert many layered graphite to graphene can be done in-situ. A novel process invented by Nosker *et al*., using extensional flow, allows for a polymer matrix and graphitic filler to undergo unique deformations of extension and exfoliation, respectively. Based on the experimental conditions, the polymer experiences a transition from a complex random walk network of chains to a fully stretched detangled array with an elongated conformation. This results in a polymer with an increase in potential energy and exposure of its chemical side groups. Under the same field, the graphite undergoes an exfoliation mechanism dominated by free radicalization via erosion, fragmentation, and diffusion leading to few and many layer graphene flakes. These conditions create two or more high surface areas, in-situ, that provided functionalization of chemically desirable sights. The process herein, yields a scalable method of producing functionalized graphene with unique properties by a continuous mixing process. Within this work, an experimental study of the complex phenomena undergone by both the polymer and created graphene are investigate. Analyzing a combination of the mixing process, composite interface, and morphology we will seek to expand our knowledge on new complex graphene composite systems.

DEDICATION

To my wife Zhi-Yin, thank you for your compassion, patience, and belief in me.

To my family; my mother, my brother, and my aunt Tracey

To my friends; Rusty, and all those who've stayed with me through this long arduous journey

Thank You

ACKNOWLEDGEMENTS

Here, I'd like to express my deepest gratitude to my defense committee co-chaired by both Professor Thomas Nosker and Professor Masanori Hara, and including members Dr. Thomas Emge, and Professor Fernando Muzzio.

I'd especially like to thank Professor Nosker and Dr. Jennifer Lynch for being extremely patient and an insightful presence through this extremely daunting journey. Thank you for starting me on this path, exposing me to the world of polymers. Through your training, your comments to scientific communication, and opportunities, you've helped shape me to be the researcher I am today.

I'd like to thank Dr. Gordon Chiu for being the life-blood of this research. You are the foundation and inspiration that birthed this work and my way of thinking.

Dr. Emge, through our conversations, your expertise, and your professionalism, you've made me a better researcher. I could not have made the steps to the finish line without your guidance.

I’d like to thank Dr. Richard Lehman and Dr. Lisa Klein for providing me the initial opportunity to pursue my graduate work. You’ve provide me with the space and process to make all this possible.

I’d finally like to thank Dr. Charlie Roth for providing me the continued opportunity.

…Thank you all

List of Notations and Abbreviations

s	seconds
min	minutes
m	meters
nm	nanometers (10^{-9} m)
Pa	Pascal
J	Joules
kJ	kilojoules (10^{3} J)
K	Kelvin
C	Celsius
g	grams
kg	kilograms (10^{3} g)
N	Newtons
eV	electron Volts
mol	moles
V	Velocity (s^{-1})
$\dot{\gamma}$	Shear rate (s^{-1})
$\dot{\gamma}_{zx}$	Shear rate from z-axis in the direction of the x-axis (s^{-1})
$\dot{\varepsilon}$	Strain rate (s^{-1})
$\dot{\varepsilon}_{xx}$	Strain rate from x-axis in direction of the x-axis (s^{-1})
$\dot{\varepsilon}_{zz}$	Strain rate from z-axis in direction of the z-axis (s^{-1})
p	Viscous ratio (dimensionless)
μ_D	Dynamic viscosity of dispersive phase (Pa·s)
μ_C	Dynamic viscosity of continuous phase (Pa·s)
Ca	Capillary number (dimensionless)
Ca_{crit}	Critical capillary number (dimensionless)
μ	Dynamic Viscosity (Chapter 3) (Pa·s)
R_d	Droplet radius (m)

σ	Surface Energy ($J \cdot m^{-2}$)
F	Hydrodynamic force (Newtons N)
T	Temperature (°C)
k_B	Boltzmann constant; 1.3806 x 10^{-23} ($m^2 \cdot kg \cdot s^{-2} \cdot K^{-1}$)
N	Number of chain segments
l	Chain segment length (nm)
R	Root mean square size (m)
dR	Change in radius (Chapter 3) (m)
dS	Change in entropy ($J \cdot K^{-1}$)
F^D	Drag Force (N)
ζ	Polymer chain size (dimensionless)
ζ_{coil}	Coiled polymer chain size (dimensionless)
η	Shear viscosity (Pa·s)
ζ_{rod}	Extended polymer chain size (dimensionless)
L	Current polymer chain length (m)
d	Maximum chain length (m)
λ	Wavelength of electro-magnetic waves (nm)
E	Energy of an electron (eV)
θ	Angle of incident electron (degrees °)
d	Interplanar distance of diffracted (nm)
D	Crystalline domain size (nm)
K	Shape factor (Scherrer equation) (dimensionless)
β	Half height width in 2θ (degrees °)
ΔHm	Melting enthalpy ($J \cdot g^{-1}$)
ΔHm_{100}	Melting enthalpy for 100% crystalline sample ($J \cdot g^{-1}$)
Q	Heating rate (°C/ min)
F_{hydro}	Hydrodynamic force (N)
r	End-to-end length of a polymer chain (m)
$F_{elastic}$	Elastic force (N)
N	Number of freely joined segments

a	Segment length meter (m)
F_{con}	Conservative force (N)
dU	Change in potential energy (Also ΔU) (J)
dx	Displacement (m)
W	Work (J)
T_g	Glass transition temperature (K)
T_r	Recrystallization temperature (K)
T_m	Melting temperature (K)
c	Conversion
k	Kinetic constant (s^{-1})
k_0	Initial kinetic constant (s^{-1})
k (T)	Kinetic constant as a function of temperature (s^{-1})
$f(x)$	Conversion as a function of reaction displacement
Ea	Activation energy ($kJ \cdot mol^{-1}$)
R	Gas constant (Chapter 6 & 8); 8.314 ($J \cdot K^{-1} \cdot mol^{-1}$)

Table of Contents

Table of Figures

Table of Tables

Chapter 1 Introduction

Graphene has been publicized as the leading edge material of this millennia. In the past two decades, the 2-D material has been considered for use in applications, such as thermal management [1], environmental remediation and filtration [2] [3], biotechnology [4] [5], and lightweight, structural materials [6]; due to its exceptional mechanical properties [7]. Many exfoliation methods have been developed to separate graphene from graphite and produce un-oxidized graphene flakes, including electrochemical [8] [9], chemical oxidation and expansion, [10] [11] and liquid phase [12] [13]. However, these approaches are costly multistep methods that use or produce harmful byproducts. Since the graphene is often extracted from a sacrificial medium, defects are often introduced on the graphene surfaces and edges, which may reduce some properties [14] [15]. The challenge is finding a viable, inexpensive, less complex process that permits property retention.

1.1 Aim

Melt mixing of composites, compared to solvent mixing or dispersion reaction polymerization, has been found to be more economical due to the lack of solvent and is currently use in common industrial techniques. The process involves taking a polymer melt and filler particles and mixing the components under a high shear environment. The high shear in an industrial mixing process imparts stresses on the filler to break the constituents apart and disperse them throughout the matrix. Although this is available, current (conventional) melt mixing technologies do not provide the same level of exfoliation and functionalization, compared to the lab scale niche process we used in these studies.

1.2 Strategy

Our research has found the presence of high speed extensional flow fields as being a fundamental driver to the creation of graphene from graphite. Under significant extensional flow, a polymer matrix may fully convert graphite to few layer and many layer graphene in-situ. The extensional flow provides the conditions that allow internal shear stress to exceed the planar shear yield stress in graphite. These kinds of stresses generate graphene that is functionalized, creating covalently and non-covalently bonded graphene polymer matrix composites (G-PMC). Under extensional flow, the polymer and the graphitic material undergo unique deformations of single chain elongation and exfoliation respectively. Depending on the condition, the polymer experiences a transition from a large globule to a fully stretched chain, leading to an increase in surface area and exposure of chemical side groups. Under the same field, the graphite/graphene components undergo a separation mechanism of erosion and fragmentation, leading to variable layer graphene flakes. These conditions create two high surface area regions *in situ* that allow functionalization of chemically desirable sights. In summary, this process yields a scalable method of producing functionalized graphene with unique properties by a continuous “melt mixing” process.

Chapter 2 Background

2.1 Context of exfoliation in polymer composites

2.1.1 Plastic processing techniques

There are a few factors contributing to material advancement and adaptation for engineering applications. The most dominant contributions are the intrinsic properties of the starting material and the scalability during process development. Intrinsic properties include high mechanical strength, low weight, good thermal stability, low cost, and corrosion resistance. In process scalability, versatility, reduction in complexity, and high yield are the ultimate goals [16]. In plastic processing, the motivating factor is to increase material utility. One of the leading methods to increase utility is to compound virgin polymer with a filler or reinforcing agent at high weight percentages. The purpose of this operation is to improve the intrinsic properties of virgin polymers, particularly stiffness, or modulus. Low Stiffness is the main shortcoming polymers have relative to traditional engineering materials. Improving stiffness thus provides a new or specialized property that gives an adding value to the final product [17].

Compounding is a mixing process which distributes and disperses a reinforcing agent into a finished composite blend. This is usually done continuously, or through a one pot batch process. Continuous processes occur by single or twin screw extrusion, where resin and filler are mixed from a solid form that is conveyed down a barrel in the molten state [18]. The molten material exits a die of a particular shape, or enters a mold for a final form. For a batch process, molten material is distributed and dispersed for a set mixing time in a chamber. The material is continuously mixed until an adequate dispersion is

achieved. The final product of the batch process is then emptied from the mixer, and then thermally formed to a desired the shape.

Each of these methods have benefits and deficiencies which can be exploited based on the desired product. Batch processing offers reduced complexity and the ability to achieve optimal mixing by longer mixing times. However, for conventional batch processes, optimization times for high yield exfoliation are often too long. This leads to polymer matrix degradation and longer production times, when incorporated into a continuous compounding line. Continuous mixers offer higher throughput and greater product uniformity. However, they can fail to properly disperse the reinforcing agent, due to short residence times and improper feeding, and may lead to compositing constituents that are not optimally reinforced. This situation provides an opportunity for a continuous compounding method that is able to reduce the time to effectively distribute and disperse the filler.

2.1.2 Composites and their application

Compounded polymer composites find applications where weight can be reduced without the sacrifice of performance. In our research, high performance polymers were selected based on the ability of their properties to be augmented to function as a substitute for metals or alloys for large-scale engineered applications. One of the engineering areas where consistent advancements have taken place is the automotive industry. This industry is continuously looking for ways to improve performance while finding more efficient alternative materials. Two examples of polymer composite matrices that are currently being researched as metal replacements are nylon (PA66) and polyphenylene sulfide (PPS).

2.1.2.1 Nylon Composites

Nylon Composites have a history of replacing steel and aluminum manufactured items, where the strength to weight is important to performance. These material replacements are often found in automotive, aerospace, and sporting goods industries. Items like electrical interconnects, fuel/air manifolds, and panels are initially replaced, resulting in an improved fuel efficiency. The most steadily used composites have contained nanoclay. Nanoclays are of particular interest due to their inherently benign (insulating) properties, abundance, and cost to property enhancement, when compared to virgin material [19]. Historically, Toyota since the 1980s, have contributed a tremendous financial stake in nanoclay/nylon containing composites. They have been in use due to their increased tensile strength and operation temperature compared to virgin nylon. They found that with a 5% by weight of nanoclay addition, the materials and processing performances are improved [20]. These nylon composites have been able to offer a 25% weight reduction compared to fiberglass automotive polymer composites while maintaining a competitive cost. In under the hood applications, these composites provide an increased thermal distortion temperature, offering some degree of heat resistance [21].

2.1.2.2 Polyphenylene Sulfide composites

A polymer composite that has a higher thermal operation temperature and dimensional stability than nylon is Polyphenylene Sulfide (PPS) composite. PPS automotive composites are typically used in locations where they are in constant contact with fuel [22]. These composites are typically 40 % glass fiber filled PPS, and are used where closer mechanical tolerances are necessary. PPS composites are still relatively new

in the automotive industry, which suggest these materials have room for improvement. A 40% fiberglass filled PPS is stiff, but very brittle and heavier, due to its fiber glass filler. Studies have shown that constant exposure to solvents can weaken the bonds between the fiberglass-PPS matrix. This can cause substantial property reduction [23]. Also, PPS filled with graphite and other 2D inorganic filler has yet to provide substantial property improvements [24]. Most require the use of a low concentration of modified filler, which still lack decent mechanical properties.

2.1.2.3 Polysulfone composites

Polysulfone (PSU,) is an interesting class of material due to its high glass transition temperature, oxidative resistance, and ability to form nanosized pores [25]. Composites of its design have been studied, and are reported to have a huge impact in membrane engineering for the fine separation of liquids and gases[26]. There have already been uses of pure PSU in ultrafiltration systems for waste water treatment [27], but improving these materials by compositing offers opportunities in inexpensive, clean water [28].

2.1.3 Ty pes of filler material

Polymers can typically be compounded with any micro, or nanosized filler, many of which can offer reasonable property improvements. Powders were the first type of material that were used to add stiffness, conductivity and [29] UV-absorption (carbon black or metal oxide powders). Powder-filled composites typically offered static stiffness properties but are extremely brittle under tensile stress. Fibers (glass fibers ,carbon fibers, or nanofibers) are the most widely used to impart added strength and stiffness, but initial costs are higher for these composite materials [30] [31]. From these materials, we find that an inexpensive filler with a significant aspect ratio is ideal. 2-D mineral fillers

offer the advantage of having anisotropic material properties, high availability, and lower cost. Of these types of filler, nanoclay and graphite (graphene precursor) are most widely used for their competitive cost and reinforcement properties.

Nanoclay have been often used in due to their relative availability, high surface (750 m^2/g) area and moderate strength [32] [33] . There are two classes of nanoclay known to be available; the first are organophilic clays, which contain Na+ as an interlamellar cation, and polycationic, which use Ca2+ as the main interlamellar cation. This cationic behavior make the clay either polar (Na+) or nonpolar (Ca2+), with surface chemistry of the matrix forming materials playing a strong role in resulting properties. Nanoclay, like graphite, are 2D yet have a much larger c-axis spacing that is 3 times as wide. This makes orienting and exfoliating, in plastic processing easier due to this characteristic. Polar clays containing Na+ are often modified with ammonium containing salts, to make them miscible in nonpolar polymer [34]. Nylons, being that they contain a polar amide group in their polymer backbone, provide them an inherent miscible with clays. Historically, Toyota has benefited from this idea, where most these composites are found in in automotive application for nonpolar polymer like Polystyrene (PS) surface modification of the nanoclays has been a requirement for improved properties. In the last few years compatibilizers for nonpolar polymers and polar nanoclay have been found to not be a requirement under extremely high shear. The high shear environment was found to be enough to increase diffusion and size reduction of the nanoclay, without chemical modifiers [35] [36] [37].

Graphite is a 3D allotrope of elemental carbon arranged in a hexagonal crystal lattice. Within the basal planes of the lattice, each carbon atom is covalently bonded to

three neighboring carbon atoms. The fourth bonded electron per carbon atom is weakly bound to carbon atoms above or below this plane by van der Waals (VDW) forces. Fluid force applied by molten polymer, in our case, are applied perpendicular to the VDW force; causing these planes to shift. This results in the modifying of the stacking of the VDW connected planes to one of two motifs that leads to one of two crystal structures, namely, the hexagonal and rhombohedral phases. Hexagonal graphite has the plane stacking sequence of ABABAB while Rhombohedral has ABCABC stacking. Of these two motifs, the hexagonal is considered the more stable structure, with the rhombohedral structure often created by mechanical grinding or other applied pressure [38]. Thus, the weakly bonded VDW planes are easy to separate by shearing.

When the 3D graphite structure is reduced to mostly 2D layers, creating a high surface area (640-1500 m^2/g) and high modulus (~ 1TPa) material, it is called graphene [39]. Graphene is proposed to have free delocalized π-bond electrons which comprise the valence and conduction bands of graphene [40]. Unlike graphite, which is a narrow band gap semiconductor, graphene has valence and conduction bands that connect at the Dirac point [41] . In other words, when the valence and conduction bands touch, the resulting material has no band gap. This lack of a band gap gives graphene semi-metal properties, including high electron mobility.

2.2 Fundamentals of polymeric flow

To understand plastic compounding, it is important to first understand the practices used in mixing to disperse and distribute a reinforcing phase. By exploiting the fundamentals of mixing, a new class of materials were created, resulting in a patented

process [42]. By analyzing these fundamentals of this process, an improved foundational understanding can be attained on how new composites can be developed.

2.2.1 Shear Flow (Couette) vs Elongational Flow (Irrotational)

Some of the earliest experimental and theoretical work in fluid flow of two immiscible liquids was pioneered by Taylor in his experiments with droplet suspension breakup in a dilute medium of dissimilar viscosity[43]. Taylor designed two methods to observe droplet deformation contributing to a difference in mechanism of deformation. The first consisted of two counter moving surfaces creating planar shear flow.
The shear flow tensor shown in (1) describing the velocity field as V, experienced by the droplet.

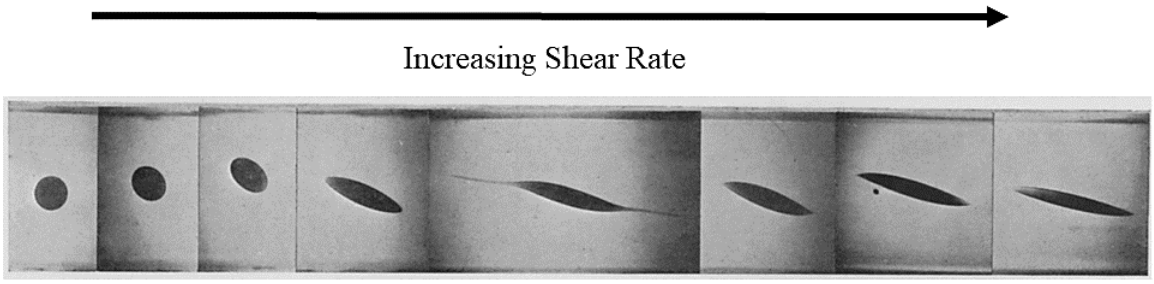

Figure 2-1 Parallel band/plate droplet deformation (Taylor)

$$V = \dot{\gamma} \begin{pmatrix} 0 & 0 & 0 \\ 0 & 0 & 0 \\ 1 & 0 & 0 \end{pmatrix} = \dot{\gamma}_{zx} \quad (1)$$

From this first experimental setup at maximum roller speed, the shear stress $\dot{\gamma}$ perpendicular to the x direction $\dot{\gamma}_{zx}$, the droplet deformed to a spheroid that distorted without breaking, in Figure 2-1. The second experiment conducted defined the velocity field V, of a four roll apparatus producing planar elongational flow under the same matrix conditions. What's observed was droplet extension at a particular strain rate $\dot{\varepsilon}$ occurred

by a strain rate increase in the direction $\dot{\varepsilon}_{xx}$ parallel to the direction of deformation. This lead to a change in rate of deformation, normal to the deformation plane $\dot{\varepsilon}_{zz}$. The extension lead to droplet rupture and breakage in (2), Figure 2-2.

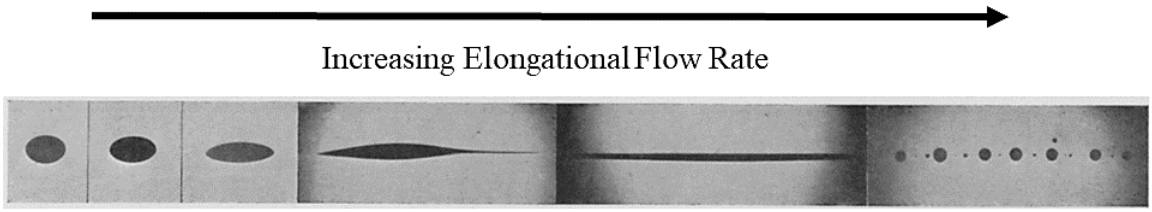

Figure 2-2 Four Roller apparatus for droplet deformation (Taylor)

$$V = \dot{\varepsilon} \begin{pmatrix} 1 & 0 & 0 \\ 0 & 0 & 0 \\ 0 & 0 & -1 \end{pmatrix} = \dot{\varepsilon}_{xx} - \dot{\varepsilon}_{zz} \tag{2}$$

Taylor found the mechanism for breakage of droplets to be related to apparent differences in kinematic viscosity ratio defined by p to a droplets critical deformability, where μ_D is the viscosity of the dispersed phase and $\mu_{C,}$ the viscosity of the continuous phase.

$$p = \frac{\mu_D}{\mu_C} \tag{3}$$

The critical deformability was found to work, but only up to a maximum viscous ratio of 4. Similar results were confirmed by Rumscheidt and Mason of this critical viscosity ratio to deformation [44], suggesting that beyond this critical viscosity exist no deformation and breakage of droplets. An expansion of work conducted by Taylor & Rumscheidt work done by Grace produced a slightly different view on the viscous ratio. For droplet deformation leading to breakage , Grace found that a specific deformation

rate above a critical capillary value Ca_{crit} was needed, where $Ca_{crit} < Ca$ [45] .The capillary number Ca represents the ratio of the viscous force of the matrix to the restorative force of the dispersed phase to deformation or shear, where μ is the kinematic viscosity , $\dot{\gamma}$ is the shear rate , σ interfacial tension, and R_d the droplet radius (4) .

$$Ca = \frac{\mu R_d \dot{\gamma}}{\sigma} \tag{4}$$

Associating 2-D elongational flow to Simple shear flow, Grace found the critical capillary number to be smaller for the case of 2-D elongational flow. Leaving for simple shear, the critical capillary number for breakage approaching a near infinite value as the viscous ratio exceeds p > 1 in Figure 2-3 [46]. This forms the bases of 2D elongational flow as being essential for particulate breakup and deformation, based on the idea of it being seemingly independent of viscosity. This viscous independence suggests that any material system, that undergoes deformation by the application of stress, has the potential to create new surfaces. These systems include liquid-liquid in Graces work, and solid-liquid systems. Particularly for solids that deform by shear stress under an inherent slip plane, like graphite.

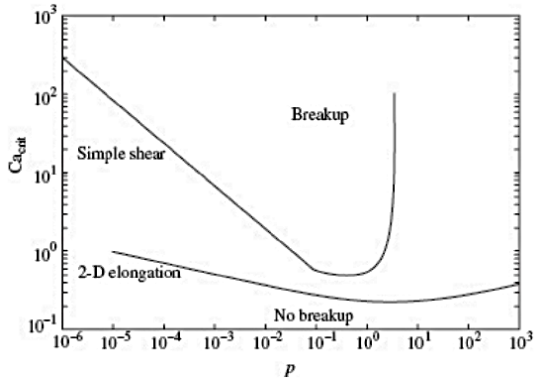

Figure 2-3 Capillary number Ca vs viscous ratio p [24]

2.2.2 Deformation of Polymers under flow conditions

Research has shown that under elongational flow, long chain polymers begin to stretch and elongate. Models suggest that based on size of the long chain polymer, there exists a shear transition from large globules to a fully stretched chain [47, 48]. For extension of single polymers, the force to stretch these long chains are preceded by a hydrodynamic drag force, imposed to deform a coiled state structure. A chain only then becomes uncoiled when the drag force as friction exceeds the entropic elastic restorative force[49, 50], given by De Gennes.

The extension of a coiled polymer chain contains an entropic driving components under elongation force. The entropic component stems from the fundamental understanding of the elasticity of a rubber band, as it stretches uniaxially. The polymer chains want to maintain an equilibrium unstretched state containing a random network of coils, $dR = 0$. As polymer coils are stretched dR, the degree of freedom and a change in entropy occurs, $dS \neq 0$. In the case of polymers, the change in entropy per extension is related to the force to extend the polymer chain (5) [51].

$$F = T\left(\frac{dS}{dR}\right) = \left(\frac{3Tk_B}{Nl^2}\right)R \tag{5}$$

In (5), T is the absolute temperature of extension, k_B is the Boltzmann constant, N is the number of chain segments, l is the segment length, and R represents the root mean square size ($R = \sqrt{6}\,R_G$, R_G is the radius of gyration) of a polymer coil. The hydrodynamic force interacting on the polymer chain acts as a resistive force due to viscosity of the flow

medium. The resistance behaves as shear on the surface as a force of drag, separating the polymer segments and reducing the effects by the inter-chain components [52].

The simplest model for the representation of (5) and the polymers response to drag is the dumbbell model. This model is coined the elastic dumbbell, and assumes the polymer chain as component weights attached by a centralized harmonic spring [53]. The force of drag from stokes law F^D (6), where V is the velocity of the surrounding media, T is the absolute temperature, ζ is the polymer chain size, and $k_B$the Boltzmann constant, produces a resistive force opposite to the direction of motion in the form of a hydrodynamic frictional force.(Table of notation)

$$F^D = \zeta k_B T V \tag{6}$$

$$\zeta_{coil} k_B T = \frac{3}{8}\sqrt{6\pi^3}\eta R \tag{7}$$

$$\zeta_{rod} k_B T = \frac{2\pi L \eta}{\ln(\frac{L}{d})} \tag{8}$$

In the size of the coiled state ζ_{coil} (7), where η is the viscosity and R is the root mean square size of the molecule, the drag coefficient is proportional to the radius of the molecule. The proportionality in R, given that in a fluid system force moves in the advantage of reducing drag [54] produces a favorable reduction in R. For an elongated rod of the e size ζ_{rod}, the drag coefficient of the molecule scales proportionally with the length L vs the log ratio of the Length L to maximum chain length d (8), for finite sized molecules [55]. The same interpretation rings true, where a reduction in length or diameter produces both an increase in drag as extension takes place.

Representing length L and d of real chain polymers are complicated to interpret, when considering all the interactive forces and side groups. An even more simplified

model is used to understand an elongated or deformed polymer chain as a tube of uniform surface, neglecting the complexity of bond angle and side group chemistries. This persistently useful model used for both synthetic and biobased polymers is the Wormlike Chain Model (WLC) [56]. This model takes a polymer as a collection of freely joined semi-flexible chains, interpreted as a space curve characterized by a contour length and stiffness [34]. Other, more complicated models exist, that describe in more detail, the elastic nature of polymer but WLC provides the simplest interpreting approach. While under an extensional flow field, the wormlike chain model attempts to resolve issues of complex side chains of high polymers [57]. However, all these models fail to predict the capabilities of what is really occurring in high molecular weight synthetic engineering polymers [58]. By identifying the conditions and development of a fully extended synthetic chain, the optimal extension rate is found for many different polymers of varying chemistries and length.

2.2.3 Particle Breakup Mechanisms

Particulate breakup in shear vs elongational flow suggests a number of different mechanisms by fluid force to cause separation of large particles Figure 2-4. In steady shear flow particles deform, then rotate in the direction tangential to the hydrodynamic shear force. In extensional/elongational flow, these hydrodynamic forces pulling and orienting these elements into smaller parts, without a definitive limit. Researchers suggest two mechanisms for particle breakup include erosion and rupture. Erosion pertains to small instances of detachment of single particles from the outer surface, whereas rupture is the large scale fragmentation of aggregates into two or more parts [59] Figure 3-4b . In these two mechanisms, the driving forces are quite different. Particularly weak

agglomerations break up more easily by rupture whereas strong agglomerates exhibit erosion. In fragmentation studies with microfluidic devices, tests have been made by maintaining particles at stagnation points while increasing fluid flow. In the case of carbon nanotubes (CNT) it is been discovered that aspect ratio and size as the critical components in breaking up loosely agglomerated CNTs. Large particles break up easier, but as the sizes reduce, the critical stress component based on the extension rate increases [60] . In the case of Graphitic Nanoparticles , it is unclear whether erosion or rupture act as the initial mechanism for particulate breakup, Vilaverde suggests it depends on the initial size of the starting material[61].

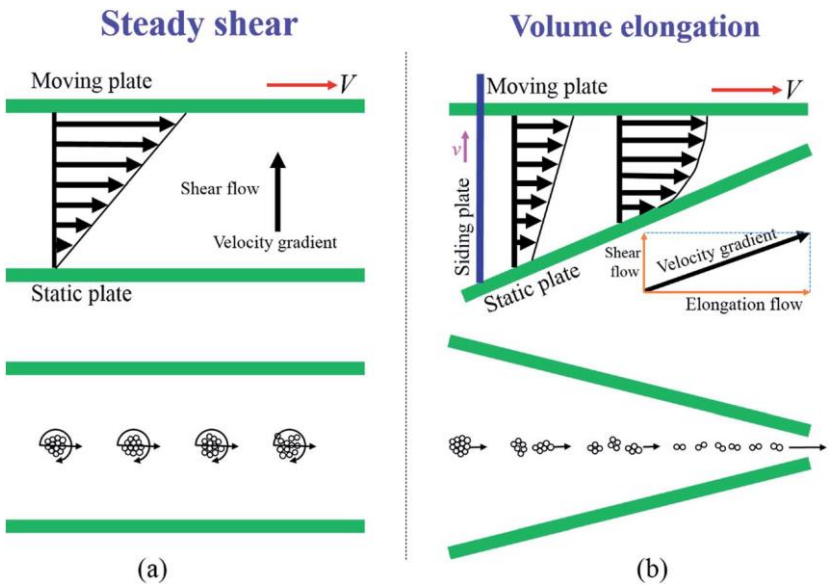

Figure 2-4 The schematic diagram of dispersing process for the nanoparticles in different flow fields: (a) steady shear flow; (b) volume elongational[40]

It is safe to suggest that the exfoliation and breakup of nanoclays could behave similarly to graphite, since they have a similar 2D structures and weak secondary bonds. Research in the exfoliation of nanoclays suggests a limit to mechanical size reduction of clay stacks. Once this limit is reached, exfoliation can only continue if the matrix has an affinity for the polymer chain. Affinity would cause the diffusion of a polymer chain into

the clay galleries and continue the rate of exfoliation [62]. In nanoclay composites, surfactants are often used to cause extended exfoliation to modify the chemical affinity of the clay [63]. This leads continued exfoliation being limited to diffusion. It has been suggested that the diffusion rate is similar to self-diffusion of the melt for nanoclay blends [64]. This suggests that by changing the system to increase the diffusion rate, exfoliation can be increased.

2.3 Types of functionalization

Even with a lot of different methods of creating graphene, applying its properties to a new composite material is a task that has yet to be overcome. One method that shows real promise is the process of functionalization. Functionalization in graphene is performed by changing the most characteristic feature of graphene, namely its surface structure, usually by changes to the chemistry of graphene [65]. The functionalized material forms a compatible interface that allow its nanoscale properties to be translated to the macroscale composite. In graphene, this is performed through methods that affect either covalent or noncovalent bonds at the surface.

2.3.1 Covalent Functionalization

Covalent functionalization of graphene is associated with a loss in π-π conjugation by the rehybridization of sp^2 carbons of the delocalized π network into sp^3 centers, leading to a modification of the inherent chemical and resulting physical properties[65]. For covalent functionalization, there exists two routes for graphene: (1) creation of highly reactive species like free radicals or dienophiles, and (2) formation of bonds between organic functional groups, including oxygen, as in graphene oxide

species[65]. This method can modify the surface of graphene, changing the degree and complexity of its chemical reactivity[66].

2.3.2 Noncovalent Functionalization

Alternatively , noncovalent functionalization provides chemical interactions without rehybridization or affecting the π network[67]. Noncovalent functionalization depends on the long-range strength of the electrons in the π-network creating attractive and repulsive forces between non-bonded neighboring atoms. These attractive and repulsive forces can be broken down into electrostatic, dispersive, inductive, and exchange-repulsive types. This route of functionalization does not lead to damage of the π structure or introduce electronic-based imperfections in the surface (minor dislocations are still possible). This allows for the retention of both the mechanical and general electronic features of graphene.

There have been many different routes in functionalizing graphene over the years, [68, 69] but a continuous method of production is still not available for realistically scalable applications. Also, none of the proposed methods of functionalization, or even graphene formation, appear to be green enough to produce a low levels of toxic chemical byproducts. A method without chemically undesirable techniques must be proposed as a scalable alternative.

In our synthesis of graphene from graphite, I've employed unique elongational flow fields to exfoliate graphene directly from mined graphite. By using a continuous polymer phase and a dispersed graphite phase, the mechanics of polymer breakup and extension were exploited to produce graphene *in situ*. By exfoliating *in situ*, using a novel elongational flow field, the resistive force to exfoliation was exceeded handily. By applying shear strain rates above 10^3 s^{-1}, scalable graphene reinforced composites with

improved interaction between the polymer and the created graphene were consistently produced.

Chapter 3 Methodology

3.1 Materials and Experimental

3.1.1 Graphite

In this research, flake mineral graphite was used (Asbury Carbons, mills grade 3627 with 95 % purity, diameter = 250 μm, ρ = 2.26 g/cm^3). To remove any surface contaminants produced in the purification process, the graphite was heated in an open air oven at 350 °C for 4 hours. The heat-treated graphite was placed in sealed glass jars prior to processing.

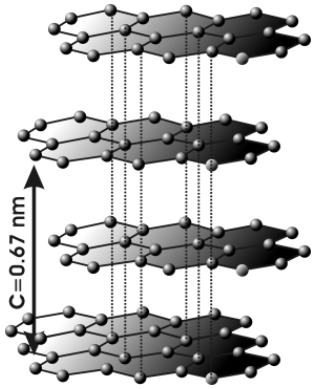

Figure 3-1 Graphite Atomic Structure

Table 3-1 Graphite Material Properties

Graphite (C)	
Density	2.26 g/cm^3
Water Absorption (24 hr, 23 °C)	0.05%
Tensile Modulus	3.4 Gpa
Tensile Stress	80 Mpa
Tensile Strain at Break	4%
Melting Temperature	3650 ° C
Thermal Conductivity (basal plane)	20 W/m/K

3.1.2 Polyamide 66 (PA66, Nylon)

PA66 is a high melt temperature polymer with an excellent strength to weight ratio [70]. PA66 is an unmodified semi-crystalline polymer, best used in a number of key consumer products. This polymer also was selected due to its current use in the automotive industry. In these experiments, Zytel 101 NC010 Polyamide 66 from DuPont, shown schematically in Figure 3-2, was purchased from PolyOne. This polymer was received as resin pellets with properties displayed in Table 1.

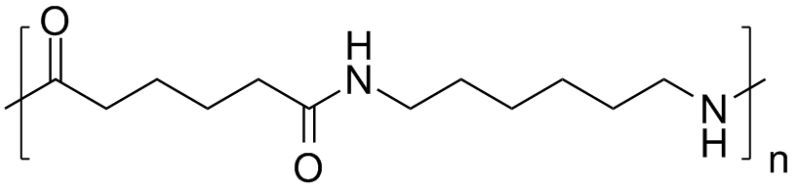

Figure 3-2 Polyamide 66 (PA66) Molecular Structure

Table 3-2 Polyamide 66 Material Properties

Polyamide 66 Zytel 101 (PA 66)	
Density	1.14 g/cc
Water Absorption (24 hr, 23 °C)	2.60 %
Tensile Modulus	3.1 Gpa
Tensile Stress	82 Mpa
Tensile Strain at Break	25%
Glass Transition Temperature (Tg)	60 ° C
Melting Temperature ™	262 ° C
Thermal Conductivity	0.16 W/m/K

PA66 is a high molecular weight polymer consisting of a monomer with a centralized amide group containing 6 ethylene chains per unit, and 6 carbon atoms on either side of the central amide bond. Polyamide is a condensation polymer, which is produced by first mixing of hexamethylenediamine ($C_6H_{16}N_2$) and adipic acid ($C_6H_{10}O_4$)

to produce nylon salt. The polymerization proceeds by the removal of water byproduct. The polymer notably forms hydrogen bonds between the amide groups upon cooling. Prior to mixing in these experiments, the polymer resin was dried in a vacuum oven for 4 hours at 90 ° C and stored in a sealed container to eliminate water.

3.1.3 Polyphenylene Sulfide (PPS)

PPS, like PA66, has a high crystalline melt point, but has a higher glass transition temperature and higher percent crystallinity. The advantage of PPS is due to its high stiffness and low coefficient of thermal expansion (CTE) which makes it useful in engineering applications where close tolerances are needed[71]. The polymer used in this research is polyphenylene sulfide (PPS) Ryton QA200N, purchased from Solvay Specialty Polymers. The monomer structure and properties are listed in Figure 3-3 and Table 4-3, respectively. PPS is a semi-crystalline polymer, commonly used in chemically resistant coatings. Due to the simplicity of the chemical structure, the polymer chain is very flexible, allowing for better adhesion as well as higher crystallinity compared to other thermoplastic polymers of its kind.

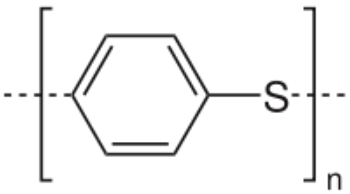

Figure 3-3 Polyphenylene Sulfide (PPS) Molecular Structure

PPS may be described as containing aromatic rings and sulfide bonds per unit. The resin is produced by the reaction of sodium sulfide with 1, 4-dichlorobenzene in an

N-methyl-2-pyrrolidone (NMP) solvent. The resin is capable of forming cross-links due to the reactivity of the sulfur, which also adds to properties of heat resistance. Prior to mixing, the resin was dried in a vacuum oven at 135 °C for 4 hours, then stored in a sealed container.

Table 3-3 Polyphenylene Sulfide Material Properties

Polyphenylene Sulfide Ryton QA200N (PPS)	
Density	1.34 g/cc
Water Absorption (24 hr, 23 °C)	0.05%
Tensile Modulus	3.4 Gpa
Tensile Stress	80 Mpa
Tensile Strain at Break	4%
Glass Transition Temperature (Tg)	90 ° C
Melting Temperature ™	285 ° C
Thermal Conductivity	0.29 W/m/K

3.1.4 Polysulfone (PSU)

Polysulfone (PSU) is a high glass transition temperature (190 °C – 230 °C) amorphous polymer. It has a much higher thermal stability than PA66 and PPS, and subsequently was selected due to its hydrolysis resistance. Hydrolytic resistance allows PSU to be useful in biochemical and water treatment applications[72] [73]. In this research, Polysulfone Udel P-3703 was purchased from Solvay Specialty Polymers, and its monomer structure and properties are given in Figure 3-4 and Table 4, respectively. P-3703 is a high flow version of PSU, most notably used for injection molding applications.

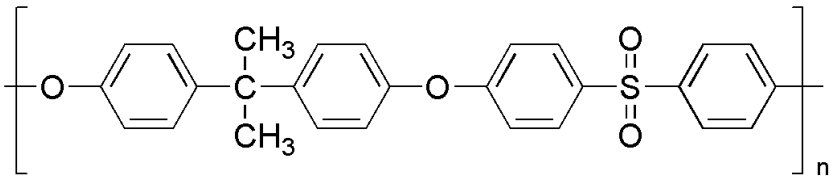

Figure 3-4 Polysulfone (PSU) Molecular Structure

PSU is comprised of aryl ether linkages followed by aryl sulfone group linkages. It is produced by a condensation reaction with a sodium salt of an aromatic diphenol (bisphenol-A) with bis (4-chlorophenyl) sulfone [74]. PSU is sought as a polycarbonate replacement due to the added properties imparted by the sulfone group, having added chemical resistance. Prior to processing, the resin was dried in a vacuum oven for 4 hours at 165 °C and stored in a sealed container.

Table 3-4 Polysulfone Material Properties

Polysulfone Udel P-3703 (PSU)	
Density	1.24 g/cc
Water Absorption (24 hr, 23 °C)	0.3%
Tensile Modulus	2.48 Gpa
Tensile Stress	70.3 Mpa
Tensile Strain at Break	50%
Glass Transition Temperature (Tg)	190 ° C
Melting Temperature ™	Amorphous
Thermal Conductivity	0.26 W/m/K

3.2 Sample Preparation

3.2.1 Exfoliated Graphite/Polyphenylene Sulfide Composites with Different Shear Strain Rates.

PPS with 0, 1, 2, 5, 10, and 20 % by weight of flake mineral graphite were mixed using a custom designed, high speed batch mixer, imparting elongational flow. The components were dry blended then mixed at 320 °C under an Ar (g) atmosphere for 10 min, to reduce polymer degradation. The concentrations were mixed with various shear strain rates, to research the effects of elongational flow on the degree of exfoliation and morphology.

Table 3-5 PPS Composite Concentrations

Shear Rate (s^{-1})	**Initial Graphite wt. %**

958	0 ,1 ,2 ,5 ,10 ,15 , 20
2876	0 ,1 ,2 ,5 ,10 ,15 , 20

Batch mixed compositions of graphite in PPS were used to create ASTM type V dog bones [75]. An aluminum mold was heated between two platens of a Carver press at 210 °C for 5 minutes. Compositions were heated in the barrel of a GALOMB micromolder, Figure 3-6, with a nitrogen blanket at 315 °C. The heated aluminum mold was transferred to the mold holder and 270 psi was applied to inject the molten material into the mold. The injected sample in the mold was placed onto a large aluminum Table, and allowed to cool to room temperature.

Figure 3-5 GALOMB Micromolder

3.2.2 Batch Mixed: Exfoliated Nylon and Graphite Composites

PA66, 20 wt. %, and 35 wt. % flake mineral graphite were mixed using a high shear batch mixer that imparts elongational flow. The blends were mixed at 276 °C and a shear strain rate of 2876 s^{-1}, under an Ar (g) atmosphere to reduce polymer degradation. 20 wt % graphite in PA66 was mixed for 20 min to access the process of exfoliation. 35 wt. % graphite and in PA66 and PA66 were mixed for 10, 20, 30, and 45 min to produce G-PA66 samples and PA66 control samples at each mixing time in Table 4-6. PA66 and G-PA66 extrudate (approximate diameter of 2.94 mm) were prepared for subsequent characterization.

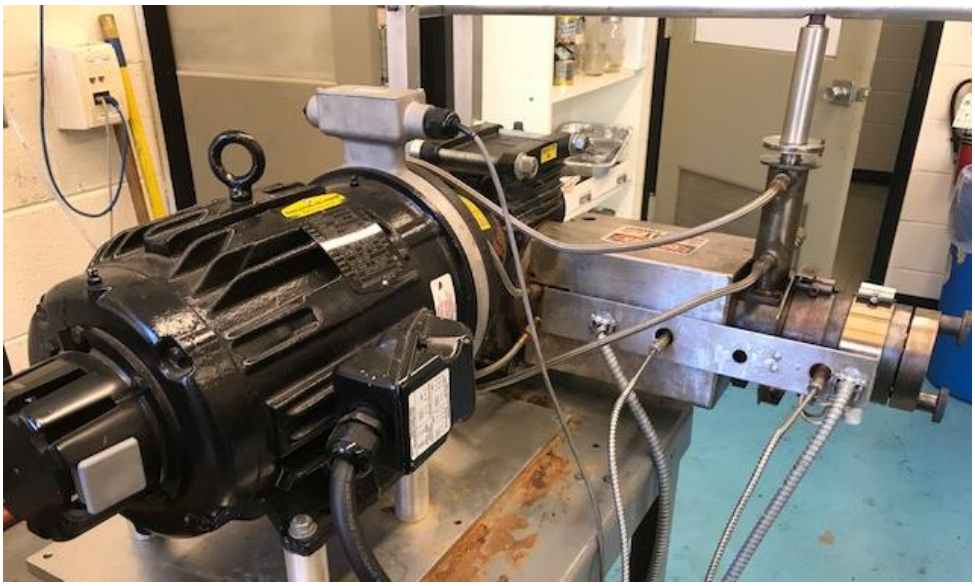

Figure 3-6 High Shear Batch Mixer

Table 3-6 PA66 Processing Table

Mixing Time (min)	Control Materials	Composite Materials

10	PA66	G-PA66
20	PA66	G-PA66 (20 % & 35%)
30	PA66	G-PA66
45	PA66	G-PA66

3.2.3 Cryogenically Cooled Polysulfone and Polyphenylene Sulfide extrudate

3.2.3.1 Polysulfone Samples

Resin of Polysulfone Udel P-3703 was dried and sheared in the high shear batch mixer at 360 °C and a shear strain rate of 2876 s^{-1} for 3 minutes, generating the shear rates and parameters in Table 4-7. While mixing, an Ar (g) atmosphere was applied to reduce degradation of extrudate. Using parameters in Table 4-7, the mixing exit port was opened and molten extrudate was allowed to collect on a Pyrex glass surface. After ~5 grams of resin was allowed to collect, the rest of the molten extrude fell into a liquid nitrogen bath. The experiment was conducted at shear rates of both 958 s^{-1} and 2876 s^{-1}. The results of the experiment were 4 different extrudates, 2 were allowed to cool at room temperature using high and low shear geometries, and 2 were cryogenically cooled with liquid nitrogen with the same parameters.

Table 3-7 Parameter Table

Mixing Time (min)	**Shear Rate (s^{-1})**
3	958
3	2876

3.2.3.2 Polyphenylene Sulfide Samples

Resin of Polyphenylene Sulfide QA200N was dried and sheared in the high shear batch mixer at 320 °C and a shear strain rate of 2876 s^{-1} for 3 minutes, generating shear rates and parameters in Table 4-7. While also mixing, an argon gas atmosphere was

applied to reduce degradation of extrudate. Extrudate was generated in the same manner as the PSU-graphite mixtures. The extrudate was collected then allowed to cool for characterization.

3.2.4 Creation of Polysulfone and Polysulfone Composite Extruded Sheets

3.2.4.1 Brabender Extruded

PSU pellets were dried at 165 °C for 4 hours in an air circulated oven. The dried PSU pellets were extruded into films using a Brabender Intelli-Torque Extruder with a 6" sheet die attachment at 360 °C and 50 RPM. The sheet extrudate was fed onto an air cooled roller, which was continuously collected. 20 % by weight of flake graphite and PSU was extruded using the same extrusion temperature at 30 RPM, to produce a continuous polymer-composite sheets. To analyze the degree of exfoliation by standard extruder, the composites containing 20 % exfoliated graphite in PSU was extruded 2 additional times. The exfoliated composite was granulated, dried, and extruded between each cycle.

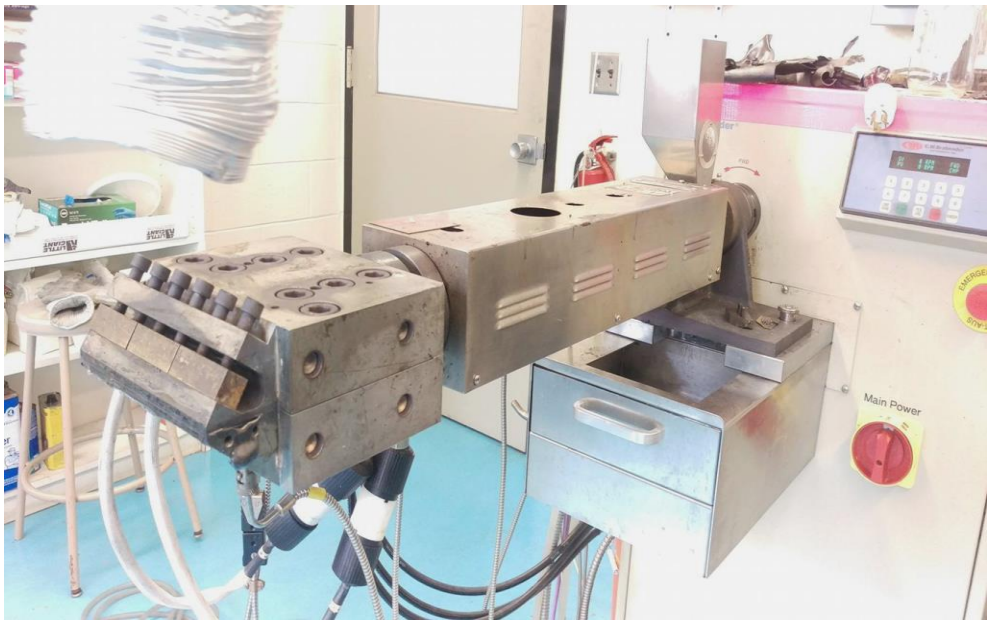

Figure 3-7 Brabender Intelli-Torque Extruder

3.2.4.2 Batch Mixer and Brabender Extruded Sheets

Batches of PSU and 20 % Graphite in PSU were mixed in a high speed extensional flow batch mixer at 360 °C and 360 rpm for 10 minutes. The batch mixed composite was dried, granulated, and extruded into 6" sheets using a Brabender Extruder at 360 °C and 30 RPM. The sheets were cut into 25.4 mm x 120 mm according to ASTM D882, and were tested in tension.

3.3 Characterization Tools

3.3.1 Field Emission Scanning Electron Microscopy (FESEM)

FESEM is a technique widely used to obtain topographical features, surface morphology, structure, grain orientation, chemical composition, and defect location[76]. In FESEM, an electron beam is directed to a target by a magnetic field. The electrons

released by a field emission source (FE gun) are focused into a spot size by electromagnetic lenses at a set acceleration voltage. The electron beam is rastered across the sample surface, creating electron-matter interactions, as in Figure 3-8. Electron-matter interactions create elastic (coulombic) scatting from the atomic nuclei and inelastically scattered electrons creating secondary electron sources. Secondary electron (SE) emission radiation is to create an image on a CCD detector, detailing the morphology of the rasterized surface structure.

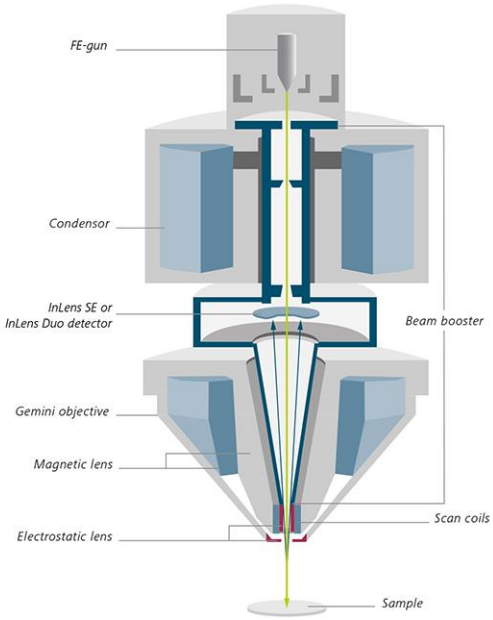

Figure 3-8 Sigma Field Emission Scanning Electron Microscope Schematic [77]

Polymer composite samples are prepared by a cryogenic brittle fractured methodology to create a clean observable surface. Materials are notched with a razor to

form an initiation point for fracture to occur, then subsequently submerged into a bath of liquid nitrogen. Sample are cleaved in liquid nitrogen, then placed on a FESEM stud.

Imaged samples are required to be conductive or are made conductive by sputtering with a conductive monolayer coating (carbon, aluminum, or gold). The conductor acts to dissipate any surface charge due to the build-up of an electric field on the surface, interacting with secondary electron radiation trying to reach the detector [76].

3.3.1.1 FESEM of PA66 Composite Sample

Batch mixed extrudate of 35% Graphite in PA66 was taken and sectioned off from the rest of the material. An extrudate rod was prepared by the cryogenic cleave method. The cryogenically fractured sample was placed on carbon tape secured to an aluminum stud. The sample and stud were gold coated with an E5 Sample Coater (Figure 3-9) to a thickness of about 5nm prior to analysis. The gold coated sample was observed using a Sigma Field Emission Scanning Electron Microscope with Oxford EDS attachment, as in Figure 3-10. The sample surface was observed using an In-lens detector at an accelerating voltage of 10 kV and a 10.9 mm working distance. The collected micrographs were used to analyze products from our process.

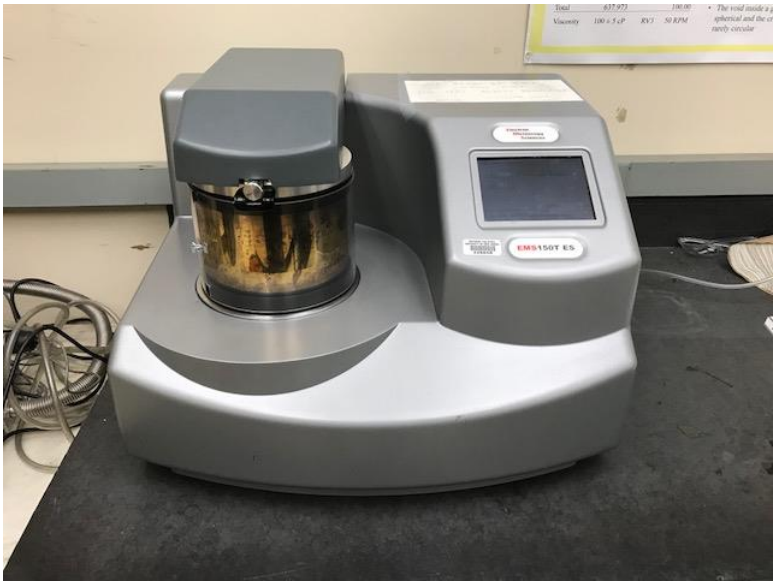

Figure 3-9 EMS150T E5 Sample Coater

Figure 3-10 Sigma Field Emission Scanning Electron Microscope with Oxford EDS

3.3.1.2 FESEM of PPS Composite Sample

Batch mixed extrudate samples of 1, 2, 5, 10, 15, and 20 % by weight of flake mineral graphite in PPS were taken and separated from the rest of the produced material.

Samples were prepared by the cryogenic cleavage methodology by fracturing in liquid nitrogen.

The fractured samples and stud were gold coated, then their surfaces were observed in the FESEM using an In-lens detector at varying accelerating voltages and working distances to detail surface features. The collected micrographs were then analyzed accordingly.

3.3.1.2 FESEM of PSU Composite Sheet

A batch mixed, then extruded, composite sheet of 20% graphite in PSU was cut into a 2" x 1" section, for electron microscopy. The top surface of the sheet was scored with a razor, secured between 2 metal plates, and then submerged into liquid nitrogen. The sheet was cleaved in liquid nitrogen then taken out to warm up to room temperature. The cleaved sheet was placed on carbon tape, secured to an aluminum SEM stud, then gold coated to a 5 nm thickness. The cleaved surface of the composite sheet was analyzed parallel to the surface of the stud.

3.3.2 Transmission Electron Microscopy (TEM)

Transmission electron microscopy has proven itself to be a very powerful technique in imaging on the nm scale, and for discerning nanostructures. TEM has similarities to FESEM in that it uses an electron source, but differs in the energy of the incident focused electrons and the setup for imaging, as in Figure 3-11. Samples are imaged by characterizing thinly sliced materials that mimic the surface structure, by using a high accelerating voltage. The prepared samples are transmittable to electrons accelerated at 100 – 400 kV, yielding elastic and inelastic scatting.

Elastic scattering allows for the observation of the internal crystal structure and atomic arrangement. Scattering obeys the conservation of the kinetic energy of the incoming electron, which interacts with the target electrons [78]. The scattered image is resolved energetically and is displayed by use of bright/dark image contrasting. This allows for a user to resolve any scattering or diffraction effects, interfacial boundaries, and spatially dependent phase information, especially for crystalline phases [79].

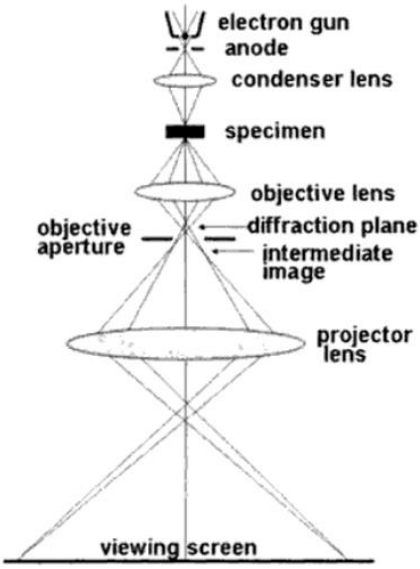

Figure 3-11 Transmission electron microscope schematic[80]

Inelastic scattering occurs with the transfer of energy from the incident electrons to the sample. This can produce sample heating, secondary emissions of X-rays, or secondary electron emissions. If the incident energy is higher than the ionization energy of the sample, beam damage can cause changes to the observable structure [79]. This would change the results of the analysis of a material or process.

Figure 3-12 JOEL Transmission Electron Microscope

$$\lambda = \frac{1.22}{\sqrt{E}} \quad (1)$$

For TEM, typically a higher accelerating voltage allows for an increase in lateral resolution of the scattering from the imaging structure, and is quantified from the de Broglie equation (1), where) E is the accelerating voltage of an electron (1eV = 1V) and λ is the wavelength, having a magnitude on the order of the smallest object, e.g., atom or molecule or aggregate, that is to be observed. If a TEM image were observed at 200 kV then the resolution limit is 0.027 Å, allowing sub- Angstrom level features to be resolved.

3.3.2.1 TEM of Graphite/PA66 Composite samples

Batch mixed extrudate of 35% graphite in PA66 were granulated using a Spex 6700 Freezer Mill to cryogenically pulverize samples and form a fine powder. The fine powder was ultra-sonicated in isopropyl alcohol (IPA) for 5 min to separate particles, then the suspension was drop coated on to a lacey carbon grid for transmission and characterization in a JEOL 2010F transmission electron microscope operating at 200kV for high resolution transmission electron microscopy (HR-TEM).

3.3.3 X-Ray Photoelectron Spectroscopy (XPS)

X-Ray photoelectron spectroscopy (XPS) is a technique that is used to characterize the surface chemistry of a sample. The technique operates under high vacuum at the sample surface. Photons of a specific energy are used to excite the electronic state of atoms at and just below the surface of a sample. The XPS spectrum is obtained by irradiating with an X-ray beam while simultaneously measuring the kinetic energy and number of electrons escaping from about 1 – 10 nm of material depending on the detection angle, as in Figure 3-13. The incidence angle is usually fixed and near normal.

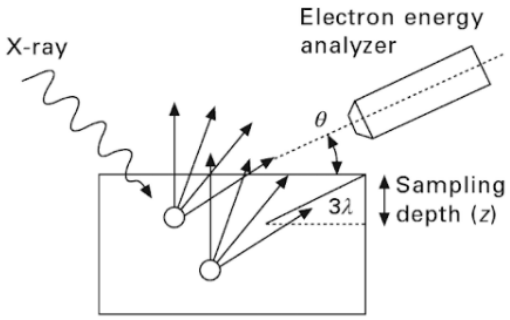

Figure 3-13 XPS sample excitation and detection [81]

The typical XPS spectrum is a plot that is based upon the number and energy of electrons detected. Each atomic state produces a characteristic set of XPS peaks at characteristic binding energy values that directly identify each element and its valence on the material surface [82]. These characteristic peaks correspond to the electron configuration within the atoms 1s, 2s, 2p, 3s, etc. The number of detected electrons in each characteristic peak is directly related to the concentration of the element within the area emitting these photoelectrons [83].

Figure 3-14 Thermo Fisher Scientific X-ray Photoelectron Spectrometer

3.3.3.1 XPS of Graphite/PA66 Composite Samples

Cryogenically milled powder of PA66 and graphite/PA66 extrudate was placed under vacuum overnight to remove water, due to PA66 being hygroscopic. The powders were placed onto carbon tape then analyzed using a Thermo Scientific K-Alpha X-ray photoelectron spectrometer (XPS). A spot size of 400 microns , with a monochromated aluminum K-alpha source at 1486.6 eV, and an energy resolution of 0.5 eV was used to collect the binding energy information from surface chemical states. Multiple scans were conducted to determine the C 1s, O 1s, and N 1s elemental binding energies**.** The final spectrum was an average of 10 scans, for improved resolution.

3.3.3.2 XPS of Graphite/PPS Composite Samples

Cryogenically milled powder of PPS and 20% graphite in PPS extrudate was placed under vacuum overnight. The powders were placed onto carbon tape then

analyzed using a Thermo Scientific K-Alpha XPS, using the same previously stated parameters. Multiple scans were conducted on carbon, oxygen, and sulfur elemental binding energies. The final result are an average of 10 scans

3.3.3.3 XPS of Graphite/PSU Composite Sheets Samples

Cryogenically milled powder of PSU, extruded PSU and extruded 20% Graphite in PSU extrudate was analyzed using XPS. Graphite/PSU extruded sheets were lightly scored with a microtome blade to remove surface polymer, with the remainder of the PSU containing samples scanned as is. The samples were then placed in a vacuum prior to processing. The samples were placed onto carbon tape, then analyzed using a Thermo Scientific K-Alpha XPS, using the same previously stated parameters. Ten scans were for carbon, oxygen, and sulfur elemental binding energies were averaged to produce the final result.

3.3.3.4 XPS Analysis of Samples

The acquired X-ray spectra were analyzed using Thermo Fisher Scientific Avantage software version 5.4.1. Survey spectra for each sample were first analyzed for atomic percentages by their identifiable photoelectric peak. The elemental peaks were identified, showed multiple modes, and were curve fitted with peaks at assigned binding energies for the initial chemical bonds found within the unmodified material. For the elemental peaks that show an additional mode present, after the curve fit, additional peaks were assigned.

3.3.4 X-Ray Diffraction (XRD)

X-Ray Diffraction (XRD) is a characterization technique that produces information about the crystalline phase and structural properties of the material. In XRD, a collimated beam of X-rays from a monochromatic source (λ =1.54 Å, from the Cu anode) are incident on a sample and diffracted at characteristic angles (θ) by the crystalline phase of a material, as described by Bragg's law (2)

$$\frac{\lambda}{\sin\theta} = 2d \tag{2}$$

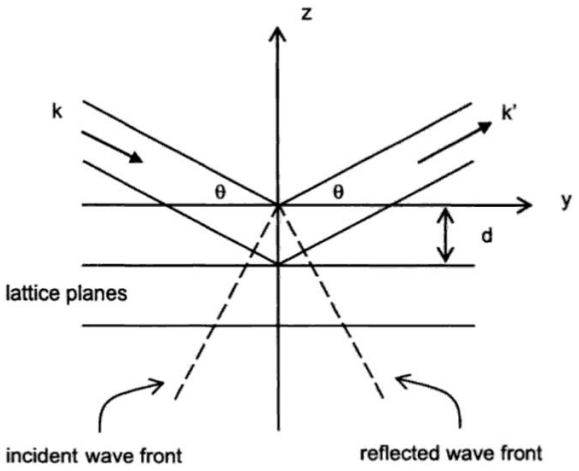

Figure 3-15 Interplanar diffraction schematic for Bragg's law; the x-axis perpendicular to the paper [84]

The crystalline phase is a repetition of specifically arranged atoms on planes with an interplanar distance (d). By use of Bragg's Law, the d-spacing can be said to represent distinctively characteristic directions. These directions are represented as 3D lattices of crystalline plane directions, hkl, called Miller indices. These indices are written as integer values, and represent a plane in a crystalline material [85]. In XRD, scans of diffraction from crystalline planes are output as sharp or broad Gaussian-like peaks, depending on the degree of crystallinity or size of crystalline domains. The peaks have specific

intensities depending on the structure and other factors such as absorption, polarization and extinction.

Figure 3-16 Philips XPERT Powder X-ray Diffractometer

$$D = \frac{K\lambda}{\beta \cos \theta} \tag{3}$$

To determine the size and orientation of crystal domains (D), the Scherrer equation (3) is a used. In the Scherrer equation, K is the shape factor (usually 0.9 assuming spherical grains, on the average),λ is the wavelength of the X-rays, β is the width at half the maximum height of a diffracted peak in radians, and θis the Bragg diffraction angle [86]. The use of the equation is found to be satisfactory for small grain/domain material with the absence of significant macrostrain [87]. It is safe to assume that strains within the measured sections are low, but consistent throughout the volume. From irradiated sample areas of about 1 cm^2 in the PXRD experiment, an

average domain size of diffracting material is obtained from the crystalline regions of the sample.

The entire scattering profile is a linear combination of scattering from amorphous regions and diffraction from crystalline regions of the sample. Thus, one can estimate the % crystalline (or, ir subtracted from 100%, the % amorphous) material in the sample by simply taking the ratio of the integrated net diffraction peaks to the entire scattering profile. The net diffracted peaks are minus their base-lines (e.g., background radiation), as the base-lines contain the amorphous scattering components.

3.3.4.1 XRD of Graphite/PA66 Composite Samples

Cryogenically milled powder of PA66 and 35% Graphite in PA66 were analyzed using a Philips X-Pert Powder X-Ray Diffractometer Figure 3-16. X-Ray Diffraction (XRD) was performed using a Cu (λ= 1.54 Å) K-alpha source at 45 kV/40 mA, and scanned from 4 ° to 70 ° 2Θ. The samples were scanned with a step size of 0.02° 2Θ to detect graphitic and nylon characteristic peaks.

3.3.4.2 XRD of Graphite/PPS Composite Samples

Micromolded discs of sheared PPS and Graphite contained PPS were analyzed using the same parameters in 4.3.4.1. Micromolded PPS samples were produced in same manner as the ASTM type V test bars, with the added changed of injecting samples into a 2 inch diameter disc mold. Aspects of the crystal structure of the PPS and Graphite were analyzed following diffraction.

3.3.4.3 XRD of Graphite/PSU Composite Samples

Extruded sheets of PSU and 20 % Graphite in PSU were analyzed using the same parameters in 4.3.4.1. Due to the amorphous nature of the PSU, scans were used to characterize the structure of the exfoliated graphite generated in-situ.

3.3.4.4 XRD Analysis

Diffraction data of composites and pure material were analyzed using JADE 7 to analyze peak positions and widths. Crystalline peaks for polymer samples were investigated by profile fitting to determine interplanar spacing and crystallite size. Graphite peaks were also fit to identify changes in crystallinity upon exfoliation by analysis of crystalline domain size in the (002) plane of graphite, as determined by the Scherrer equation.

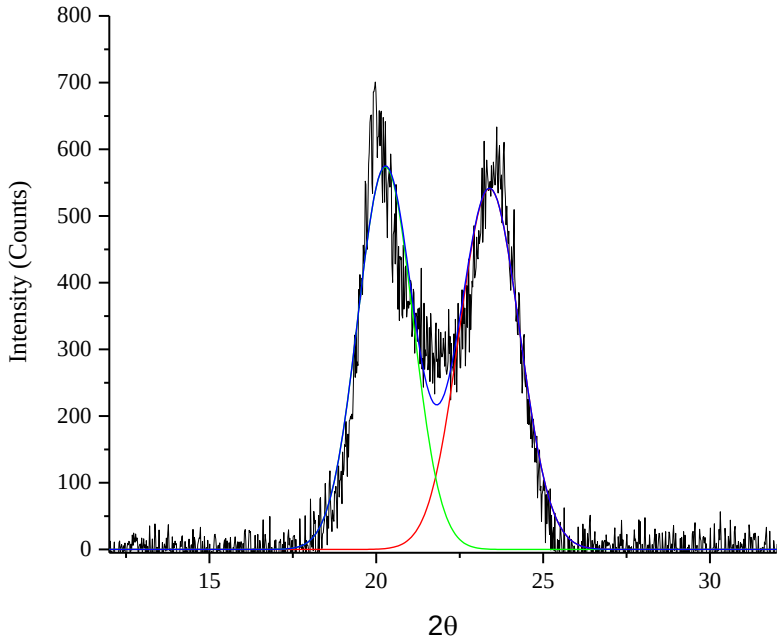

Figure 3-17 Profile fitting for peak width and interplanar spacing of PA66

Based on the shape and intensity of the diffraction pattern, an interpretation of the degree of exfoliation, or particulate breakup, can be analyzed. In the case of this work, distribution plays a tricky role in analysis. In diffraction, this distribution comes in the form of crystalline domains of a single size or a multi-domain size distribution. In single domain distribution, crystalline domains that have a longer-range order (larger) produce narrow intense peaks. As the single domain size decrease, the peak intensity decrease and broadens. This is indicative of approaching a nanocrystalline or graphene material. On the alternative case of resulting in a multi-domain distribution that is also nanocrystalline, peak broadening and intensity reduction is also occurring. Interpreting the difference between single domain distribution and multi-domain is not easily obtainable using the x-ray diffraction data and instrumentation within this work. What will be gained from analyzing the x-ray result is an approximation of the crystalline domains. The approximation suffices as a bulk characterization, which does not directly highlights the single domains within a particular multi-distribution.

3.3.5 Raman Spectroscopy

.

Raman Spectroscopy is a technique for the structural-chemical analysis of materials. The technique measures the scattering of monochromated light as photons, when they interact with a molecular surface, in Figure 3-18. As the incidental photons bombard a sample, elastic scattering, called Rayleigh scattering may occur. Rayleigh scattering is caused by the incidental photons interacting a molecular structure, causing no change in the incidental wavelength of light by the interaction event. The resulting photons that lead to an increase (blueshift) or decrease (redshift) in the incidental photon

wavelength, results in inelastic scattering events. Scattering events causing a shift in wavelength is termed the Raman Effect. Within the Raman Effect, scattering leading to a decreased wavelength (Stokes scattering) is caused by initial ground state excitation. Alternatively, scattering leading to an increase in wavelength (Anti-stokes scattering) is caused by excited state excitation [88].

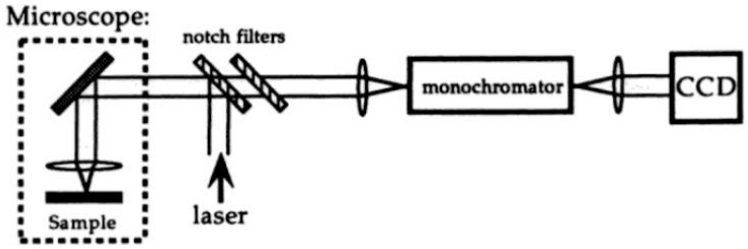

Figure 3-18 Typical Raman microscope configuration setup

The loss or gain in wavelength due to incidental photon bombardment provides a fingerprint for chemical bonding and symmetry of a material due to the polarizability of electrons in a molecule [88]. This provides materials information that has often served as a useful probing technique to identify process related changes in nanostructured materials [89].

Figure 3-19 Renishaw Raman Spectrometer

Raman has been a strong tool in the spectrographic analysis of identifying and characterizing graphene and its properties. Graphene's optical phonons exposed to mechanical stress or chemical treatment used Raman to detect strain, strength, and arrangement of chemical bond [90] [91, 92]. These identifiable changes in graphene are often detected by a shift in graphite's G peak (In plane strain) or its 2D peak (number of layers). These changes often provides a wealth of information about a material system. When the system consists of a composite containing both organic and inorganic materials, a resolvable Raman spectra becomes difficult to obtain. The difficulty in collecting the spectra of a composite sample lays in the generation of fluorescence, due to the incident photon energy. Fluorescence generation masks the Raman spectral finger print, making analysis difficult. When the photon energy is too high for a selected molecular surface (high wavelength), the photons are excited to the energy of electron-electron transition energy states. If the incidental photon energy is less than the transition

state, a Raman spectra is generated. A near infrared wavelength is lower energy, and often useful for polymer samples. Alternatively near infrared wavelengths will produce a weak Raman signal for inorganic materials sample. Higher energy wavelength (lower wavelength) chosen for graphene samples saturates the Raman signal, making analysis difficult. Often for composites, a fluorescence signal is in competition with Raman spectra, if the incident phonon energy is too high. This indicates that a keen selection of the proper wavelength is just as important in selectively identifying specific changes in specific constituents of a material. In this work, a 633nm laser was chosen to detect shifts in graphene's peaks. 633 nm was selected to avoid fluorescence issues by the polymer matrix, as mentioned.

3.3.5.1 Raman Spectroscopy of Graphite/PA66 Composite Samples

Cryogenically milled powder of Graphite/PA66 extrudate was ultra-sonicated in isopropyl alcohol (IPA) for 5 min, then the suspension was drop coated on to a glass slide. The glass side was characterized using a Renishaw inVia Raman Microscope. Samples are analyzed at a magnification 20x ,0.90 optical aperture and 10% laser power; using a 633 nm laser to identify changes in the spectra related to graphene. The 633 nm laser wavelength causes PA66 to fluoresce due to the high incidental excitation energy of incoming photons. Fluorescence causes PA66 in the composite spectra to appear as background noise, rendering the matrix finger print unable Graphite/graphene generate a strong Raman scattering at 633 nm[93].

3.3.6 Mechanical Properties

In the case of anisotropic materials, tensile strength is one of the most important physical properties, under standard use. These materials tend to be stronger in one or two dimensions, due to the method in their production. In the case of graphene, the 2D materials has an extremely high modulus within the planar direction. Tensile testing acts as a useful technique that would be able to identify a composite with strength closer to graphene's theoretical values. In regards to the rest of the composite tensile testing is sensitive to microstructural changes such as, crosslinking, branching, crystallinity, adhesion, and matrix or filler orientation[94]. In addition to the structural changes taking place, test tend to be inhomogeneous in application; generating volumetric deformations. Because of this, mechanical testing is standardized by temperature, rate of test, and direction of deformation. These parameters Generate reproducible results; that become morphology specific.

Test specimens are stretched at a constant rate, based on length. Stress is measure by extension Force (F) as Newtons by a transducer per-unit-area (A), normal to the samples surface (Stress = F/A).

Figure 3-20 MTS Qtest / 25 Tensile Testing Machine

The strain of the sample is given by the displacement (Δl) over the initial length of the samples (l_0); (Strain (%) = Δl/ (l_0). The stiffness, as elastic modulus E of a material is measured by dividing the Stress by Strain in the linear region of the curve, at a given test speed. These values are used to detail strength and stiffness under an applied load. Based on the usefulness of this technique; changes in these values translate into structural changes in the composite. Features like improved bonding, increased crystallinity, or development of nanocrystalline region can be analyzed using this characterization method.

3.3.6.1 Tensile Testing of Graphite/PA66 Composite Sample

Micromolded dog bones of ASTM type V samples of PA66 20% graphite in PA66 and 35% graphite in PA66 composite samples were tested on an MTS Qtest 25

testing machine according to ASTM D638 at a crosshead rate of 1.2 mm/min. Samples were tested until breakage, with the results further analyzed for property variations due to process.

3.3.6.1 Tensile Testing of Graphite/PPS Composite Sample

Micromolded dog bones of ASTM type V samples of high and low speed shear strain rate Graphite/PPS (0, 1, 2, 5, 10, and 20 %) composite samples were tested under the same experimental conditions as 4.3.6.1. Samples were tested until breakage, with the results further analyzed for property variations due to processing.

3.3.6.2 Tensile Testing of Graphite/PSU Composite Sheet

Extruded Sheets of PSU and 20% Graphite in PSU were tested on an MTS Qtest 25 testing machine according to ASTM D882. Samples of 25.4 mm x 120 mm strips of extruded material were cut and tested under extension. Strips of paper were placed between the grips to prevent slipping and reduce premature tearing by the serration in the grips. During the test, the paper helped distribute the stress to the grip surface, leading to consistent breakage in the center. Sheets were extended at a crosshead rate of 50 mm/ min until the sheets fractured. The results were then analyzed to address characteristic changes due to processing.

3.3.7 Differential Scanning Calorimetry (DSC)

DSC is a thermal analysis technique that measures the heat capacity of a sample at constant atmospheric pressure, under an inert gas atmosphere. Test specimens are measured at constant heating rates where the difference in heat flow is measured against a reference sample, in Figure 3-21.

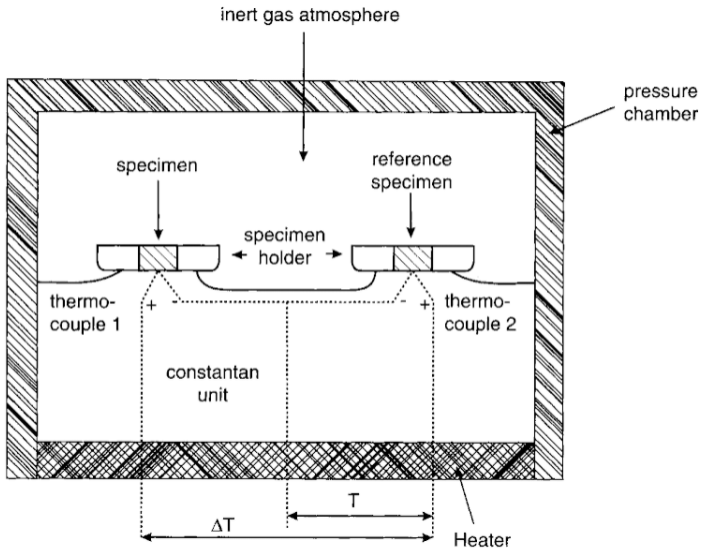

Figure 3-21 Schematic of DSC sample test chamber [95]

At a constant heating or cooling rate, variation in heat flow create exothermic and endothermic shifts in the thermogram. The measured shifts are interpreted as a thermodynamic transition like; glass transition (T_g), recrystallization temperature (T_r), crystallization temperature (T_c), and melting temperature (Tm)[96]. In the field of polymers and composites, a change in these transitions, can produce information about changes due to crystallinity, stability, or morphology.

Figure 3-22 TA Instruments Q1000 Differential Scanning Calorimeter

Information that can be resolved from thermodynamic data in DSC is the % crystallinity. This information is a qualitative technique that describes the bulk crystallinity of sample, which could be used to explain comparative results of improvement in material characteristic due to processing. The results of the bulk crystallinity is measured by calculating the ratio of the enthalpy of melting (ΔHm) for, to the enthalpy of melting a 100 % crystalline sample (ΔHm_{100}) (7), by thermal analysis.

$$\text{Weight \% Crystallinity} = \frac{\Delta Hm}{\Delta Hm_{100}} \times 100 \qquad (7)$$

Another piece of information that can be resolved from the thermodynamic data is the activation energy in the given thermodynamic transitions. The values for activation energies are generated by plotting the heating rates to the temperature of a given thermodynamic change (Kissinger method) [97]. The y-axis of the plot uses natural log

of the ratio between the heating rate (Q) the heating rate and square of the transition temperature (T) (8).

$$\ln\left(\frac{Q}{T^2}\right) \tag{8}$$

$$\frac{10^3}{T} \tag{9}$$

The x-axis is the ratio of 1000 to the transition temperature (T) (9). The curve plot produces a straight line containing a linear equation. The slope of the linear equation is the activation energy of the transition [98]. The activation energy provides information on the isothermal kinetics of the glass transition, melting, and crystallization process of created materials.

3.3.7.1 DSC of Graphite/PA66 Composites

DSC results of PA66 and Graphite/PA66 samples were determined using a Q1000 Differential Scanning Calorimeter. Samples weighing 10 mg were subject to heating, cooling, and reheating at 10°C /min from 0° – 300° C, under a nitrogen atmosphere. The effect of processing on the melting ™, crystallization (Tc), and glass transition (Tg) temperatures of the PA66 component was determined, to include enthalpy of crystallization ΔHc, enthalpy of melting ΔHm, and % crystallinity in PA66.

3.3.7.2 DSC of Cryogenically cooled Polysulfone and Polyphenylene Sulfide Extrudate

DSC results comparing room temperature and cryogenically cooled PSU and PPS samples were tested using a Q1000 Differential Scanning Calorimeter. Samples weighing 10 mg, were sectioned from the extrudate and subject to a single heat ramp at 10, 20 and 30°C /min 0° – 330° C under a nitrogen atmosphere. Cryogenic and room temperature

cooled samples using two different processing methods were tested. Their glass transition (T_g), recrystallization (T_r), and melting temperatures ™ were determined and analyzed. The given thermal transitions were plotted using the method developed by Kissinger, where their activation energies were found.

3.3.7.3 DSC of Graphite/PPS Composites Samples

DSC results of PPS and Graphite/PPS samples were tested using the same experimental parameters in 4.3.7.1 from 0 – 330 °C. Transition peaks were analyzed under the same conditions as PA66, and assessed by changes in processing conditions and degree of exfoliation.

3.3.7.4 DSC of Graphite/PSU Extruded Sheets

DSC results of PSU and 20% Graphite in PSU sheets were tested using the same experimental parameters in 4.3.7.2 from 0 – 230 °C. Thermal transitions were analyzed using the method developed by Kissinger. Changes in activation energy by processing conditions were assessed by degree of exfoliation and polymer chain extension.

Chapter 4 Exfoliated graphite in polyphenylene sulfide (PPS) under a high and low shear strain rate

4.1 Summary

An analysis of exfoliation, leading to functionalization under high and low shear strain rate, was conducted. Variation in shear strain rates are produced by studying the change in performance of a novel mixer, generating two distinctly different strain rates. At low concentration, a high shear strain rate of 2876 s^{-1} produced diffusion dominated exfoliation whereas low shear strain rates (958 s^{-1}) produced surface driven exfoliation, converting graphite to graphene. Both methods were able to produce functionalization of PPS to the graphene exfoliate in the matrix, observed by preferential crystal growth on the edge and surface planes of graphene. Through the combined results of thermal analysis by differential scanning calorimetry, X-ray diffraction, X-Ray Photoelectron Spectroscopy, and mechanical properties, results have shown that covalent and noncovalent bonding between the PPS and graphene exfoliate was developed. This has led to better π- π bond interactions at the interface between the two systems; creating improved stress transfer based on the increase in elastic modulus.

4.2 Introduction

In composite engineering, the drive is to find a material that reduces weight with the added ability of improving properties. In the utilization of polymers with good intrinsic properties, a new, higher modulus class of materials can be achieved. Our advantage in this type of compositing lay in our approach to mixing these polymers with the 2D material. A small problem with this method is that available graphene is very

expensive to use as a reinforcing material. A small addition of graphene, by weight, substantially increases material cost with only minor advantages in property improvement [99] . By investigating a process of creating a cost effective graphene reinforced composites, using the novel process detailed in Nosker et al [42], we begin to understand the that primary and secondary chemical interactions are developed in this process. In this work, the exfoliation of graphite is investigated by observing the effects of high and low shear strain rate in a PPS matrix.

Exfoliation has been found to be dependent on the variable change in the draw ratio, temperature, and the affinity of matrix and filler molecules [100]. In the case of polymer matrix-filler chemical affinity, it is suggested that the process can in part be assisted by diffusion [101] for clay filled composite material [102]. If the condition of clay exfoliation is similar in our graphite system, our model driven by creation of two high surface areas, interact favorably. This favorable interaction is created by bonding between matrix and filler, which are translated to material and morphological properties.

Polyphenylene Sulfide (PPS) pellets were dried in a vacuum oven at 135 °C for 4 hours with glass sealed flake graphite dried at 100 °C overnight. Flake Graphite and PPS were subject to extensional mixing at concentrations of 0, 1, 2, 5, 10, and 20 wt % Graphite in PPS. The concentrations were mixed at shear strain rates of 958 s^{-1} and 2876 s^{-1} respectively. The blends were mixed for 10 minutes under an Ar (g) atmosphere to prevent degradation. After mixing, they were extruded and molded into ASTM D638 type 5 dog bones at 315 °C using a GALOMB micromolder, Figure 4-5.

4.3 Structural and morphological analysis of PPS

4.3.1 X-Ray Diffraction of PPS PMCs

X-Ray diffraction was used to characterize the crystal structure and the results of exfoliation in a starting graphite and PPS composite. ASTM D638 type 5 dog bone samples were machined into discs, and their crystalline structure was detected. The resulting patterns were used to examine the graphite lattice structure and domain size in the (002) plane. In the PPS phase, the (110) and (200) planes were analyzed.

In the analysis of the starting graphite, the (002) plane has a crystalline domain size of 62.7 nm in Table 4-1. In Figure 4-1, we are reminded that the expected direction of (002) plane is parallel to the graphite c-axis thickness of 0.34 nm. The domain size obtained, represent an average value over the respected graphite tested. Average values for graphite thicknesses have a degree of deviation, where larger and smaller domains are still present. The results show in Table 4-1 that our exfoliation process [30] reduced the average domain size of all graphite-PPS concentrations. A high concentration of graphite is found to yield a greater size reduction. Comparing the degree of exfoliation, high shear strain rates are more effective at reducing the size of the graphite thickness. Therefore, high starting graphite concentration and high shear rates provide the fastest route to optimal exfoliation.

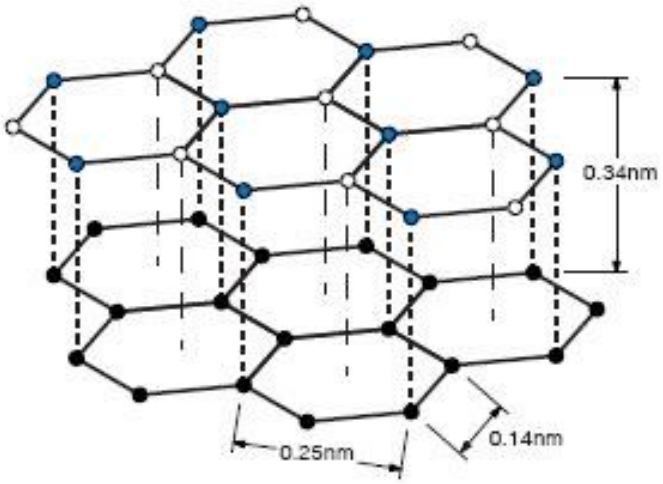

Figure 4-1 Graphite Lattice Structure

For high shear strain rate (HS) versus low strain rate (LS), we observe that HS provides the smallest (002) approximation for the crystalline domain size; having the highest plurality of few and many layer graphene flakes, in Table 4-1. By curve fitting the results, we observe that exfoliation closely follows an exponential decay model. In our mixing processes, an exponential decay model will uniformly extend to molecular diffusion acting on the concentration of species present. When there is greater extension and increase in shear rate of mixing, there is an increase in rate of decay (A1 – LS =15.4 and A1-HS = 21.0, Figure 4-2) [103]. When this extends to the variation in domain size, the fit in Figure 4-2 suggest an 11 nm reduction in the (002) crystalline domain, indicative to a relative thickness reduction of 33 layers of graphene. This thickness is obtained by the constant (y0, Figure 4-2), based on the shear strain rate.

Assessing exfoliation data in Table 4-1, we can see that at 5 wt % HS and 2 wt % LS graphite concentration, results suggest a discontinuity in the fitting curve. Observed exfoliation is steadily occurring, understood by the fact that the domain size is a fraction

of the starting graphite. The discontinuity hints to a transitional concentration, which is often seen for starting graphene containing composites. In our case, this transition is shear rate dependent, which acts as a good indication in the role diffusion plays in this process. We should also take note that using XRD as a characterization method to identify the presence of graphene, flakes below 20 nm, may not be resolvable in the current experiment, but accounted for in the domain size approximation. These results are likely not to reflect the plurality of graphene sizes due to the methodology. Address further in this work, we will be able to verify few and many layer graphene flakes not captured in our diffraction methodology, but by electron microscopy.

Table 4-1 Graphite (002) d-spacing and domain size

Material	**Wt. % Graphite**	**Graphite d (002) nm – LS**	**Graphite (002) domain nm – LS**	**Graphite d (002) nm – HS**	**Graphite (002) domain nm – HS**
Graphite	100	0.3344 (~)	62.7 (4.1)	0.3344 (~)	62.7 (4.1)
G-PPS	1	0.3365 (~)	38.8 (2.1)	0.3355 (~)	43.3 (1.8)
G-PPS	2	0.3364 (~)	39.6 (0.7)	0.3341 (~)	28.4 (1.0)
G-PPS	5	0.3365 (~)	36.6 (1.5)	0.3346 (~)	42.8 (2.6)
G-PPS	10	0.3355 (~)	34.4 (0.6)	0.3380 (~)	21.5 (1.0)
G-PPS	20	0.3356 (~)	31.9 (1.4)	0.3347 (~)	20.6 (0.7)

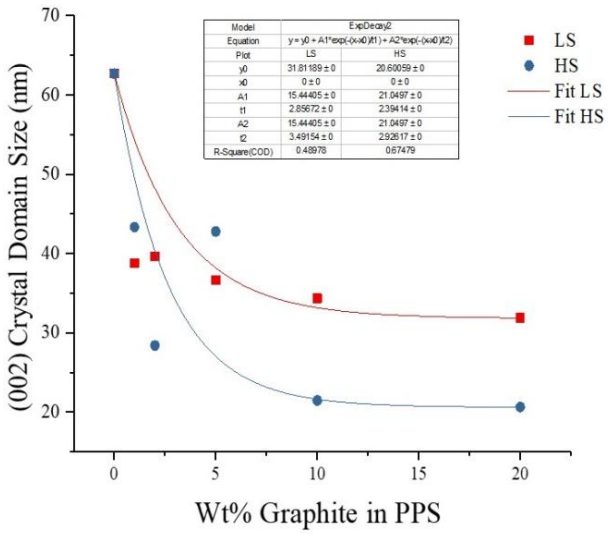

Figure 4-2 Graphite (002) domain size vs concentration with exponential decay average curve fit

Changes in the PPS matrix, caused by exfoliation act as important clues to functionalization of the created graphene. These clues present themselves as crystal structure alterations, preferential crystal growth, and possibly oriented crystal domains. In the analysis of HS and LS, due to increases in concentration of starting graphite, the diffraction pattern of PPS in the matrix produce changes in characteristic crystalline peaks. These changes are seen in Figure 4-4 & 4-5, where the first peak near ~19 ° 2 Θ represents the (200) crystalline plane and the second, ~21° 2 Θ (110) plane. In the interpretation of PPS crystal structure, the (200) plane corresponds to the zig-zag arranged surface for sulfur atoms in the backbone, while the (110) plane corresponds to the phenyl group on the PPS chain folding surface [104] in Figure 4-3.

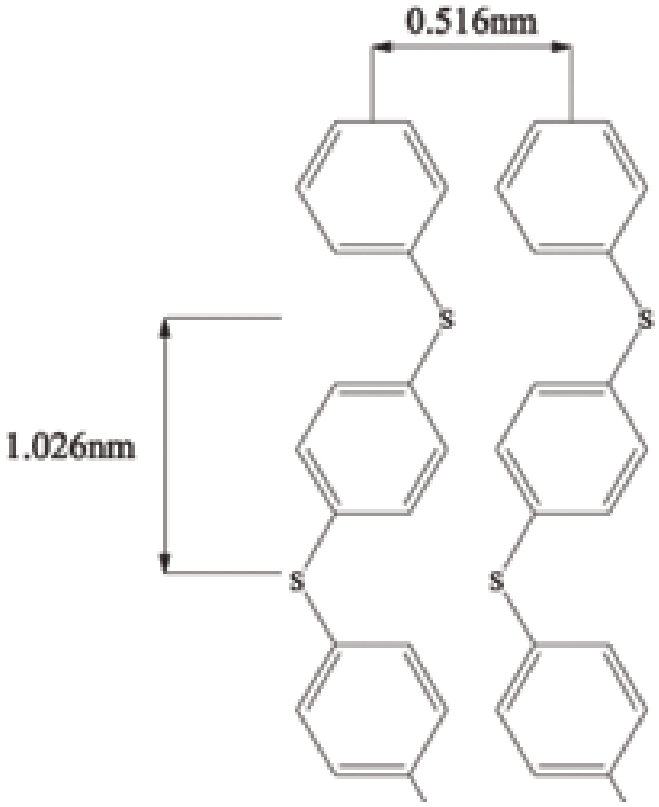

Figure 4-3 Crystal structure of PPS

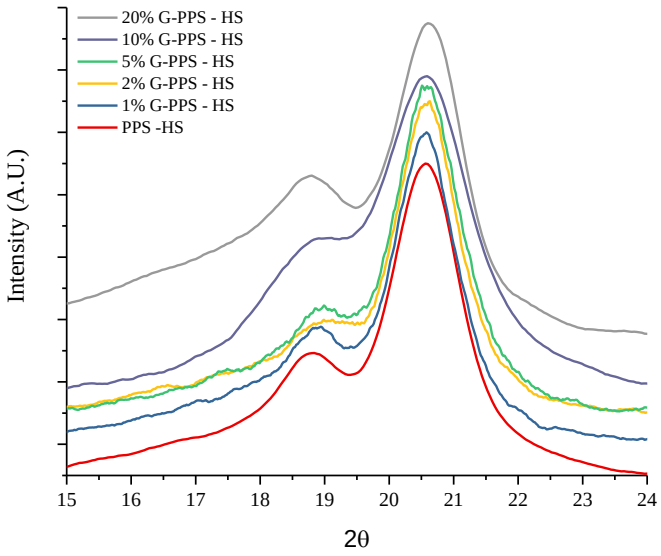

Figure 4-4 X-Ray Diffraction pattern of PPS (200) and (110) plane by HS

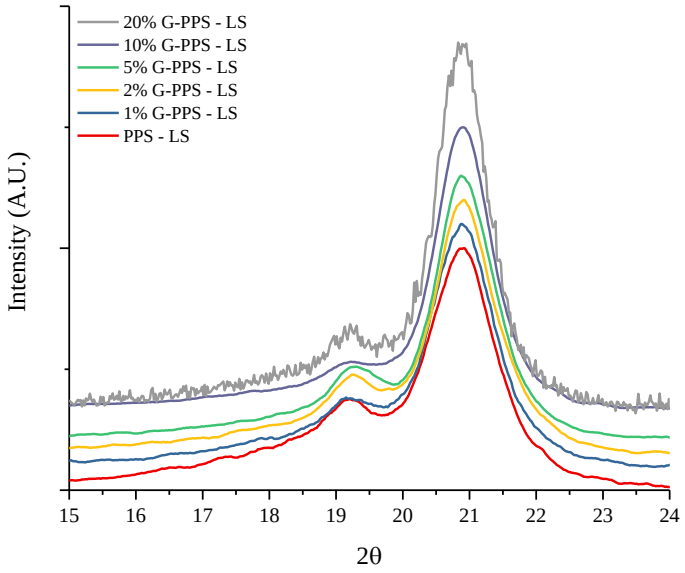

Figure 4-5 X-Ray Diffraction pattern of PPS (200) and (110) plane by LS

In Table 4-2, the effects of low shear strain rate (LS) produce larger domain sizes in the zig-zag (200) plane of PPS overall, compared to the high shear strain rate. In G-PPS LS, as the concentration of graphite increases, there is a slow increase, then an abrupt decrease in (200), transitioning at 10 wt % graphene exfoliate for Figure 4-6. For (110) in the same LS process concentrations, there is a continuous increase in the polymer domain in Figure 4-7, suggesting a direct relation to graphite concentration. In G-PPS HS, the opposite effect occurs in the domain size in (200), with a decrease leading to an increase at the same 10 wt % graphite concentration in the table data. However, the (110) domain shows no dependence on the concentration, but never exceeds 8.2 nm, in Figure 4-7. This suggests shear rate and exfoliation morphology plays a significant role on the creation of these distinct crystallites. Diffusion driven by shear rate, lead to driving the polymer into the graphite galleries. As the concentration of graphite increases, the degree at which the polymer changes its conformation and interacts with the system increases. Within the mixing system, the polymer will eventually diffuse into the layer,

relative to the concentration environment. Overall, the results in Table 4-2 indicates that higher shear strain rate produces smaller crystal domains by the dispersion of graphene sizes through a finite volume.

Table 4-2 Diffraction results for PPS (200) and (110) domain size d-spacing

Materials	Wt. % Graphite	(200) d (nm)	(200) Domain size (nm)	(110) d (nm)	(110) Domain size (nm)
PPS LS	0	0.462	12.2 (5.1)	0.425	8.4 (0.7)
G PPS LS	1	0.461	9.7 (1.1)	0.423	8.5 (0.2)
G PPS LS	2	0.462	10.1 (0.7)	0.425	8.6 (0.2)
G PPS LS	5	0.460	12.0 (0.7)	0.424	9.2 (0.2)
G PPS LS	10	0.468	7.8 (0.9)	0.430	9.4 (0.2)
G PPS LS	20	0.456	7.1 (1.3)	0.419	9.9 (0.2)
PPS HS	0	0.474	5.8 (0.2)	0.431	7.6 (0.1)
G PPS HS	1	0.467	2.6 (0.4)	0.425	7.3 (0.2)
G PPS HS	2	0.463	2.5 (0.9)	0.422	8.2 (0.2)
G PPS HS	5	0.461	2.3 (1.4)	0.422	7.6 (0.3)
G PPS HS	10	0.479	5.7 (0.5)	0.437	6.7 (0.2)
G PPS HS	20	0.478	6.4 (0.2)	0.434	7.8 (0.2)

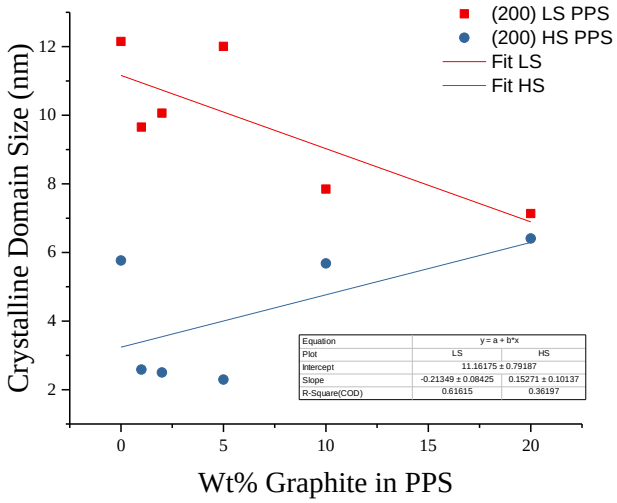

Figure 4-6 PPS (200) domain parameters vs graphite concentration with linear curve fit

Research has been done to understanding the epitaxial growth of PPS on different surfaces. Work by Qian et al suggested that the (200) plane often nucleated on steps or line defects, whereas (110) nucleation occurs along the planar surface [105]. If we are to expand our interpretation on the research conducted by Qian, PPS has preferential growth of particular domains dependent on the type of functionalizable surface present. In the case of the (200) plane, edge nucleation by sulfur occurs. If the edges/line defects present in the exfoliated many layer graphene are long and continuous (in G-PPS LS vs G-PPS HS), there is an increase in the (200) domain, Figure 4-6. If these steps and line defects are populous and small, a small (200) domain would be the result. For the (110) plane, π-π interactions leading to nucleation by the phenylene group in the polymer with graphite occurs. An increase in exfoliated graphene concentration leads to progressively larger (110) domains in G-PPS LS but an apparent suppression in G-PPS HS ,in Figure 4-7. In our exfoliation process, the small domains and suppression is likely caused by the creation of dangling bonds through graphitic sheet ripping. The polymer interacts at both line defects and within the surface, slowing down nucleation in HS.

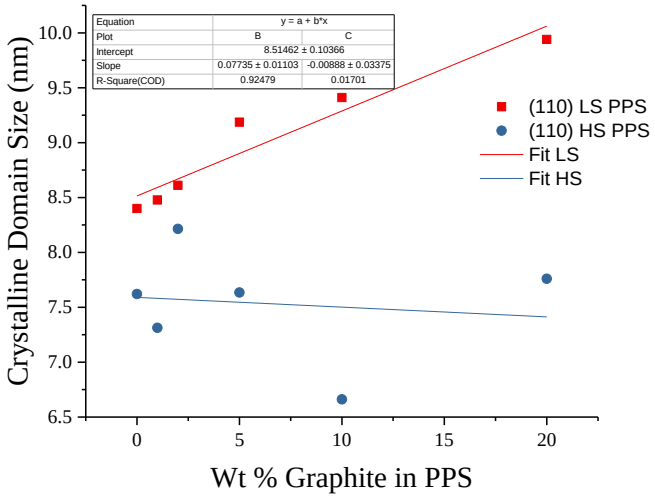

Figure 4-7 PPS (110) domain parameters vs Graphite concentration with linear curve fit

A closer observation of the (200) and (110) domain sizes suggest the crystallites are anisotropy, Figure 4-8. Observing the ratio between the phenylene group (π plane) to the sulfur, HS has crystal domains larger in the (110) direction. The aspect ratio between (110):(200) domains, above and below the isotropic line in Figure 4-8, suggest a mechanisms of exfoliation which relates to the bonding morphology present. By taking the exponential decay model into account, intercalation and outer layer fragmentation by creating dangling bonds (Large Scale Exfoliation = LSE) are propose to be occurring. If the aspect ratio of (110)/(200) > 1, exfoliation is dominated by intercalation of the polymer within the graphite layers leading to π- π stacking by the phenyl group. Diffusion is anticipated in either case due to the intercalation of PPS and the crystal growth due to confinement of the polymer between graphite layers. If (110)/ (200) < 1, LSE results in nucleation on the outer edges and surface defects given by the increased amount of dangling bonds present in the composite, hence primary bonding.

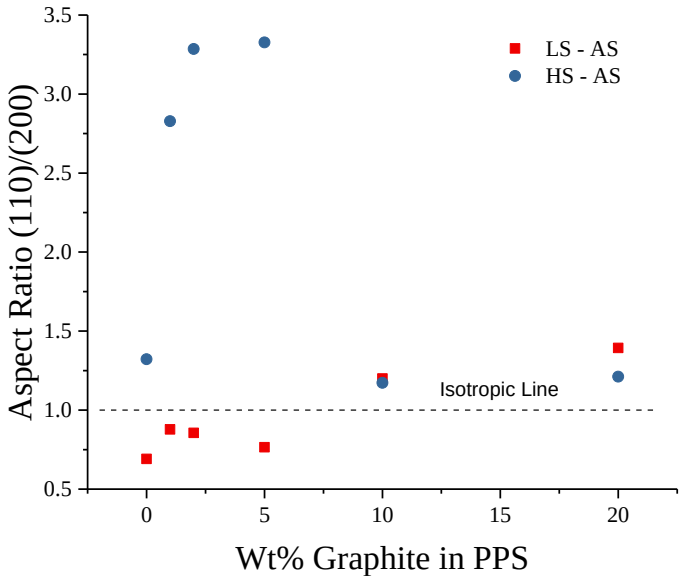

Figure 4-8 PPS (110)/(200) Domain isotropy parameter vs graphite concentration

4.3.2 Differential Scanning Calorimetry of PPS PMCs

Calorimetry results for PPS and G-PPS appear in Table 4-3, with corresponding thermograms in the supplemental data. The glass transition temperatures for PPS and G-PPS were calculated using a baseline tangential method. A line representing the baseline was drawn from 20° C in the direction of increasing temperature. A deviation from the baseline, at an inflection point in the thermogram, was found to be the glass transition temperature (T_g). The bulk crystallinity of PPS was calculated according to (1), for which enthalpy of melting for 100 % crystalline PPS is ΔHm_{100} = 76.5 J/g[106] . The values for ΔHm and ΔHc were adjusted for percent PPS, due to G-PPS having varying wt % of polymer present.

$$\text{Weight \% Crystallinity} = \frac{\Delta Hm}{\Delta Hm_{100}} \times 100 \qquad (1)$$

Table 4-3 Differential scanning calorimetry results for PPS and G-PPS

Materials	Wt % Graphite	Tg (°C)	Onset Tm (°C)	Tm (°C)	ΔHm (J/g)	Onset Tc (°C)	Tc (°C)	ΔHc (J/g)	Crystallinity %
PS – LS	0	102	265	280	33	251	242	41	43
G-PPS – LS	1	101	270	285	43	260	251	50	56
G-PPS – LS	2	102	269	281	41	248	241	52	54
G-PPS – LS	5	103	266	280	41	246	238	52	54
G-PPS – LS	10	101	268	282	39	251	243	50	51
G-PPS – LS	20	96	266	279	29	258	248	32	38
PPS – HS	0	99	267	278	41	234	226	46	54
G-PPS – HS	1	104	264	281	37	245	237	48	48
G-PPS – HS	2	104	258	277	34	238	227	46	44
G-PPS – HS	5	96	269	280	27	247	241	30	35
G-PPS – HS	10	99	264	278	59	244	237	67	77
G-PPS – HS	20	102	267	281	44	254	245	54	58

The T_g in both processes are higher than the value provided by the manufacturer, at 90°C. This suggests that the process alone produces a thermal property improvement, indicative of increased crystallinity or degree of crosslinking. From the overall interpretation of the aspect ratio of the crystal domains formed, we recall that HS is dominated by functionalization on surface and line defects by dangling bonds, which is further lead to intercalation. This recalled by the anisotropy of the crystallites and the low domain size of the (200) diffraction direction. In LS, PPS intercalation is lower in low concentrations but dominated by nucleation from the sulfur on the larger line defects caused by dangling bonds. An increase in graphite concentration of 10 – 20 % dangling bonds become more prevalent due to the increased graphene conversion. Splitting these interpretations, the LS has an average increased T_g due to functionalization while HS has an increased T_g via strong conformational deformations by intercalation as well as functionalization.

The melting temperature by either method, having a 1% concentration of exfoliated graphene produces the highest increase melting temperature for the composite, Table 4-3. For a low concentration of initial graphite concentration in HS, the oriented domains have a lower % crystallinity than the near isotropic domains in the LS. In the composite with the highest calculated percent crystallinity, in Table 4-3, 10 % graphite within HS transitions to relatively larger near isotopically shaped crystalline domains. This composite also has the largest crystalline lattice in (200) and (110) directions. The change in domain and lattice provides evidence for the higher percent crystallinity. The likely culprit is the highly anisotropic flow, orienting and changing the conformation of the PPS causing crystallite nucleation. The same results continue to translate to the HS composite at graphite concentration of 20 % but drop off for LS due to its reduced domain size.

The results in Table 4-3 suggest exfoliated many layer graphene act as a site dominated by heterogeneous nucleation of PPS. Nucleation is observed by a more than 9 °C increase in crystallization temperature (Tc), compared to the unreinforced material. The Tc increase attributed concentrations occur in the lowest and the highest percentage of many layer graphene, for both LS and HS composites. The low concentration LS composite form smaller domains leading to early onset crystallization, by a (200) domain reduction in Table 4-2. As the concentration increases, (200) domain continues to be low but increases in the (110) direction for LS. Based on the results in Table 4-2, this suggest the development of distinctly different crystallites by graphite concentration. As mentioned for the G-PPS HS, there exist early onset crystallization leading to heterogeneous nucleation. The low concentration nucleation is likewise represented by a

reduced (200) domain, as in LS composite. Unlike The higher concentration of graphite in HS (~20%), a reduction in (200) domain is not represented. In fact, specific to the domains, there are no discernable trends indicative of nucleation by crystal structure in PPS. In higher concentration HS, the graphite is highly exfoliated indicating early onset crystallization is noticeably due to the presence of graphene exfoliate. Table 4-1.

4.3.3 Electron Microscopy of PPS PMCs

Increasing concentrations of wt. % graphite in PPS composites were cold fractured in liquid nitrogen to produce a surface ideal for electron microscopy. From Figure 4-9, as the starting concentration of graphite is increasing from 1% – 20%, the processes of exfoliation generates continuously disrupted graphite flakes. In Figure 4-9, the morphology of the fractured surface changes with increasing concentration, generating surface features more sensitive to interactions of the PPS, with increasing initial graphite concentration. At low concentrations of 1 – 2% the surface is smooth, with exfoliate flake and PPS matrix present. Graphite flake pullout is absent at these low concentrations, suggesting the concentration dependent adhesion proposed earlier. As the concentration is increased to 5 -10%, the voids left by flake pullout become obvious, in Figure 4-9. In the 10 % graphite concentration, adhesion of PPS on the surface and edges of the exfoliate graphene structure cause the sheet to curl and separate from others. This separation causes the surface to appear porous, once fractured. At 20 % graphite in PPS the surface is unmistakably different, by the absence of the curling phenomenon at lower concentrations of many layer graphene flake edge. The separation of flakes is a dominant feature, suggesting this to be an occurrence at the surface of the graphite on PPS. The

increasing concentration of graphite also leads to difficulties in finding the PPS matrix. Due to the separation of the flakes, it is likely that the polymer has a strong adhesion to the surface of many layer graphene in these micrographs, which results in these unique features.

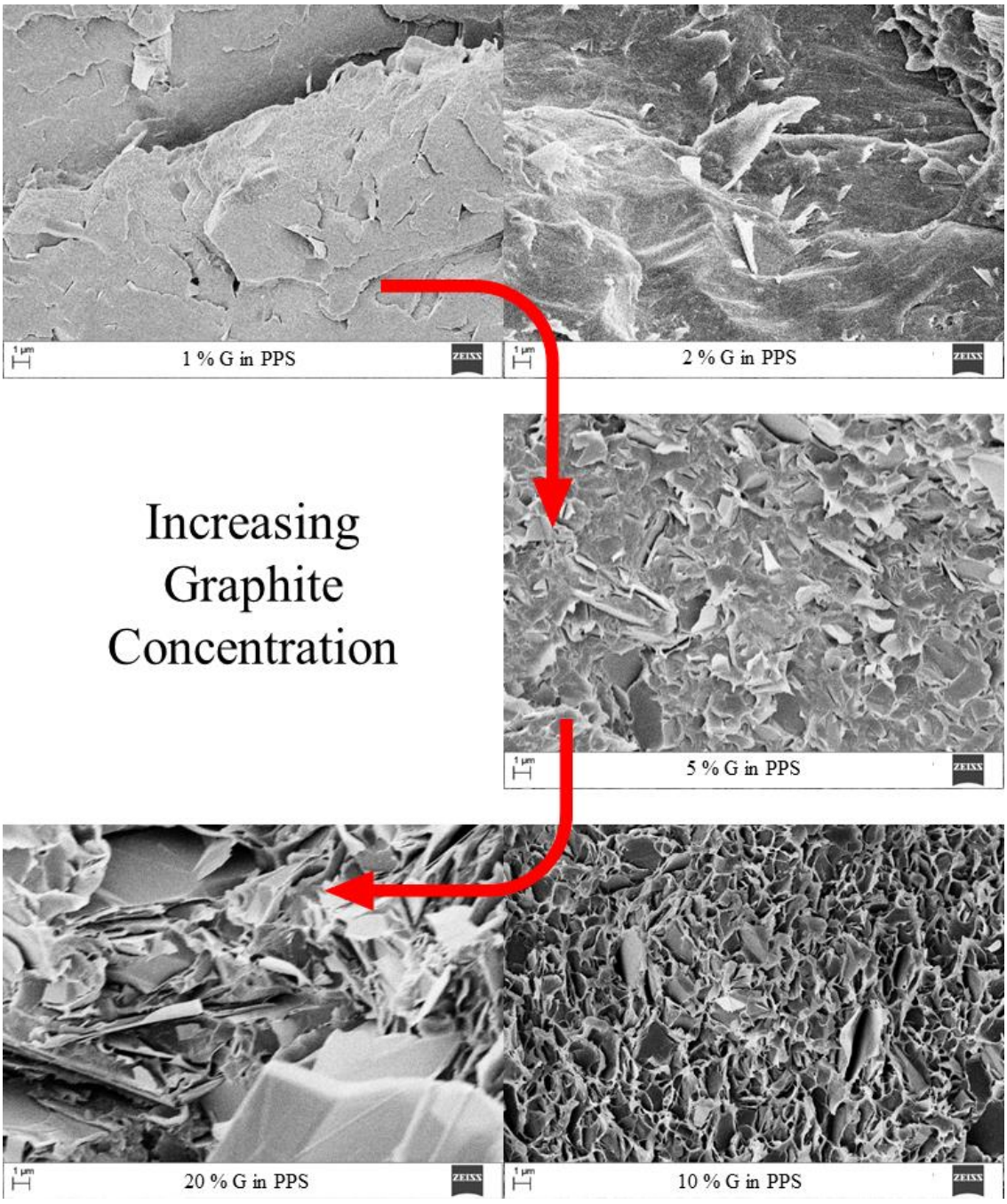

Figure 4-9 Scanning Electron Microscopy of G-PPS with increasing concentration of graphite at 10 KX and 5kV

From the XRD results, crystallization may occur on edge/steps on a particular crystal face (200). In our microanalysis, we observed adhesion of PPS on crystalline steps at high concentration of graphite, Figure 4-10. In the fractured surface, flake pullout leaves behind locked in graphite, adhering to the PPS. In the Figure, the PPS is observed as fibrils extending from the edges of isolated flakes. This acts as strong evidence of polymer functionalization to the created graphene. That in either concentration; adhesion (bonding) on the edge and surface is likely in these composites.

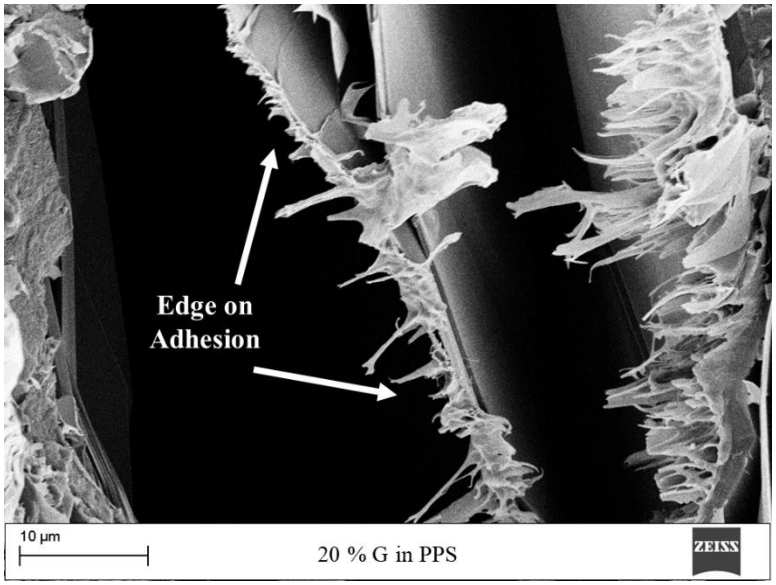

Figure 4-10 Scanning Electron Microscopy of edge functionalized graphite in 20 % G in PPS at 5KX and 5kV

An analysis of the fracture surface in Figure 4-11, shows graphene is identified by its substrate/matrix interaction. In Figure 4-11, the PPS matrix has features indicative of its extension from the cryo-fractured surface. A nanoflake of many layer graphene is identified by its jagged structure, as it is able to extend out of the matrix. Many layer graphene is very thin (20 nm, in this Figure) [109], but thick enough to structurally support itself. Single layer graphene is extremely thin, and requires a surface to provide

support. In Figure 4-11, graphene appears to adhere along the surface of the PPS, containing two strong indicators. The first indication are the 2 folds on the surface, indicated by the arrow [107], as it undergoes geometric reconstruction on the surface. The second indication is the wavy-like structure with its leading edge connected to a rolled flake extending from the surface. This wavy structure is found to be different than the polymer surface, which contains a series on striation supporting graphene sheets. These wavy features have been identified in previously constructed work of large exfoliated flakes on a PPS substrate. The wavy structure is due to an attempt of the graphene to match the lattice of the substrate [108] , creating free standing ridges. All things considered, substrate interactions are clues to the identification of graphene, with the surface structure having sensitivity to the level of adhesion.

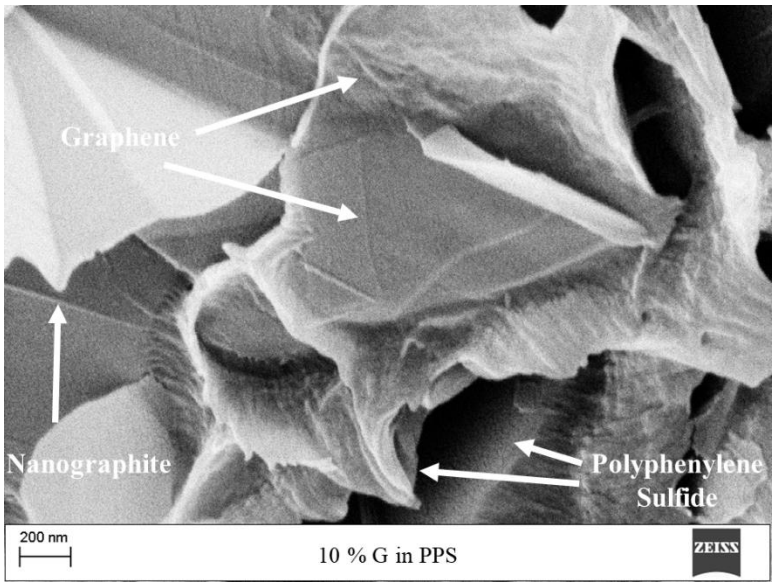

Figure 4-11 Scanning Electron Microscopy of surface and edge functionalized graphite in 10 % G in PPS at 100KX and 5kV

4.4 Interfacial Analysis

4.4.1 X-Ray Photoelectron Spectroscopy of PPS PMCs

In the analysis of XPS, binding energy shift and peak broadening act as clues to bond formation due to reinforced graphene in the matrix. In our analysis, the S2p Sulfur valence state of PPS was detected. A binding energy shift, equating to either oxidation or reduction of an analyzed valence state was observed. If there is a binding energy increase, oxidation is expected to be present. Oxidation leads to bonds forming at or near the sulfur in the PPS backbone. If there is a lowering in the binding energy, the reaction is reduction. Reduction leads to a depletion at or around the sulfur. In our analysis, XPS was conducted on PPS and 20 % graphite containing PPS. The results were used to identify the type of chemical bonds present, due to exfoliation.

Our results show PPS having two S2p peaks in Figure 4-12, corresponding to C-S and –SO- [109] [110]. Binding energies for PPS are found to be 163.73 eV (C-S) and 164.79 eV (-SO-). For the 20 % graphite containing PPS, 163.55 eV (C-S) and 164.56 eV (-SO-). In the pure PPS, –SO- appears broad, where the extended region leading to higher binding energies, extends beyond the 164 eV binding energy analyzed. The extended region in Figure 4-12, accounting for the broadness of the peak, suggests PPS is oxidized. PPS has unsaturated sulfur bonds, which are reactive to adsorbed oxygen [111], that occur by the low bond energy to C-S-C . In the graphene reinforced PPS, a lower binding energy leads to a reduction of the S2p. The S2p, reduction narrows the binding energy peak, eliminating the adsorbed oxygen. This suggests that graphene implants antioxidant properties to the PPS matrix.

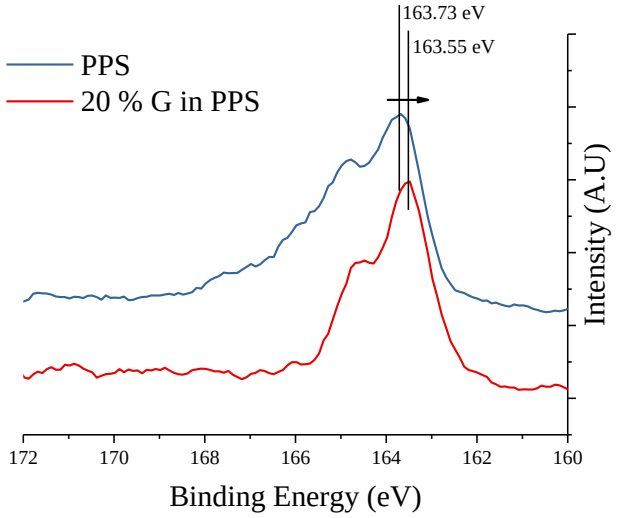

Figure 4-12 XPS of Sulfur S2p binding energy shifts in PPS and 20 % G in PPS

The reduction in the sulfur S2p suggested earlier, was due to a depletion at the sulfur in the backbone of PPS. In the 20 % graphite in PPS, phenylene interactions with the surface of graphene was suggested. These interactions simplify to π- π bonds formed between the interfacing surfaces. From the XPS results, a depletion of the S2p due to the π bonds formed. These π bonds cause a withdrawal of electron from the sulfur, reducing the binding energy. This withdrawal leads to noncovalent bonding in the graphene surface, as a dominant mechanism for adhesion. If covalent functionalization in the sulfur is available in higher concentrations, an increase in binding energy would be observed.

4.5 Mechanical Properties of PPS PMCs

4.5.1 ASTM D638 of PPS PMCs

In the drive to develop graphene reinforced polymer matrix composites, overall mechanical property improvement serves as the lynchpin for direct application. In the case of polymers, these properties tend to include stiffness improvements. Most polymers

are flexible and subject to deformation under load. By improving stiffness, polymer matrix composites can be designed for structural applications. ASTM D638 type 5 dogbones are tested parallel to the direction of flow. When looking at the modulus vs concentration in Figure 4-13, the modulus up to 5 % graphite by weight, have similar properties in both HS and LS. Increasing to 10 % by weight, the modulus shows an increase by 2 GPa in LS compared to HS. In the 10 % graphite containing PPS, the crystal domains are smaller in the HS system. Smaller grains are known to be tougher, while larger grains are much more stiff and brittle [112]. At 20 % graphite concentration, the modulus values drastically increase by 2.4 GPa suggesting there is better adhesion between the composite phases. The grains are still much smaller in the 20 % G-PPS HS, but the added adhesion to the exfoliated graphene creates better stress transfer. For polymers, good adhesion is achieved when effective lateral stress transfer between filler and matrix create a buildup of high strain energy density. The strain energy lead to a small internal main chain mobility, counteracting large axial chain stress. This characteristic lead polymer composites that undergo brittle fracture [113] [114]. If the modulus is reduced (less stiff); then there is a reduction in bonding between the matrix components and crystalline domains, allowing more plastic deformation [115]. Smaller crystalline domains may lead to lower crystallinity, which will ultimately improve the toughness of polymer composites.

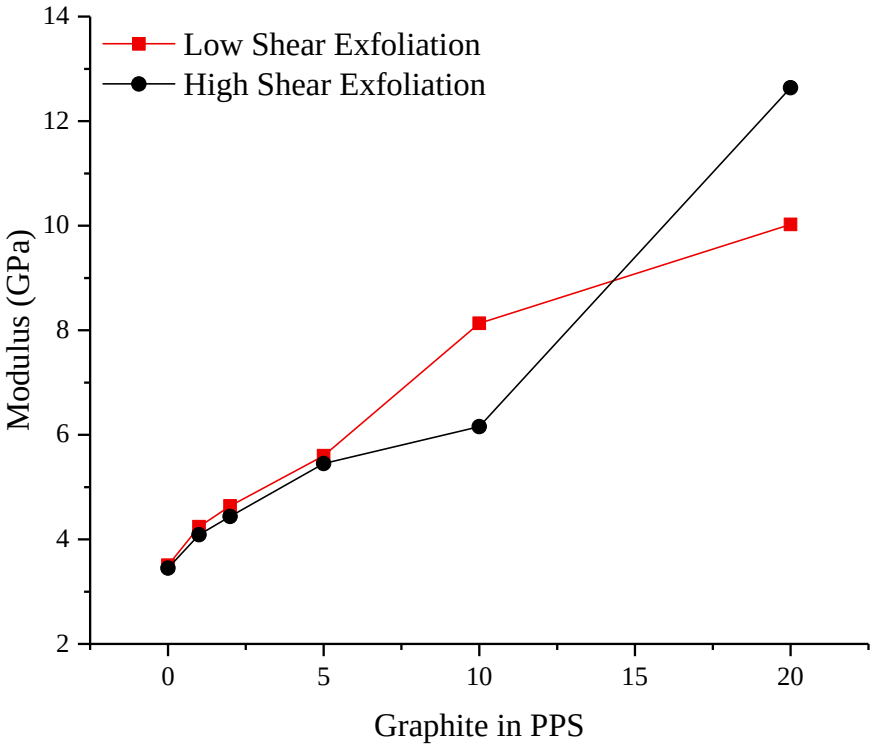

Figure 4-13 Elastic Modulus of PPS and G-PPS PMCs

Table 4-4 Mechanical Property result for PPS and G-PPS

Material	Peak Strain (%)	Peak Stress (MPa)	Modulus (GPa)
PPS LS	21.35 (6.64)	82.02 (1.06)	3.50 (0.05)
1 % G in PPS LS	2.40 (0.46)	77.96 (9.42)	4.24 (0.17)
2 % G in PPS LS	2.55 (0.21)	78.21 (2.99)	4.64 (0.08)
5 % G in PPS LS	1.79 (0.16)	69.55 (4.15)	5.60 (0.25)
10 % G in PPS LS	1.18 (0.21	64.94 (6.21)	8.13 (0.82)
20 % G in PPS LS	0.99 (0.21)	56.36 (4.23)	10.02 (0.82)
PPS HS	15.83 (7.67)	76.12 (5.44)	3.45 (0.25)
1 % G in PPS HS	3.32 (0.37)	81.06 (3.09)	4.09 (0.10)
2 % G in PPS HS	2.87 (0.42)	77.42 (2.66)	4.44 (0.07)
5 % G in PPS HS	1.94 (0.17)	68.09 (4.16)	5.45 (0.17)
10 % G in PPS HS	1.43 (0.41)	56.95 (8.09)	6.16 (0.82)
20 % G in PPS HS	0.76 (0.09)	65.09 (6.20)	12.64 (0.72)

4.6 Closure

A study of the effects of exfoliation to functionalization by high and low shear strain rate was conducted. Observed at low concentrations starting graphite concentrations and high shear strain rates (2876 s^{-1}) produced exfoliation dominated by edge and line defect adhesion, caused by dangling bonds created in-situ. This further developed to large conformational changes in PPS driven by PPS intercalation. Low shear strain rates (958 s^{-1}) led to smaller conformational effects dominated by outer surface fragmentation, also created dangling bonds leading to converted graphene. Diffusion dominated exfoliation was found to follow an exponential decay model, where the rate was dependent initial graphite concentration. Exfoliation also lead to the observation that there existed a variation in crystal domain aspect ratio of (110)/ (200) from the novel process. It is believed that a ratio > 1 is dominated by intercalation of the polymer within the graphite layers leading to π- π stacking by the phenyl group and < 1 is dominated by nucleation on line and edge defects by the increased amount of dangling bonds present in the composite. In the exfoliation process, graphene was observed by its interfacial characteristics to create folds and wavy structures. Comparing to the diffraction results by the two different shear rates, a plurality of graphene sizes were found with an overall approximation for domain size being 20 nm (002) by XRD. Graphene sizes smaller than the approximate value were found, highlighting the fact that using techniques like microscopy and spectroscopy are good in identifying the plurality of graphene flakes in the background of the diffraction data. The 20 nm size is a representation of an upper limit to crystalline domains in the (002) direction. Additionally, at the planar interface, functionalization was found to occur by π-π bonding

at the graphene surface, leading to noncovalent functionalization. The bonding was shown by the depletion of sulfur in the backbone of PPS, from the XPS results. The combination of functionalization, graphene in-situ exfoliation, and smaller polymer crystal domains lead to the development of a PPS composite with improved mechanical properties.

4.7 Supplemental Data

4.7.1 Differential Scanning Calorimetry Results

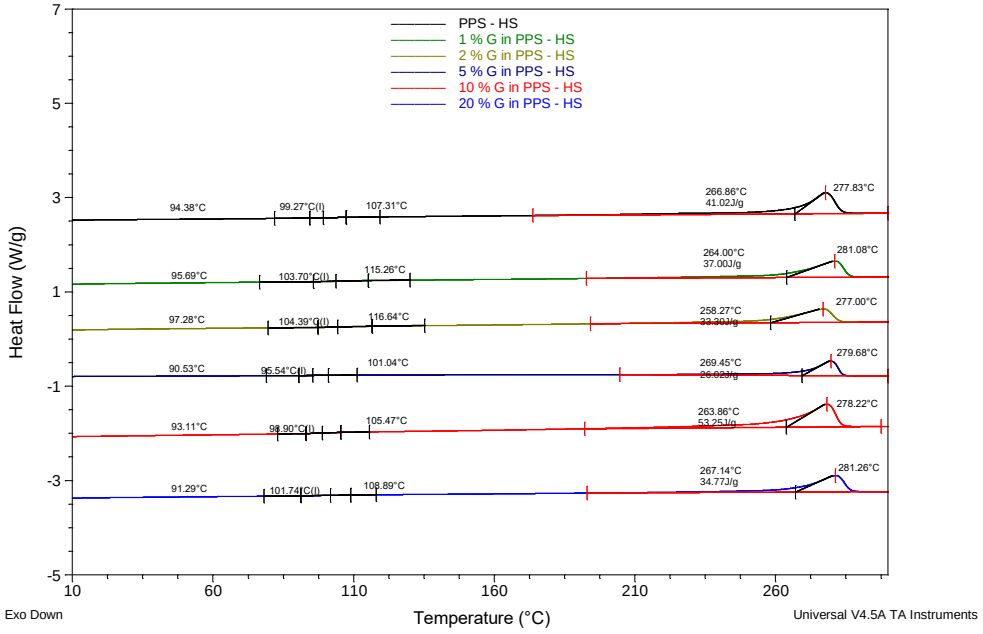

Figure 4-14 DSC heat ramp analysis results for PPS and G-PPS by HS

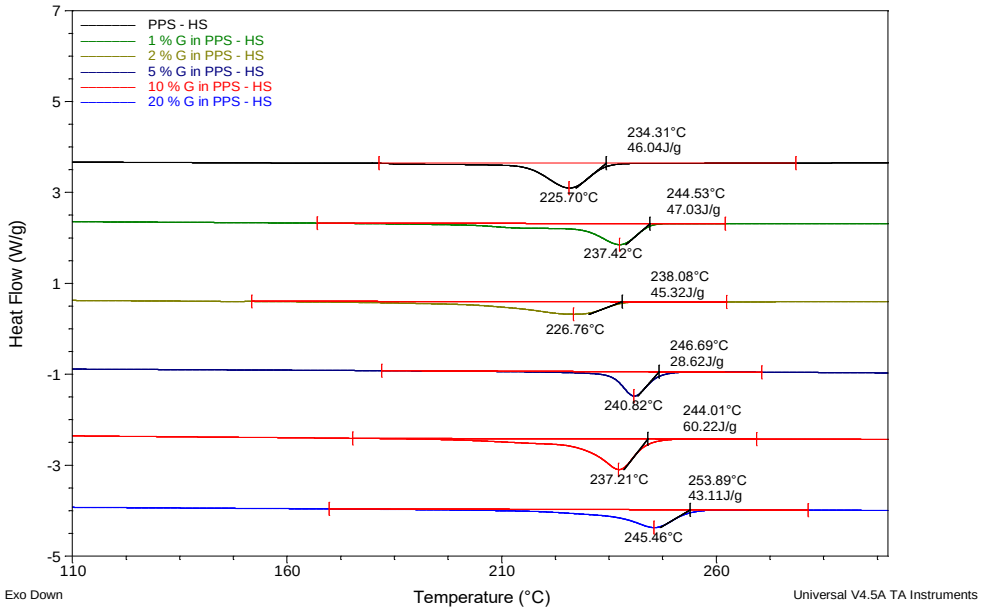

Figure 4-15 DSC cooling; analysis results for PPS and G-PPS by HS

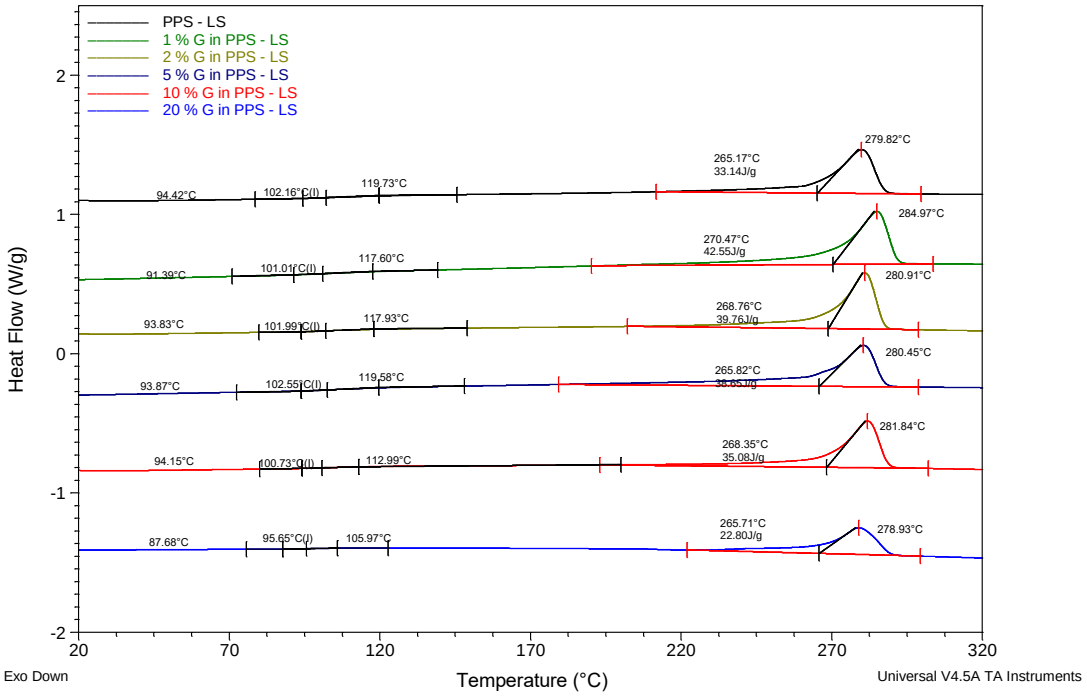

Figure 4-16 DSC heat ramp analysis results for PPS and G-PPS by LS

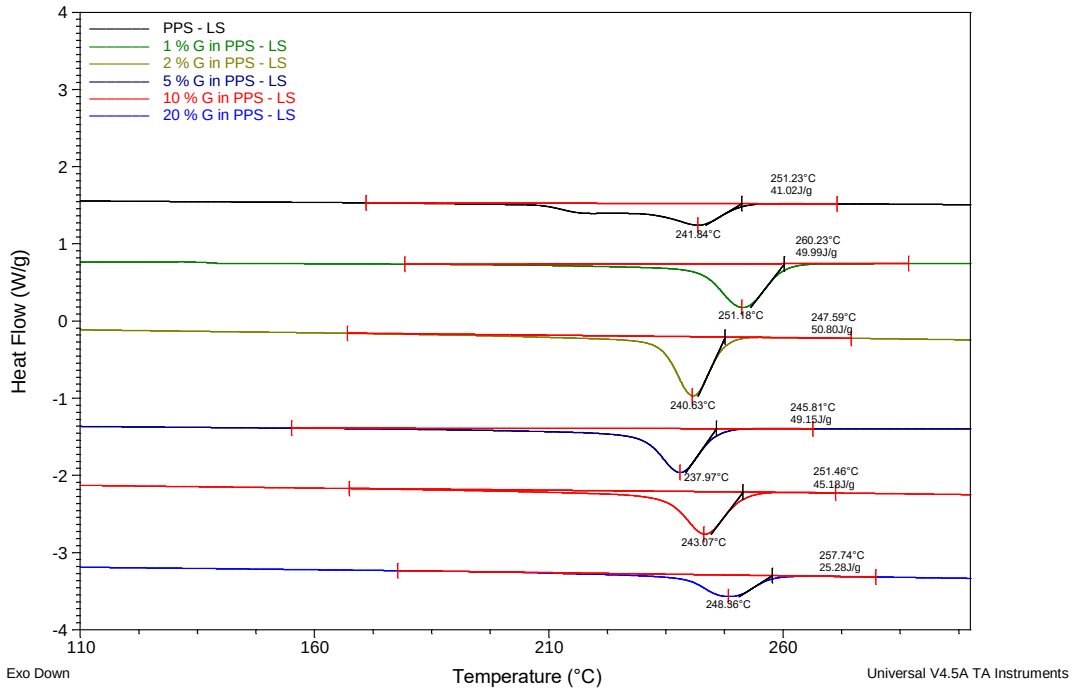

Figure 4-17 DSC cooling; analysis results for PPS and G-PPS by LS

Chapter 5 Polymer Deformation in Extensional flow

5.1 Summary

The application of extensional flow seeks to deform a molten polymer, decrease the conformational entropy, and increase the surface area for functionalization. In the deformation of polymer chains, a 1-D elongated polymer chain was created due to the development of an extensional flow generated in a process patented by Nosker et al [30]. The ability to functionalize and create a high surface area was observed by accessing the isothermal kinetic properties of deformed polymers. The theory suggests that high speed extensional flow in the process, given by a high shear strain rate, allows for a fully deformed high surface area polymer surface to be created. The created surface has a high surface energy, determined by kinetic processes. This high surface energy, working with the chemistry in the polymer backbone, creates instances for functionalization to take place. In this work, the activation energy difference in the polymer, frozen in place and relaxed, is measured. The activation energy is taken as a measurement of the potential energy stored into a spring. The side groups in the backbone are assumed to be available to an approaching surface, making reactivity possible.

5.2 Theoretical groundwork for activation energy to deformation

5.2.1 Revision of Deformation Model

One of the first instances to interpret the deformation and extension of an isolated polymer molecule was in the investigation of DNA. DNA is a long chain double helical biopolymer that maintains a random coil conformation, making internal portions of the

polymer unavailable. In sequencing DNA, elongational flow cells were designed to unravel and extend DNA to identify its base pairs. In these flow cells, the dynamics of single polymers were first analyzed by fluorescent markers in work done by Perkins [116] . De Gennes predicted for steady extensional flow, a coil stretch transition occurs for single polymers when the strain rate exceeds $\dot{\varepsilon} = 0.5\tau_1^{-1}$ where τ is the relaxation time for a polymer to return to its original position [117].

Looking at the force to stretch these coiled states, extension occurs when the hydrodynamic force (F_{hydro}) (2) exceeds the elastic restorative force of a polymer coil to return to its original position ($F_{elastic)}$ (3). The hydrodynamic force is governed by the shear rate $\dot{\gamma}$, viscosity η, and linear end-to-end distance r of the deformed polymer chain.

$$F_{hydro} = 6\,\pi\,\dot{\gamma}\,\eta\,r^2 \tag{2}$$

$$F_{elastic} = k_B T\left[\frac{3r}{Na} - \frac{2}{r}\right] \tag{3}$$

The elastic force of a polymer chain is dependent on average molecular kinetic energy terms k_BT (kB is the Boltzmann constant and T the absolute temperature), the end-to-end distance r, and to the overall polymer length as a multiple of the number of chain segments N to the segment length a. Knowing that polymer chains are flexible at its connected segment points, the interpretation is simplified to a persistent length model, negating the complexity of the segments. The persistent length model or worm-like chain model (WLC) made the contour length constant, having L = Na. In this interpretation, the hydrodynamic force is negated for using calorimetry results, but the elastic force is used under the assumption that energy is conserved.

Once these polymers or any spring is stretched and elongated, the molecule has stored potential energy. In the case of a modeled spring, the stored potential energy is U(x) = ½ k $x^{2;}$ where U(x) is based on the degree of displacement x, and a 'spring' restorative constant k. In this model, the force is conserved F_{con}, (4) such that it is represented by the potential energy change dU to the change in displacement dx; where the sign is negative due to the direction of energy conservation. An integration over the displacement, establishes that the amount of work (W) placed into the system due to the deformation is given by (5). Under a deformed polymer, equation (5) is the work that the system undergoes, by the investigation of the displacement states studied. Establishing a relation to the changed potential energy (ΔU) to the fluid force imparted on a polymer chain, causing it to deform.

$$F_{con} = -\frac{dU}{dx} \tag{4}$$

$$W = \int_1^2 Fcon\ dx = -\Delta U \tag{5}$$

5.2.2 Established Thermodynamic Understanding

Calorimetry experiments using DSC acquires results that help interpret the energy requirement of a reaction along a particular reaction pathway. In the case of the materials system studied in this research, glass transitions, endothermic (Melting) and exothermic (Crystallization) reactions are obtained. For any particular reaction, the number of active molecules that take part in a reaction pathway must pass over an initial energy barrier. This barrier is the amount of energy reactants must absorb to reach a final state product, deemed the activation energy E_a. In a reaction pathway, the energy difference between the starting

reaction and the end reaction is the enthalpy ΔH. In DSC, energetic differences between initial and final products across a complex pathway are trivial since these methods are straight forward. Activation energies on the other hand are more complex processes, which are both sensitive to heating rate and pathway.

Based on experimental setup there are three thermally reactive phenomena we are analyzing for activation energy using DSC, for a polymer. These phenomena include glass transition, recrystallization temperature, and melting temperature. These act as interpretations for the mechanical response of deformed polymer chains. They are broken down as modes to stress relaxation of deformed chains and the microstructures they create.

The glass transition temperature equates to the phase change of a material that goes from a rubbery state to rigid glassy state. This transition expresses itself as being sensitive to material properties, where most polymers are very rigid above T_g and more compliant below T_g. A molecular understanding of the glass transition is the onset of molecular motion acting as the beginning stage of reptation [118] . An expanded view, in the context of amorphous polymers, the glass transition is an α relaxation phenomena associated with large scale group motion along the polymer chain axis. The scale of group motion occurs over a temperature range, where stress relaxation speeds up. This reduces steric hindrances that change the effective volume of the polymer chain [119].

For deformed polymer morphologies due to in process strain, anisotropic grains or metastable fibrous structures are created in semi crystalline polymers. Reorganization of low temperature deformed structures result in the reorganization or reformation of stable crystals. This process is deemed recrystallization, since it results in crystallization from a

pre-oriented structure. In all cases, recrystallization is process dependent, which is sensitive to thermal history.

The Temperature at which a crystalline region is in thermodynamic equilibrium with the melt phase is considered melting. In a semi-crystalline polymer, the equilibrium melting temperature is dependent on the lamellar thickness Figure 5-1, where thicker lamella sections increase the equilibrium temperature. Melting does occur over a large range and is not statistically defined by a single value. This being said, a range of lamella sizes exist in the extent of a semi-crystalline polymers, suggesting a broad distribution of sizes.

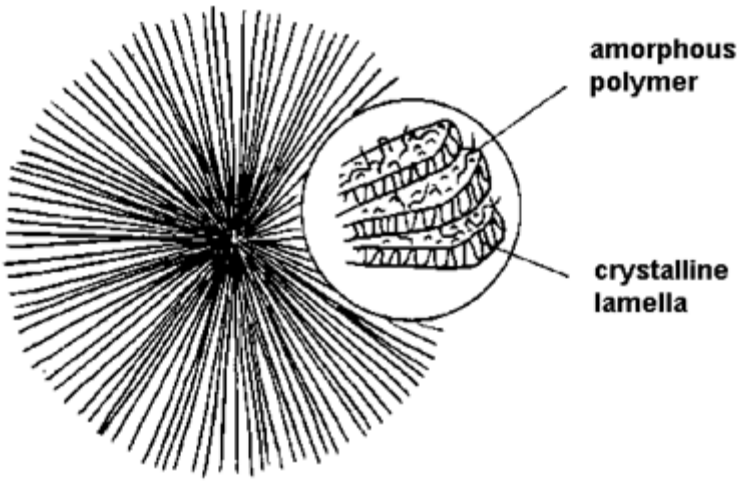

Figure 5-1 Unoriented polymer spherulite showing amorphous and lamella structure.

Interpreting the calorimetry results for given thermal transitions, the activation energy serves as a representation of the potential energy or stored elastic energy for endo and exothermic reactions Figure 5-2. Based on the experimental procedures, the thermoactive phenomena of T_g, T_r, and T_m represent stored potential energy generating

modes of stress relaxation to melting. In the case of the semi-crystalline polymers, the increase temperature quantifies the degree of molecular motion; where $T_g < T_r < T_m$. The variation in potential energy of the system, as stated earlier, represents the work applied or generated from the system. These values are then used as energetic quantities, sensitive to the degree of deformation of an extended polymer, and results in causing an increased potential energy change. In the case of the glass transition temperature, which represents molecular motion over a temperature range, steric hindrance plays a part in the interpretation of activation energy. Therefore, the degree of reptation should be sensitive to in-process and microstructural changes.

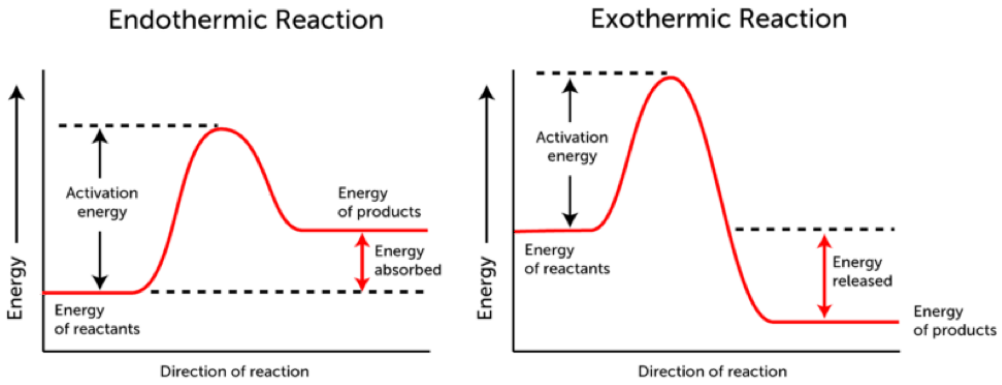

Figure 5-2 Energy vs reaction pathway for endothermic and exothermic reactions

5.2.3 Derived Kissinger Method

Kissinger developed a non-isothermal method to obtain the kinetic parameter of solid state reactions, without knowing information on the reaction mechanism. The method allows one to evaluate the activation energy from a linear regression dependent on the heating rate (Q) and the equilibrium reaction temperature (T_m , T_r, or T_g) [120]. Kissinger devised a set a rules to validate his method [121] .

(1) The expression of the rate of a reaction, given as a function of temperature and conversion, is separable. In this expression the kinetic constant is a function of temperature *k* (T) and conversion and function of conversion *f*(x)

$$c = \frac{dx}{dt} = k\,(T) * f(x) \tag{6}$$

(2) The kinetic constant is an exponential function to the product of reciprocal temperature (T) to the gas constant. Likened to the Arrhenius equation, the exponential term yield the activation energy Ea.

$$k = k_0 \exp\left(\frac{-Ea}{RT}\right) \tag{7}$$

(3) Test are conducted at a constant heating rate Q and can't be applied to processes involving cooling

$$Q = \frac{dT}{dt} > 0 \tag{8}$$

(4) The rate of reaction at constant heating rate Q is a function of temperature and has a relative maximum in the interval under study; at equilibrium temperature (T_m , T_r, or T_g) & dc/dT = 0

(5) Rate of variation of the kinetic function *f(x)* at equilibrium temperature is q = *(df/dx)* < 0.

By these methods Kissinger showed

$$\frac{Q*\mathrm{Ea}}{RT} = -Qk_0 \exp\left(\frac{-Ea}{RT}\right) \tag{9}$$

Or

$$\frac{d\ln(\frac{Q}{T^2})}{d(\frac{1}{T})=} = - \frac{Ea}{R} \quad (10)$$

A plot of (10) of $\ln(\frac{Q}{T^2})$ vs $(\frac{1}{T})$ produces a slope of Ea/ R where Ea is the activation energy

5.3 Materials and Method Review

Polysulfone (PSU) and Polyphenylene Sulfide (PPS) were deformed under high speed extensional flow, generating 2 shear strain rate regimes. The strain rates were created by deforming the molten polymers at maximum shear strain rates of 985 s^{-1} and 2876 s^{-1}. The molten polymer, under these conditions were extruded into a bath of liquid nitrogen to freeze the microstructure in place; at mixing conditions. The remainder of the extrudate under the same conditions were allowed to cool to room temperature onto a glass slide, without any additional conditioning.

Prepared polymer samples were characterized using DSC at heating rates of 10, 20, and 30 °C/min. The glass transition temperate (T_g), recrystallization temperature (T_r), and melting temperature (T_m) for each rate, in Table 5-1 and Table 6-2. The results of the corresponding calorimetry experiment were analyzed.

Table 5-1 Calorimetry Results for Polyphenylene Sulfide

Material	Q	T_g (K)	ΔH_r (J/g)	T_r	T_m (K)	ΔH_m (J/g)
Cryogenically frozen PPS (HS)	10	363.79	29.11	400.77	552.81	42.65
	20	365.09	28.17	405.37	551.47	40.13
	30	366.28	25.18	408.50	549.72	37.89
Room Temperature PPS (HS)	10	363.67	31.29	401.03	551.43	42.83
	20	364.92	28.66	405.85	551.35	41.78
	30	365.09	29.65	408.88	549.34	40.50
Cryogenically PPS (LS)	10	363.53	30.21	400.66	554.23	40.71
	20	364.65	35.50	405.59	552.39	47.87
	30	366.10	29.04	409.64	553.84	38.77
Room Temperature PPS (LS)	10	363.81	34.11	400.77	554.07	45.47
	20	365.03	30.69	405.51	552.61	40.94
	30	365.81	29.84	408.99	551.59	38.62

Table 5-2 Calorimetry Results for Polysulfone

Material	Q	T_g (K)
Cryogenically frozen PSU (HS)	10	457.01
	20	458.53
	30	460.13
Room Temperature PSU (HS)	10	458.57
	20	460.50
	30	459.67
Cryogenically frozen PSU (LS)	10	459.07
	20	459.51
	30	461.13
Room Temperature PSU (LS)	10	459.05
	20	460.48
	30	460.75

The ln (Q/T^2) vs 1000/ T were calculated at their thermal equilibrium temperatures for both polymers observed. The results were labeled in in Table 5-3 and Table 5-4

Table 5-3 Results for Kissinger Plot for Polyphenylene Sulfide

Material	Q	ln (Q/T_g^2)	$10^3/T$ (T_g)	ln(Q/T_r^2)	$10^3/T$ (T_r)	ln (Q/Tm^2)	$10^3/T$ (T_m)
Cryogenically frozen PPS (HS)	10	-9.491	2.749	-9.684	2.495	-10.327	1.809
	20	-8.805	2.739	-9.014	2.467	-9.630	1.813
	30	-8.406	2.731	-8.624	2.448	-9.218	1.819
Room Temperature PPS (HS)	10	-9.490	2.750	-9.686	2.494	-10.322	1.814
	20	-8.804	2.740	-9.016	2.464	-9.629	1.814
	30	-8.399	2.739	-8.626	2.446	-9.216	1.820
Cryogenically PPS (LS)	10	-9.489	2.751	-9.684	2.496	-10.333	1.804
	20	-8.802	2.742	-9.015	2.466	-9.633	1.810
	30	-8.405	2.732	-8.629	2.441	-9.233	1.806
Room Temperature PPS (LS)	10	-9.491	2.749	-9.684	2.495	-10.332	1.805
	20	-8.804	2.740	-9.015	2.466	-9.634	1.810
	30	-8.403	2.734	-8.626	2.445	-9.224	1.813

Table 5-4 Results for Kissinger Plot for Polysulfone

Material	Q	ln (Q/T_g^2)	$10^3/T$ (T_g)
Cryogenically frozen PSU (HS)	10	-9.947	2.188
	20	-9.260	2.181
	30	-8.862	2.173
Room Temperature PSU (HS)	10	-9.954	2.181
	20	-9.269	2.172
	30	-8.860	2.176
Cryogenically frozen PSU (LS)	10	-9.956	2.178
	20	-9.265	2.176
	30	-8.866	2.169
Room Temperature PSU (LS)	10	-9.956	2.178
	20	-9.269	2.172
	30	-8.865	2.170

Data in Table 5-3&5-4 were plotted and the results were fit with a straight line to acquire the activation energy for the calorimetry results Figure 5-3.

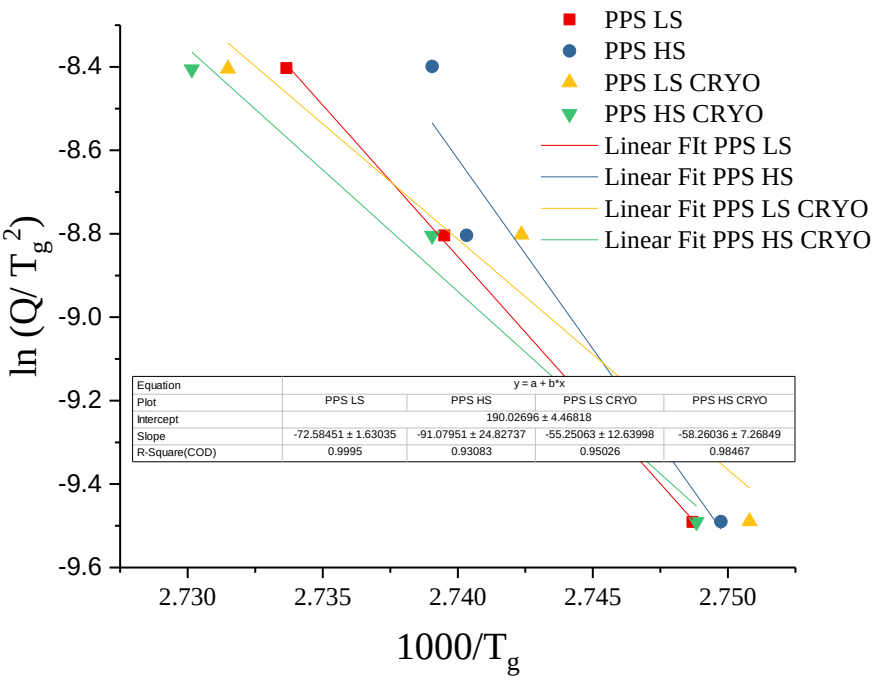

Figure 5-3 Kissinger plot for PPS glass transition temperature

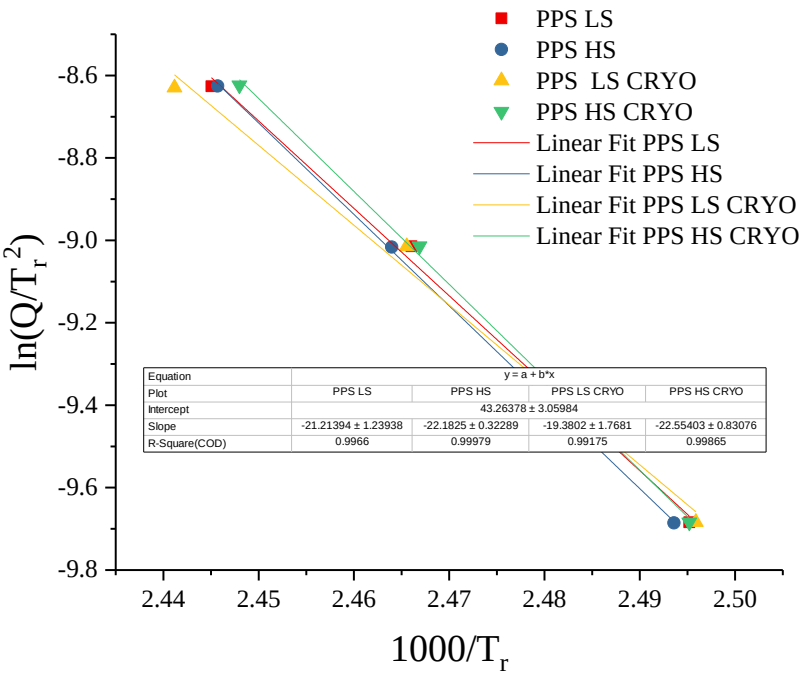

Figure 5-4 Kissinger plot for PPS recrystallization temperature

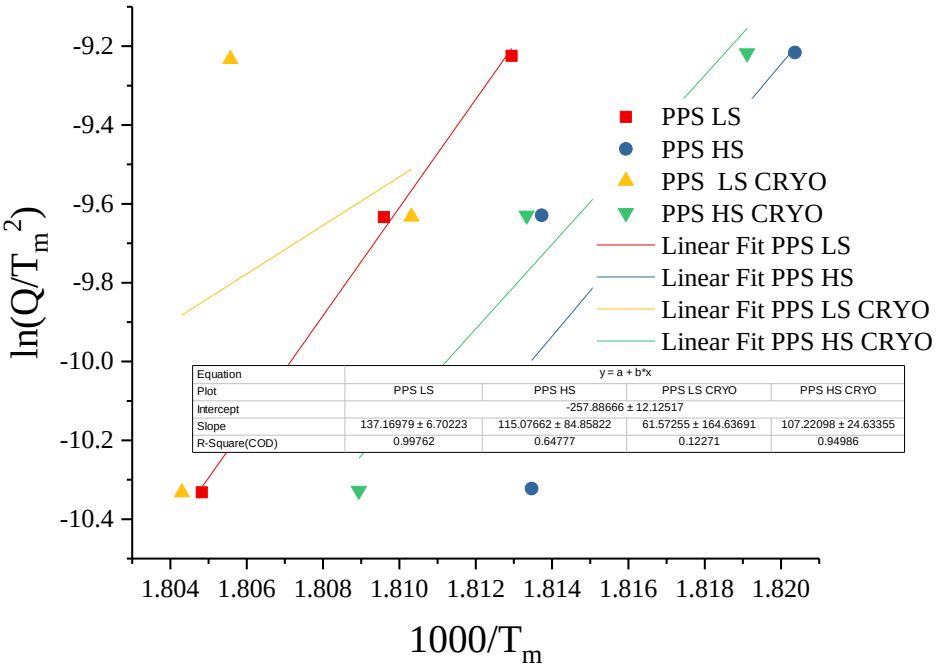

Figure 5-5 Kissinger plot for PPS melting temperature

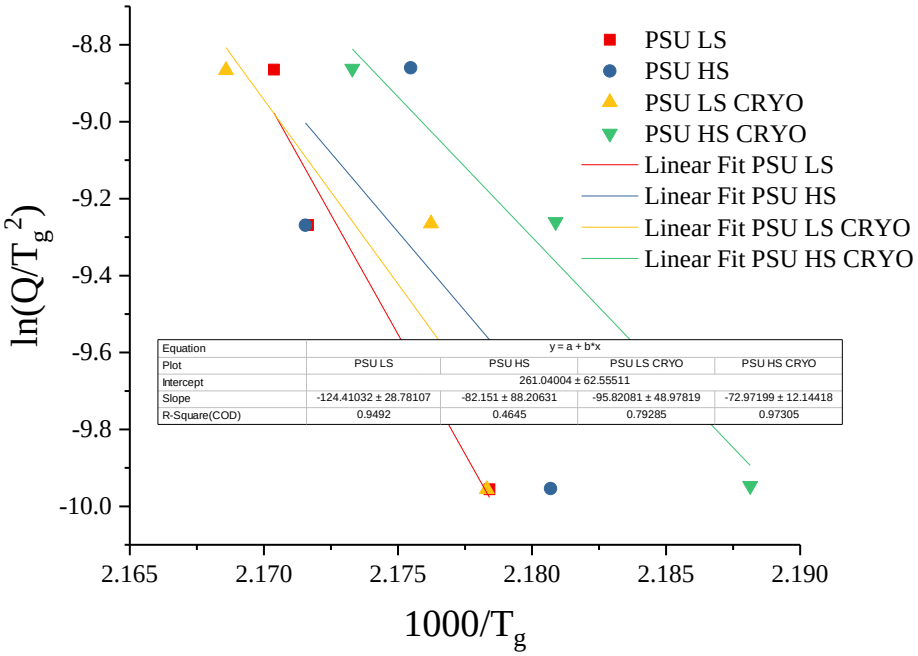

Figure 5-6 Kissinger plot for PSU glass transition temperature

The results of the slope from the linear equation were multiplied by the gas constant R to acquire the activation energy in kJ/mol.

5.3.1 Interpretation of changes in glass transition of PPS & PSU

Glass transition action energy is an interpretation of structural relaxation energy of the tested matrix. Looking at the activation energy of PPS of just the room temperature cooling process by shear strain rates of ~1000 s^{-1} (LS) to ~3000 s^{-1}(HS), the energy to cause molecular motion is higher in PPS HS than PPS LS Table 6-5. In the higher shear strain rate, the results cause a greater degree of chain deformation due to the increased force used to extend the polymer. The increase in activation energy suggests that the chains are interacting with adjacent chains in the matrix, causing steric hindrance that are perturbing molecular motion. Observing the effects in the cryogenically frozen structure (LS/HS CRYO), the overall activation energy is much less that the PPS that is cooled down to room temperature. Lower activation energy suggests an increase in free volume and less steric hindrance for molecular motion to occur. This agrees with models of glass transitions and free volumes studied by forming glasses by differing cooling rates; Nosker [122].

Comparing the activation energy difference between HS and LS, the difference in molecular motion yields the high speed shear process having large changes in potential energy. Previously we've equated this as representing the quantification of work in the system. For glass transition, the work term equates to the amount of energy for a volumetric change to relieve stress of a constrained chain. In this case, a change in potential energy represents a volumetric displacement. Interpreting this as displacement

producing steric hindrances, the HS process has highly deformed polymer chains. The extensional flow created conformational changes in the polymer, reducing the radius of gyration. This may bring the chains closer, cause confinement by chain-chain self interactions. The greater change in HS suggests that there is a greater interaction due to proximity effects by reduced radius of gyration.

Table 5-5 Activation Energy T_g of PPS (kJ/mol)

Material	**E_a of Tg for PPS (x 10^{-1})**	**Change in E_a (x 10^{-1})**
PPS LS	60 (14)	-14
PPS LS CRYO	46 (11)	
PPS HS	76 (21)	-27
PPS HS CRYO	48 (6)	

For PSU, the opposite occurs, with the activation energy comparing the high and low shear strain rate. PSU is rigid in terms of its polymer backbone, which can aid in its increased activation energy. Due to the effects of extensional flow, polymer chains extend more effectively due to highly deformed flow. In the case of PSU, as amorphous polymers are extended in a highly deformed state, the activation energy is lower. This occurs 1st by having stiff, untangled chains, and 2nd to its lack of interacting side groups. The least deformed PSU is much further entangled, creating an effectively higher activation energy.

Table 5-6 Activation energy PSU Tg (kJ/mol)

Material	**E_a of Tg for PSU (x 10^{-1})**	**Change in E_a (x 10^{-1})**
PSU LS	103 (24)	24
PSU LS CRYO	80 (41)	
PSU HS	68 (73)	8
PSU HS CRYO	61 (10)	

Comparing the activation energies for the change in potential energy of the system, we see that work is much lower in the HS system than the LS. The reduced work required for the volumetric change suggests that the system is more oriented and less entangled. A greater degree of entanglement raises the work requirement to change these kinetic parameters.

5.3.2 Recrystallization Activation Energy

In the case of recrystallization, the activation energy is interpreted as the recovery deformation of a metastable crystalline system in PPS. These systems can be looked at as crystalline stress relaxation of a deformed spring. When looking at the activation energy of HS and LS Table 5-7, HS has the higher activation energy when full chain extension is present. In comparing the activation energy difference to the work placed into the system, the reduced work suggests that the polymer is already fully extended and the recoverable energy is low; this effect due to the high extension of the flow. In the case of LS, which is less deformed, the work for crystallization recovery is greater. If we interpret activation energy of this process as volumetric changes, LS CRYO has a larger frozen-in volume than HS CRYO. When it cools by a non-cryogenic process, there is more time for stress relaxation to cause structural impingement of the metastable crystals. The HS process causes severe extension of the polymer. This leads to steric hindrances to recover elastic deformation.

Table 5-7 Activation Energy Tr of PPS (kJ/mol)

Material	**E_a of Tr for PPS (kJ/mol) (x 10^{-1})**	**Change in E_a (x 10^{-1})**
PPS LS	18 (1)	2
PPS LS CRYO	16 (1)	
PPS HS	18 (0.2)	-0.3
PPS HS CRYO	19 (0.6)	

5.3.3 Melting Activation Energy

Melting is interpreted as an expansion of the recrystallization interpretation, but expands on changes of the lamellar structure. In melting, there is the onset of larger scale molecular motion of polymer chains, leading to the destruction of crystalline regions. When detailing the difference between the HS and LS method undergoing room temperature cooling, the activation energy is larger in LS. The LS process is able to form larger crystals in the lamellar structure due to the low deformation of extension. In the HS method, the activation energy is lower due the smaller size of the developed crystals.

Comparing the change in potential energy of the two processes from the cryo to room temperature cooled methods, the work energy to melt is less in HS than LS. Lower potential energy can be interpreted as the polymer is already massively strained, so the recovery effort of an already deformed system is low. For the potential energy for LS to melt, the difference in activation energy is the available work that can be placed into a system to further crystalize. When there is less work available in HS, this suggests a highly deformed system requires less work due to non-recoverable deformation.

Table 5-8 Activation Energy Tm of PPS (kJ/mol)

Material	**E_a of Tm for PPS (kJ/mol) (x 10^{-1})**	**Change in E_a (x 10^{-1})**
PPS LS	-114 (6)	

PPS LS CRYO	-51 (137)	63
PPS HS	-96 (71)	7
PPS HS CRYO	-89 (20)	

5.4 Closure

5.4.2 Expansion of results to include revision of previous model

Taking the previous interpretation of the polymer behaving as a WLC (Work-like Chain) with non-interacting side groups, it suggests that this method has to be updated. When dealing with semi-crystalline vs amorphous polymers, highly deformed semi crystalline polymers are more likely to create interactions due to a high surface area created by extension, in addition to side group interaction due to its desire to form a crystal by secondary bonding (Hydrogen, Van der Waals, or π). In amorphous polymers, extension leads to reduce entanglements, creating a rigid 1-D surface that is easier to separate, but less interactive by its noncompliant backbone. The model suggests that a 1-D or highly extended polymer is created but chain flexibility plays a strong role in secondary effects, once extended.

A caveat to this method is the conservation of elastic force in extension. Once these polymer chains are deformed in extensional flow, the expectation that they will fully recovery once under stress relaxation. In each case, a small elastic deformation leads to a lower potential energy in each of the systems. These small potential energy changes can equate to a loss in the conserved force response of a stress relaxed polymer. The potential energy change leading to a loss in work is likely due to pinning of the microstructure by steric hindrances; once the polymer is fully extended. Accounting for the loss in energy may lead to a secondary indication of bonds formed or broken in the

process. This may result to more information of the possible chemical changes due to extensional flow; which requires further investigation

5.5 Supplemental Information

DSC Data

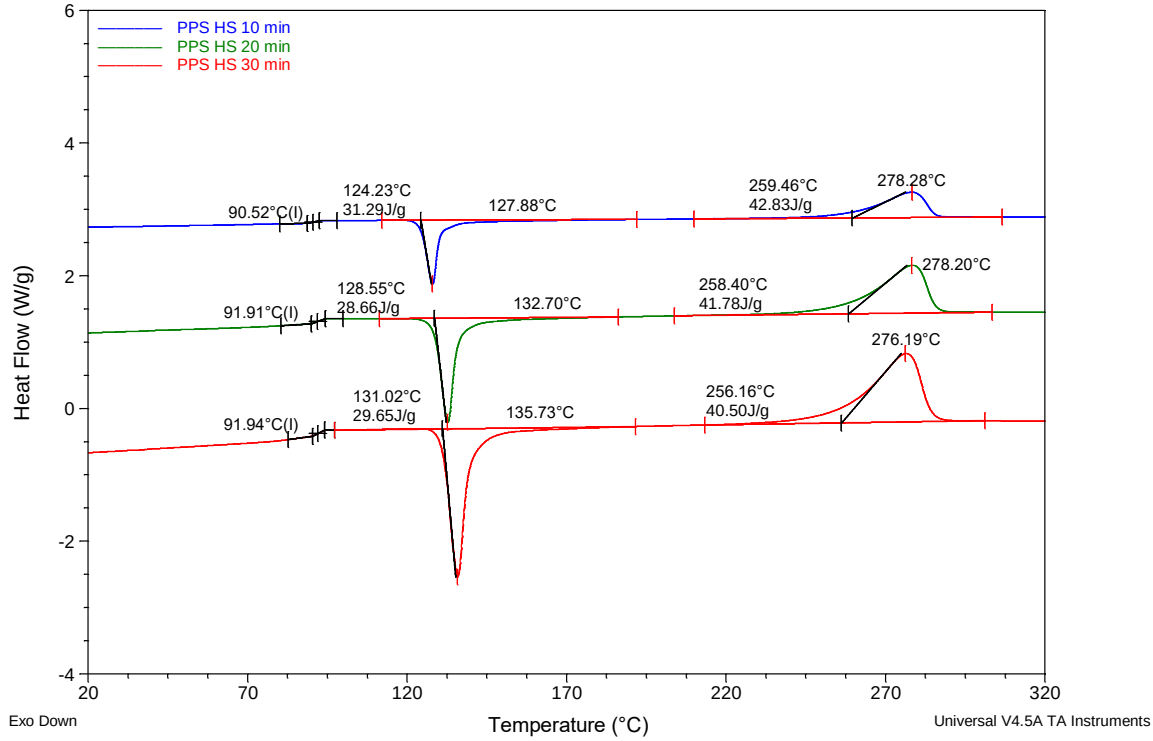

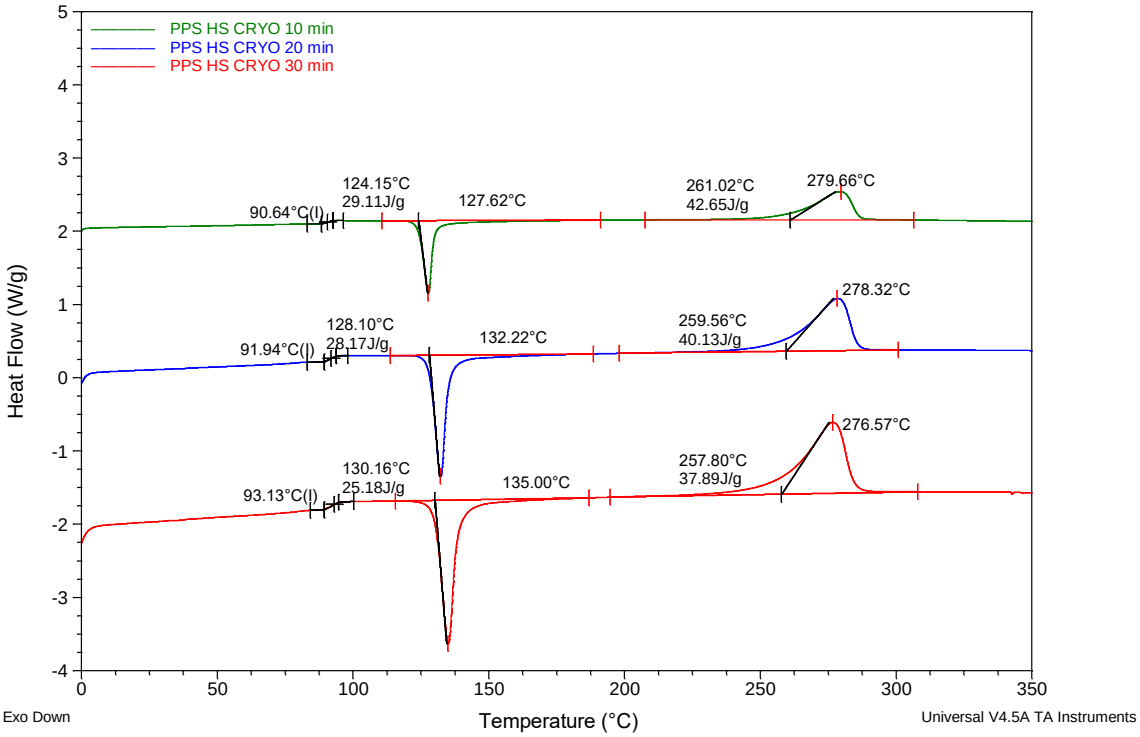

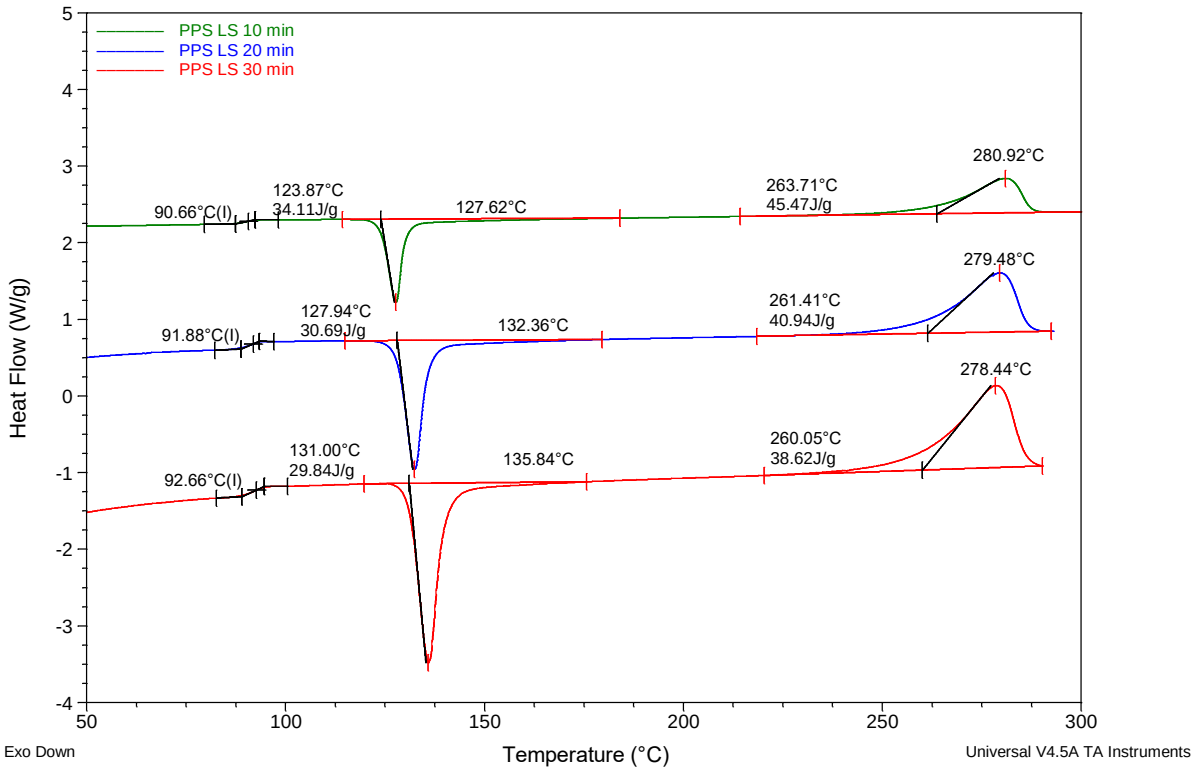
PPS LS 10 min
PPS LS 20 min
PPS LS 30 min
90.66°C(I)
123.87°C
34.11J/g
127.62°C
263.71°C
45.47J/g
280.92°C
91.88°C(I)
127.94°C
30.69J/g
132.36°C
261.41°C
40.94J/g
279.48°C
92.66°C(I)
131.00°C
29.84J/g
135.84°C
260.05°C
38.62J/g
278.44°C
Heat Flow (W/g)
Temperature (°C)
Exo Down
Universal V4.5A TA Instruments

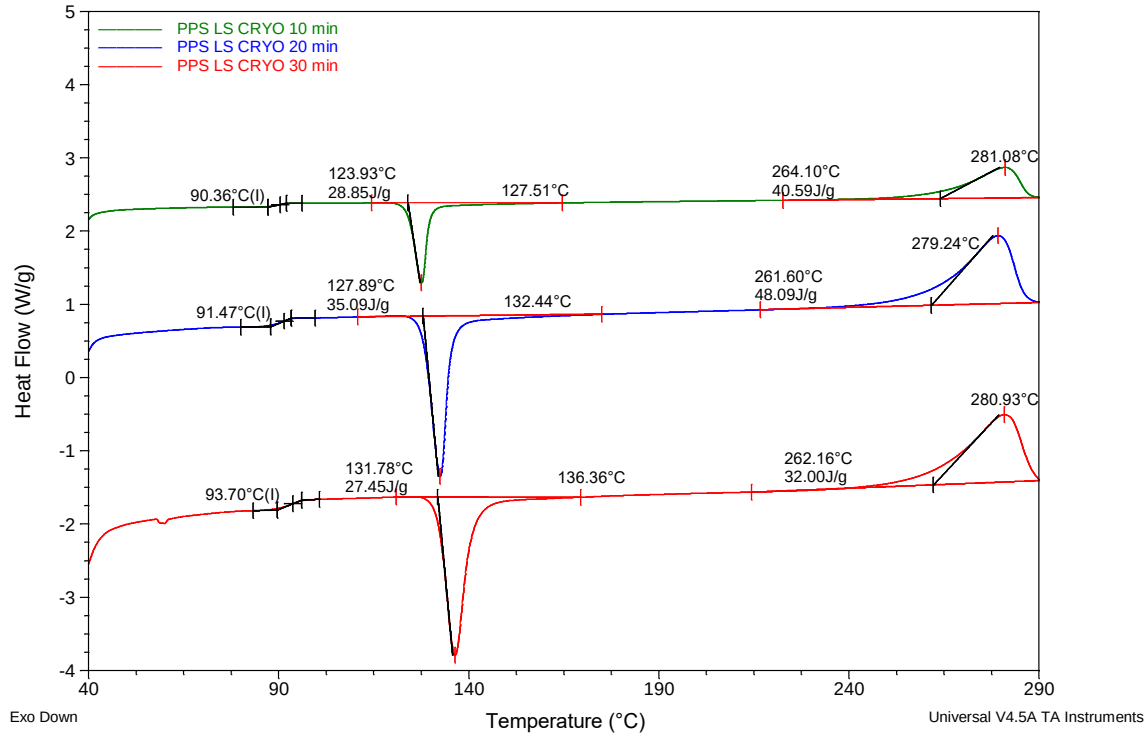
PPS LS CRYO 10 min
PPS LS CRYO 20 min
PPS LS CRYO 30 min
90.36°C(I)
123.93°C
28.85J/g
127.51°C
264.10°C
40.59J/g
281.08°C
91.47°C(I)
127.89°C
35.09J/g
132.44°C
261.60°C
48.09J/g
279.24°C
93.70°C(I)
131.78°C
27.45J/g
136.36°C
262.16°C
32.00J/g
280.93°C
Heat Flow (W/g)
Temperature (°C)
Exo Down
Universal V4.5A TA Instruments

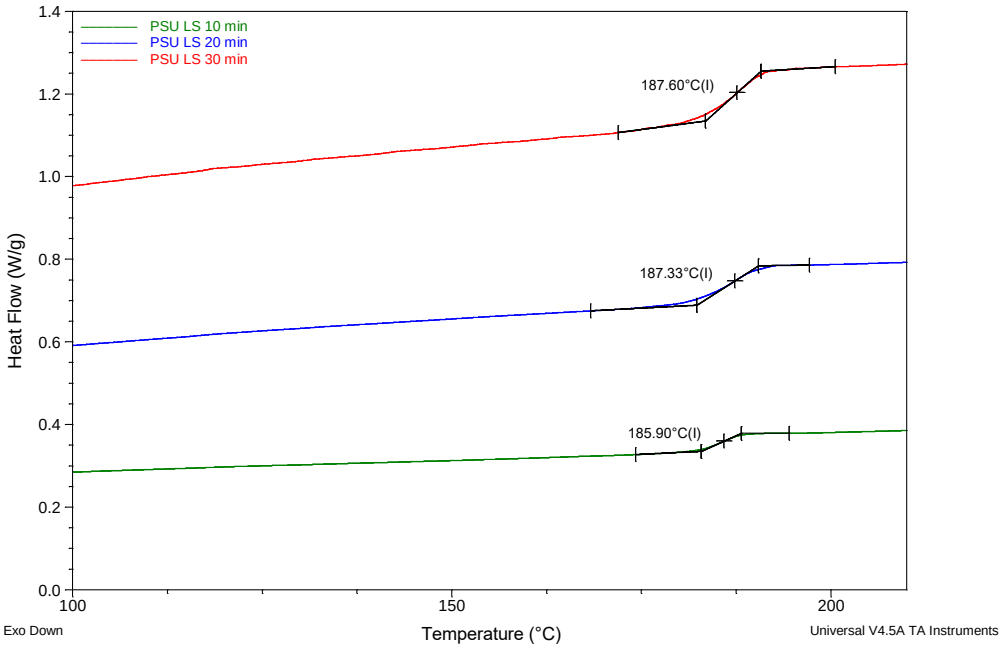
PSU LS 10 min
PSU LS 20 min
PSU LS 30 min
187.60°C(I)
187.33°C(I)
185.90°C(I)
Heat Flow (W/g)
Temperature (°C)
Exo Down
Universal V4.5A TA Instruments

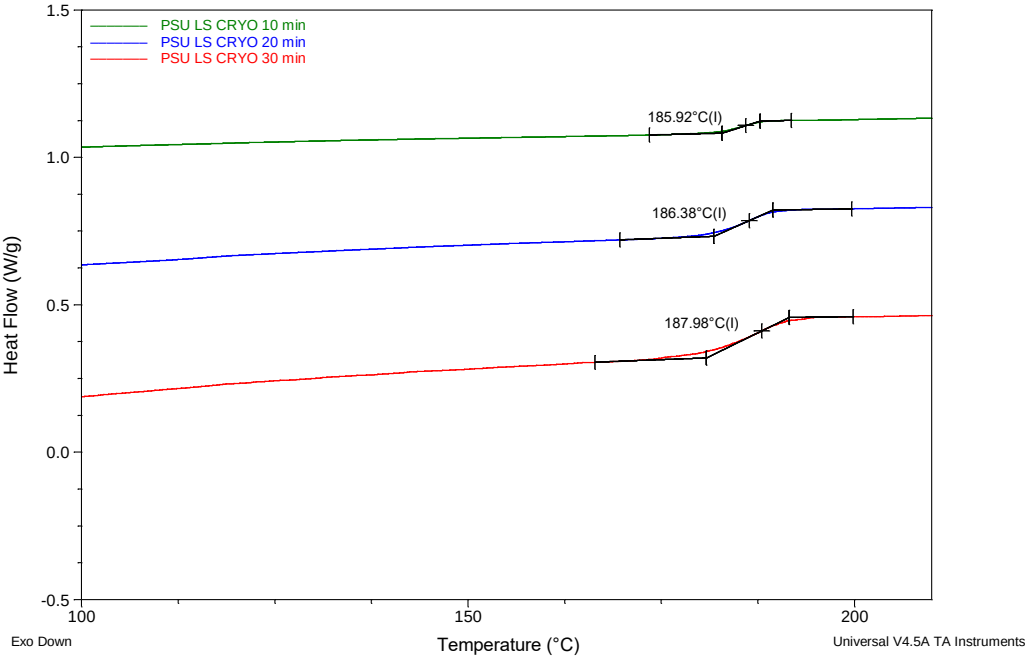
PSU LS CRYO 10 min
PSU LS CRYO 20 min
PSU LS CRYO 30 min
185.92°C(I)
186.38°C(I)
187.98°C(I)
Heat Flow (W/g)
Temperature (°C)
Exo Down
Universal V4.5A TA Instruments

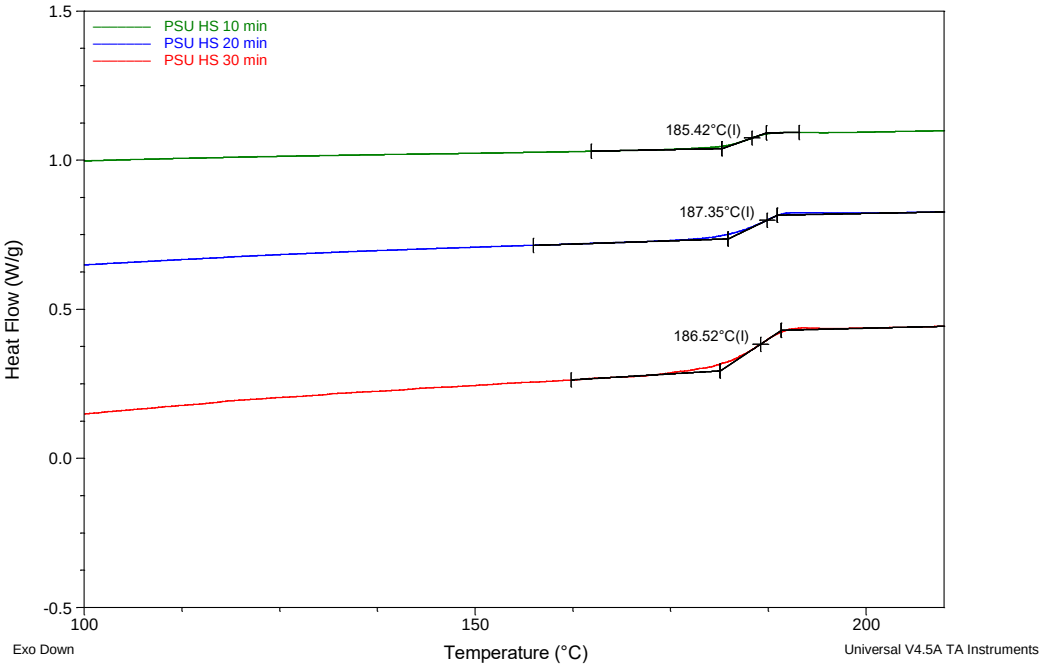
PSU HS 10 min
PSU HS 20 min
PSU HS 30 min
185.42°C(I)
187.35°C(I)
186.52°C(I)
Heat Flow (W/g)
Temperature (°C)
Exo Down
Universal V4.5A TA Instruments

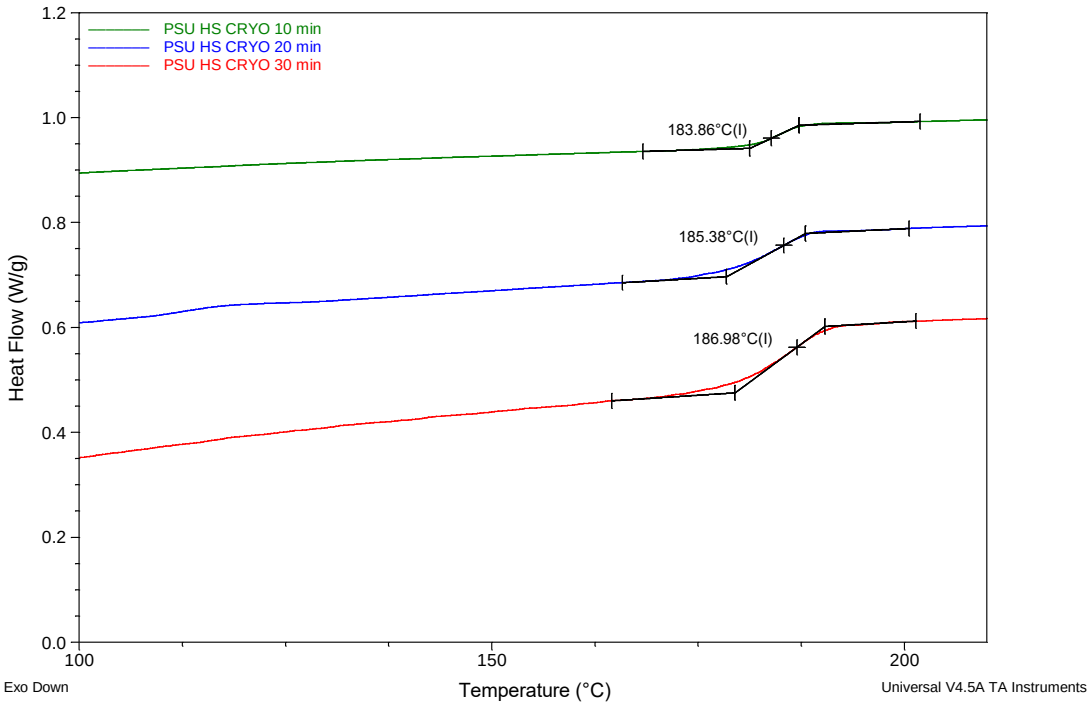
PSU HS CRYO 10 min
PSU HS CRYO 20 min
PSU HS CRYO 30 min
183.86°C(I)
185.38°C(I)
186.98°C(I)
Heat Flow (W/g)
Temperature (°C)
Exo Down
Universal V4.5A TA Instruments

Chapter 6 Time Dependent Exfoliation of Graphene Reinforced Polyamide Composite

6.1 Summary

Graphene has been known as exceptionally strong, superconductive, and an extremely thin material that imparts fantastic properties to any application [1, 8, 123]. As this material is being researched for a number of applications, and fields of use, interfacial characteristics are increasingly becoming an important subject in translating its incredible properties to the macroscale [4, 5]. In compositing graphene directly in a polymer matrix composite (PMC), the lack of favorable interfacial adhesion due to functionalization leads to low property improvement, hindering full adaptation [124]. Research has been done using traditional plastic processing techniques, combining chemically modified graphene within a polymer matrix [125]. This chemical modification allows for improved interfacial properties but maintains problems with chemical stability of surface modifiers; adding complexity and limiting applications for higher temperatures. By attaining a simplified process that functionalizes the interface without initial chemical modification, a new range of composites can be easily produced without road blocks. Our research shows that our method produces interfacial characteristics with chemical functionality. This provides an alternative in creating a simplified method of exfoliation leading to scalable chemical functionalization in-situ.

6.2 Revision of method to graphene functionalization

Functionalization of graphene species serves by modifying the interfacial structure through the creation of dangling bonds, introduction of an electrophile, or the development of noncovalent electrostatic bonds [65]. In this route, methods of graphene

functionalization are simplified by the creation of covalent and noncovalent bonds. On more traditionally made graphene, covalent bonds are formed usually at defect sites where the introduction of an oxide on surface defect is present; reacting with an electron donating or acceptor specials [126]. Noncovalent bonds are created by the interaction of chemical species interacting with π-bonds in the surface of graphene to create a stable functionalite. Based on the chemistry of the matrix and process, functionalization is probable. In our work, we show that our process is unique enough to create the occurrence of functionalized systems, based on the interfacial and morphological characteristics. Functionalization leads to improved interfacial bonding that directly transfers to improved structural applications [127] .

6.3 Method review

Natural flake graphite (Asbury Carbons, mills grade 3627 with 99.2 % purity, diameter = 250 μm, ρ = 2.26 g/cm3) was used as the exfoliating species. Polyamide 66 (PA66, Zytel 101 NC010, Tm = 262 °C, Tg = 60 °C, ρ = 1.14 g/cm3) was used as the high temperature polymer in this study. Prior to processing, both components were dried in an oven to eliminate water. PA66 was dried at 85 °C under vacuum, and graphite was dried at 350 °C for 4 hours.

PA66, 20 wt. %, and wt. 35 wt. % flake mineral graphite were mixed using a high shear batch mixer imparting elongational flow. The blends were mixed at 276 °C and a shear strain rate of 2876 s-1, under an Ar gas atmosphere to reduce polymer degradation. 35 wt. % graphite and in PA66 and PA66 were mixed for 10, 20, 30, and 45 min to produce G-PA66 samples and PA66 control samples at each mixing time Table 6-1,

PA66 and G-PA66 extrudate (approximate diameter of 2.94 mm) was prepared for subsequent characterization.

Table 6-1. Processing Matrix

Mixing Time (min)	Control Materials	Composite Materials
10	PA66	G-PA66
20	PA66	G-PA66
30	PA66	G-PA66
45	PA66	G-PA66

6.4 Morphological Analysis

6.4.1 . X-Ray Diffraction

In our assessment of the crystalline characteristics of the X-Ray diffraction results, the Scherrer Equation (1) was used to calculate the crystalline domain size of the phases in PA66, G-PA66, and Graphite. K = 0.9 represents the shape factor, λ is the radiation wavelength, β is the line broadening at half the maximum intensity of the detectable peak, and Θ is the Bragg angle in degrees.

$$L = \frac{K\lambda}{\beta cos\theta} \quad (1)$$

The starting graphite is analyzed to having a (002) lattice spacing of 0.334 nm, indicative of the stable hexagonal phase [121]. After exfoliated in the presence of elongational flow, the existing hexagonal phase shows an increase in (002) d-spacing, in Table 6-1. The results from the Figure 6-2 and Table 6-2 show a progressive reduction in the average domain size, leading to a 76% reduction in domain size for the graphite portion compared to its native structure. The increase in (002) lattice spacing suggests that the starting hexagonal phase is converting to a turbostratic phase of many layer graphene

contained in the composite. The turbostratic form of exfoliate has been known to contain stacks of graphene planes, which have undergone rotations and distortions [122]. Comparing samples G-PA66 30 minutes and G-PA66 45 minutes, there is a large difference in both the reduction in (002) domain size and the increase in lattice spacing. This suggests that after 30 minutes of mixing, a transition in the conversion of the graphene exfoliate and the resulting morphology has occurred. It is important to note that sizes smaller than the ~14 nm exist in the background curve data. Graphene, having a large FWHM, being highly oriented, as well as the process creating flakes with varying degrees of strain may attribute to the (002) upper limit domain size. It will be found that using other characterizations methods often used to study graphene result in identifying a plurality of few to many layer graphene sheets.

In Figure 6-2, a curve fit was constructed to establish a model for exfoliation by the reduction in (002) domain size in graphite. The exfoliation of graphite in PA66 is shown to fit a parabolic model, described as the mechanism for exfoliation. Parabolic models are closely tied to diffusion reaction systems [123] [124]. In the diffusion reaction system, the movement of species are modeled as a projecting wave front. In the creation of our graphene reinforced composite, the projecting wave behaves as the diffusing PA66 species between the graphite layers.

The results of the curve fit for the diffusion model shows that the linear equation is second-order with respect to mixing time. Second-order approximations accounts for a linear driving force (LDF) for diffusion a graphite intercalant, from Budzianowski [128]. In his work a second-order model a cyclic adsorption/desorption step change for fluid concentration at the surface was assumed. He found that the half-life for adsorption or

distortion was too long and provided no instance for full saturation, while diffusing. In our case, the PA66 diffuses, adsorbs, and then desorbs continuously. This process is successive until mixing stops, making it diffusion limited.

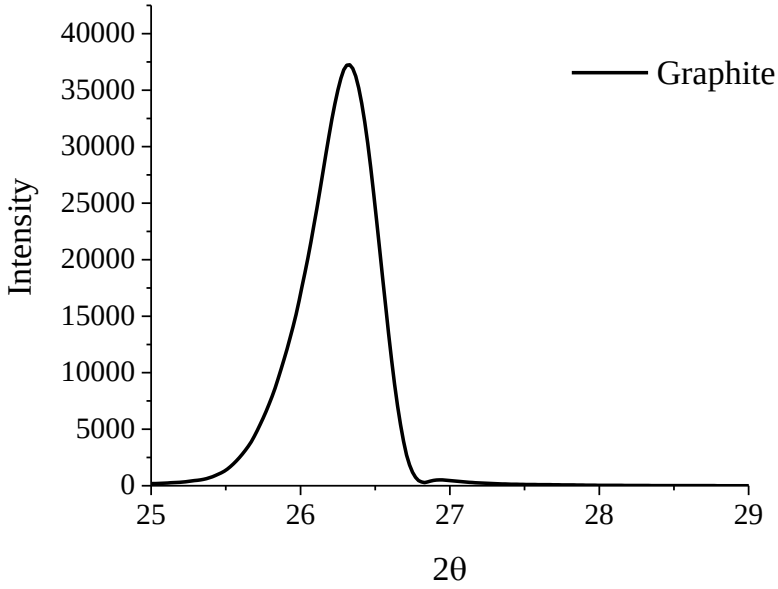

Figure 6-1 Diffraction pattern of (002) peak.

Diffraction patterns of PA66 exposed to extensional mixing are shown in Figure 6-3. In PA66, the first crystalline peak occurs at 20.7° 2Ɵ, which corresponds to the inter-chain hydrogen bonded (100) plane of the amide group for semi-crystalline PA66 [3]. The second crystalline peak for PA66 occurs at 23.6° 2Ɵ, corresponding to the overlapping diffraction peaks for the (010) and (110) planes, namely the key intra-chain and intersheet periodicities perpendicular to the (100) direction [129]. As mixing time was increased for PA66 samples to 30 minutes, lattice spacing of the (100) and (010)/ (110) diffraction peaks showed no trend, in Table 6-2. In the sample mixed for 45 minutes, there is a reduction in crystalline domain size. Suggesting extensive mixing times lead to a reduction in crystal domain sizes, likely due to

partial degradation or oxidation of uninvestigated species.

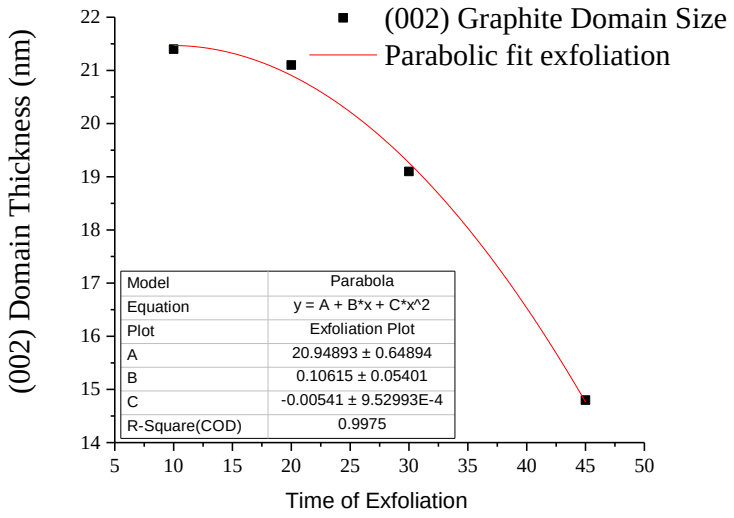

Figure 6-2 graphite (002) domain size curve fit

$$(002)\ \text{Domain (nm)} = 20.949 + 0.106\,t - 0.005\,t^2 \qquad (4)$$

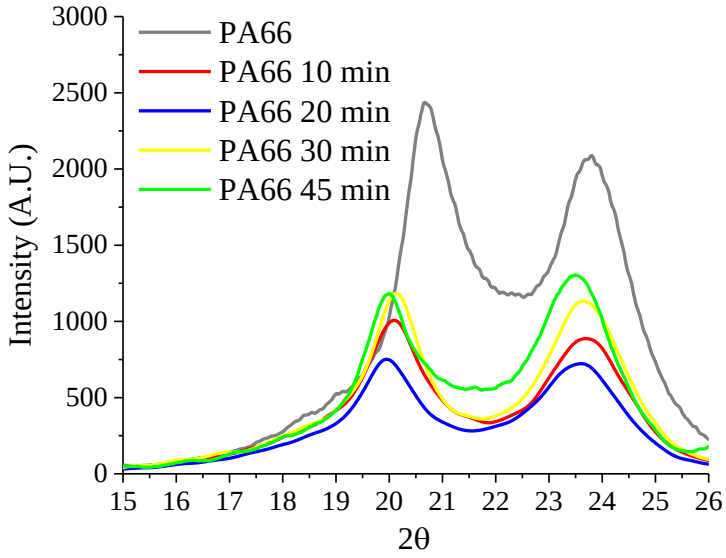

Figure 6-3 Diffraction patterns of PA66, PA66 10 min, PA66 20 min, PA66 30 min, and PA66 45 min showing the (100) & (010)/(110) diffraction peaks for PA66

XRD patterns of PA66, relative to the extensional mixing with graphite, appear in Figure 6-5. Relative to Figure 6-4, the PA66 diffraction peaks are found to contain close similarities to the graphite exfoliating PA66. After analyzing the diffraction peaks by fitting the resulting lattice and domains, crystal structure information is obtained, Table 6-2. During graphite exfoliation to 30 minutes, the crystalline domain of PA66 increases in the hydrogen bonded direction (100) and decreases in the van der Waals direction (010)/ (110). The change in domain size suggests a preferential crystallization direction in PA66, likely due to the extensional flow process. In Figure 6-6, anisotropy of the diffraction peak profiles in pure PA66 versus graphene reinforced PA66 reveals a non-linear dependence on exfoliation time. By the increasing mixing time to 30 minutes for G-PA66, the inter-sheet (010)/ (110) d-spacing increase, Table 6-2. The non-uniform changes in crystal domain size may allow for preferred crystallization along the surface of the nanoflake, and in the hydrogen bonded plane. This suggests preferred direction for PA66 in the (010)/ (110) directions and limited growth in the (100) direction.

Extending the time of mixing from 30 minutes to 45 minutes with graphite, produces a distinctive change in the G-PA66 lattice structure. G-PA66 shows a lattice increase for both the (100) and (010)/ (110) by +0.0030 nm and +0.0037 nm, respectively. This material also changes with a reduction in the hydrogen bonded (100) domain and an increase in the intersheet (010)/ (110) domain. The change in the van der Walls (010)/ (110) direction trends parallel to the lattice changes in graphite (002). The reduction in (100) d-spacing is likely due to disruptions in the hydrogen bonded network due to few layer graphene and many layer graphene lattice mismatches, that may increase available surfaces for binding [130].

It is likely that the lattice parameters in the hydrogen bond and the van der Waals direction follows not with the degree at which the graphene is reduced in size, but with the (002) lattice spacing between graphene layers beyond 30 minutes of mixing. The stacking faults in graphene exfoliate changes to the lattice parameters in PA66, which lead to parameter increase. These faults are the results of created turbostratic graphite [131], consisting of an increased and shifted lattice spacing.

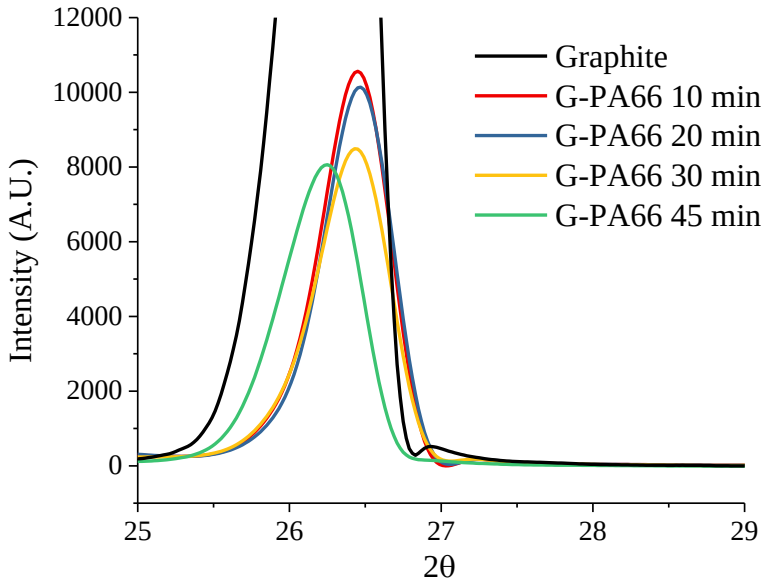

Figure 6-4 Diffraction pattern of graphite, G-PA66 10 min, G-PA66 20 min, G-PA66 30 min, and G-PA66 45 min of Graphite (002) peak – scaled for composite exfoliation

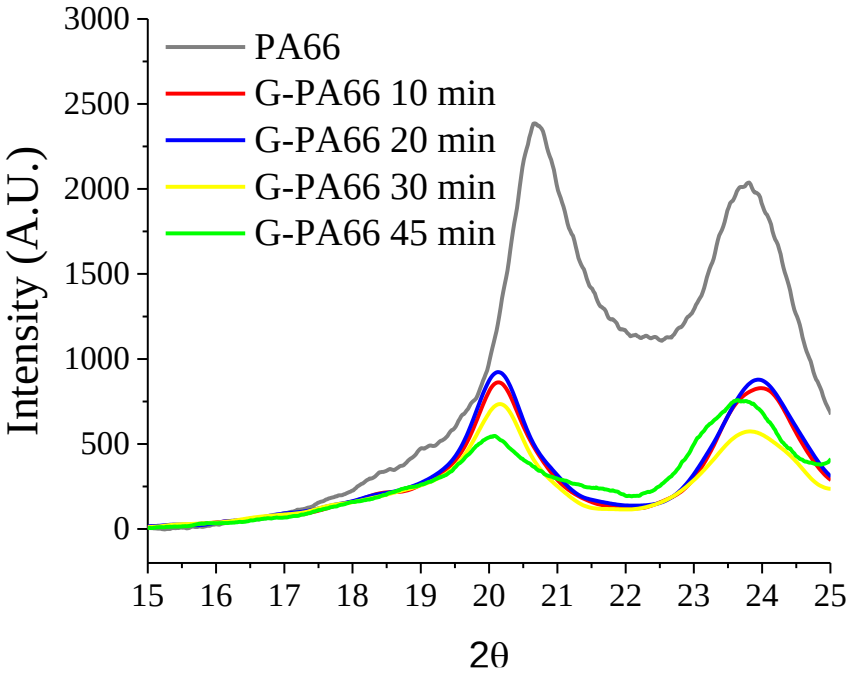

Figure 6-5 Diffraction Pattern of PA66, G-PA66 10 min, G-PA66 20 min, G-PA66 30 min, and , G-PA66 45 min showing the (100) & (010)/(110) diffraction peaks for PA66

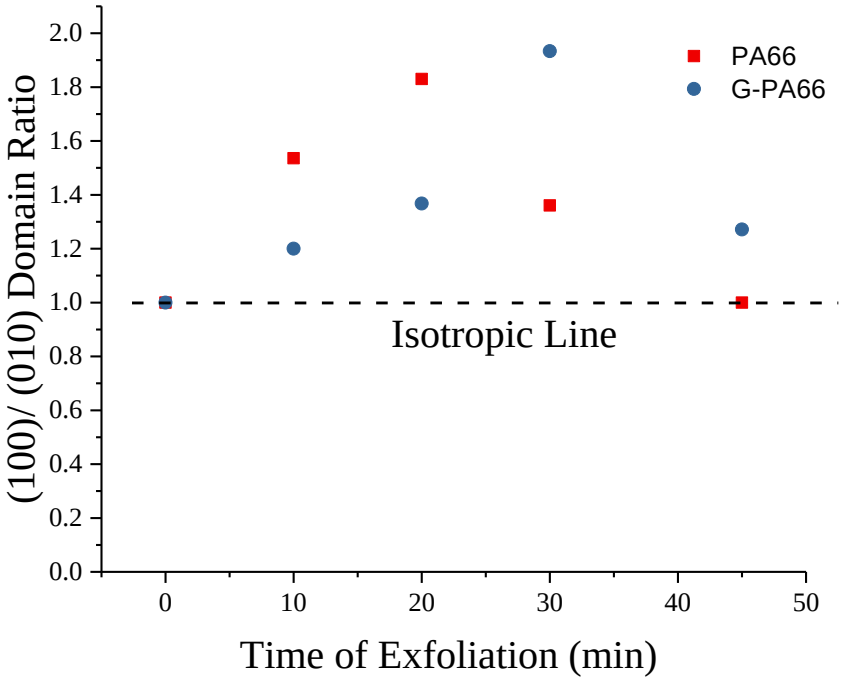

Figure 6-6 PA66 (100)/ (010) domain size isotropy parameter vs graphite concentration; (010) is (010)/(110)

Table 6-2 Diffraction data for Graphite, PA66, and G-PA66

Materials	Mixing time (min)	PA66 d (100) nm	PA66 (100) domain nm	PA66d (010)/ (110) nm	PA66 (010)/(110) domain nm	Graphite d (002) nm	Graphite (002) domain nm
Graphite	-	-	-	-	-	0.3344	62.7 (4.1)
PA66	-	0.4407	4.4 (0.2)	0.3878	4.4 (0.7)		
PA66	10	0.4427	8.6 (0.4)	0.3753	5.6 (0.2)	-	-
PA66	20	0.4453	9.7 (0.6)	0.3768	5.3 (0.2)	-	-
PA66	30	0.4414	8.3 (0.4)	0.3758	6.1 (0.2)	-	-
PA66	45	0.4435	2.9 (0.9)	0.3796	2.9 (0.5)		
G-PA66	10	0.4404	8.4 (0.4)	0.3719	7.0 (0.2)	0.3360	21.4 (0.3)
G-PA66	20	0.4405	9.3 (0.5)	0.3720	6.8 (0.1)	0.3358	21.1 (0.2)
G-PA66	30	0.4393	11.6 (0.8)	0.3735	6.0 (0.1)	0.3363	19.1 (0.2)
G-PA66	45	0.4423	8.9 (1.7)	0.3772	7.0 (0.3)	0.3386	14.8 (0.1)

6.4.2. Differential Scanning Calorimetry

Thermal properties for PA66 and G-PA66 after 10, 20, 30, and 45 minutes of elongational mixing appear in Table 6-2, with corresponding thermograms in Figures 6-7 - 6-10. Though difficult to notice in Figures 6-7 & 6-9 the glass transition temperatures for PA66 and G-PA66 were calculated using a baseline tangential method. A line representing the baseline was drawn from 0° C in the direction of increasing temperature. A deviation from the baseline, at an inflection point in the thermogram, was found to be the glass transition temperature (Tg). Transition temperatures for 10, 20, 30, and 45 minutes of exfoliation mixing of PA66 & 10, 20, 30, 45 minutes G-PA66 were found. The glass transitions (Tg) were found to occur at 60, 56, 57, 53, 56, 57, 51, 50 °C respectively. For all the values listed in Table 6-2. The bulk crystallinity of PA66 was calculated according to (3), for which enthalpy of melting for 100 % crystalline PA66 is $\Delta Hm^\circ = 197$ J/g [132]. The values for ΔHm were adjusted for percent PA66, since G-PA66 samples only have 65 wt. % PA66.

$$\text{Weight \% Crystallinity} = \frac{\Delta Hm}{\Delta Hm^{\circ}} \times 100 \quad (2)$$

In Figure 6-8 & 6-10, the reheat cycle is shown for PA66 samples, we see the formation of two distinct melting peaks in Figure 6-7. Two melting peaks are due to a bimodal distribution of crystallites formed by an intermediate heating and cooling rate of 10° C/min [133]. Since the rate chosen is constant, the thermal characteristics of the crystallites are dependent on the time of mixing and crystal structure formed. As the mixing time increases, the first melting peak reduces in intensity, and the secondary melting peak broadens. This broadening of the overall melting in PA66 is indicated by the reduction in onset melting temperature relative to Tm. As the mixing time increases, Tg, Tm, Tc, and ΔHc all decrease. However, there is no consistent trend with ΔHm results in Table 3 which produces a small increase in % crystallinity as mixing continues beyond 20 minutes.

In Figure 6-9, the reheat scans of the G-PA66 samples show a single melt peak; suggesting a narrow distribution of crystallites formed, compared to the bimodal curve in neat PA66. G-PA66 produces an increased crystallization temperature (Tc) and percent crystallinity for 10 and 20 minutes of mixing; symptomatic to heterogeneous nucleation of PA66 in few layer and many layer graphene presence. As the exfoliation time continues beyond 30 minutes, there a reduction in Tg, Tm, and Tc. These properties are much lower than all the other materials, suggesting a drastic change occurs at 30 minutes and beyond, in its structure.

Compared to pristine PA66 at 30 minutes, G-PA66 at the same exfoliating time, has nearly equivalent values of percent crystallinity, but has a much lower Tm and Tc. The reduced crystallization previously mentioned, suggests the suppression of crystallization

to occur. The exfoliated graphitic nanoflake in the matrix is likely to cause a subdued rate of crystallization [134] [135]. This suppression lead to a reduced crystallization temperature Tc of 9 °C. The same results appear for the Tg, with 45 minutes of exfoliation resulting to a 6 °C reduction than the lowest Tg. The crystallization suppression is shown sensitive to the percent crystallinity calculated, which suggest lower Tc depression leads to lower crystallinity.

Table 6-3 Differential scanning calorimetry results for PA66 and G-PA66

Material	Mixing Time (min)	Tg (°C)	Onset Tm (°C)	Tm (°C)	ΔHm (J/g)	Onset Tc (°C)	Tc (°C)	ΔHc (J/g)	Crystallinity %
PA66	10	60	246	261	72	235	233	70	~36
PA66	20	56	244	260	69	233	231	68	~35
PA66	30	57	243	259	71	233	231	66	~36
PA66	45	53	245	256	73	238	234	59	~37
G-PA66	10	56	241	252	97	243	239	85	~49
G-PA66	20	57	243	254	103	245	241	94	~52
G-PA66	30	51	226	239	69	229	222	74	~35
G-PA66	45	50	218	236	48	227	217	38	~24

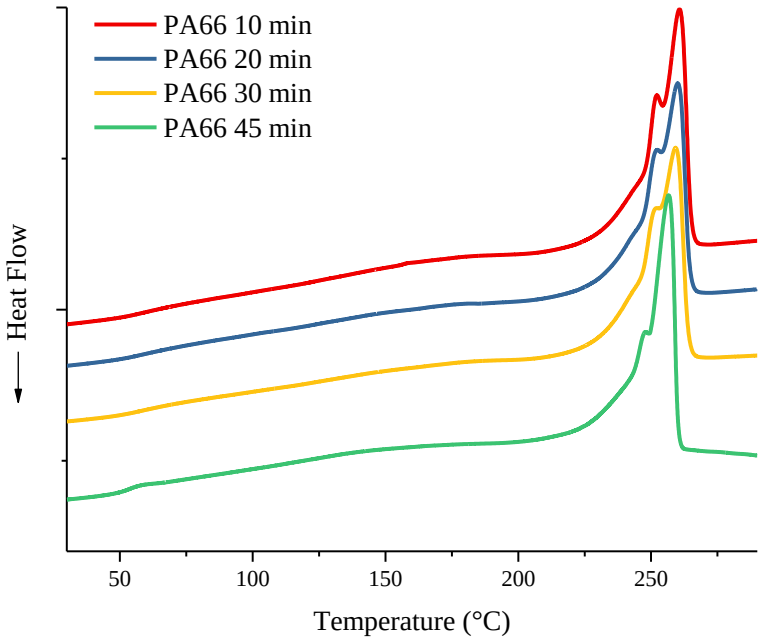

Figure 6-7 DSC thermograms for PA66 10 min, PA66 20 min, PA66 30 min, PA66 45 min melting

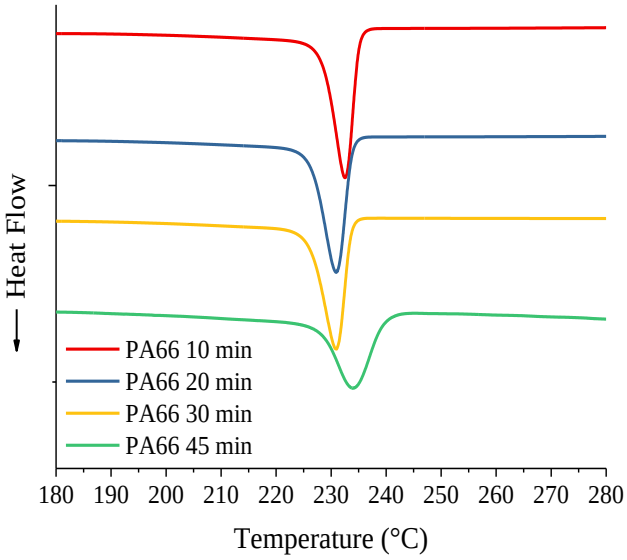

Figure 6-8 DSC thermograms for PA66 10 min, PA66 20 min, PA66 30 min, and PA66 45 min crystallization

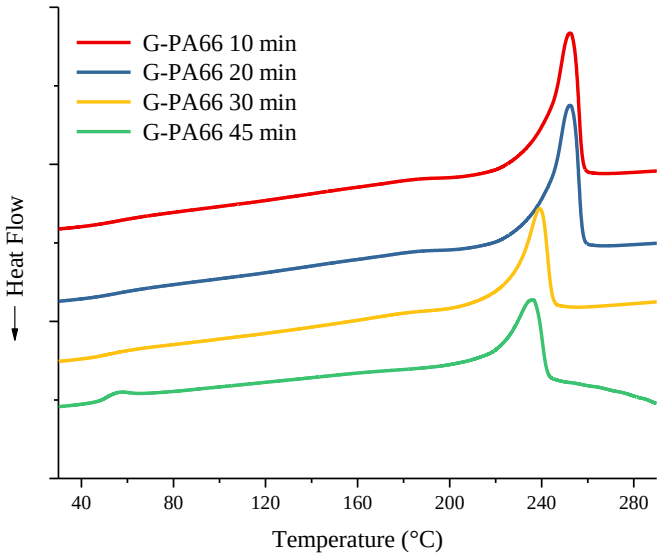

Figure 6-9 DSC thermograms for G-PA66 10 min, G-PA66 20 min, G-PA66 30 min, G-PA66 45 min melting

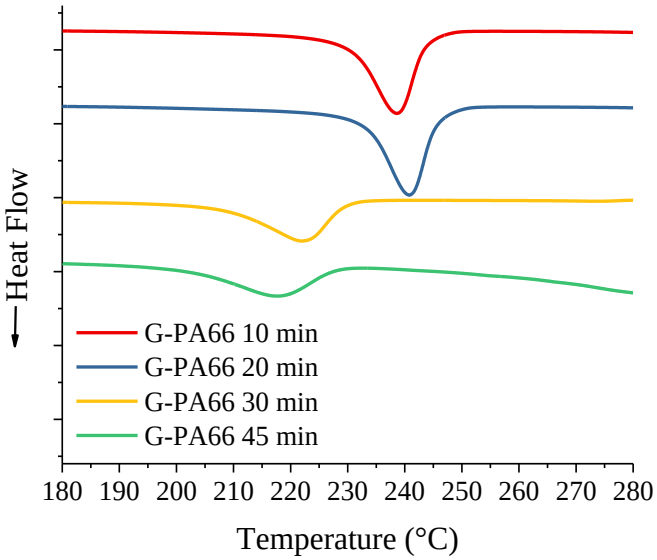

Figure 6-10 DSC thermograms for G-PA66 10 min, G-PA66 20 min, G-PA66 30 min, and G-PA66 45 min melting crystallization.

Identifying how the crystal structure relates to the thermal stability of G-PA66 composite, we see that the hydrogen bonded lattice parameters play an important role. This is not represented in the neat PA66, since the differences between 20 and 30 minutes are nominal. G-PA66 mixed at 20 minutes; having the least modified hydrogen bonded lattice, has relatively higher thermal properties and percent crystallinity. The thermal property variations occurring through reduction of the hydrogen bonded lattice, suggesting there is a relation to the structure in the PA66 of the composite. From the increased crystallization temperature Tc and percent crystallinity, we know this is evidence of surface crystallization occurring in the G-PMC (10 & 20 minutes). The cause of crystallization temperature depression in G-PA66 mixed at 30 minute might be explained by the exfoliated graphene acting as unstable crystals growth surfaces. These surfaces form disrupted hydrogen bonded sites; imparting themselves between the formed crystals, suppressing their crystallinity and thermal stability [136].

6.4.3. Field Emission Scanning Electron Microscopy

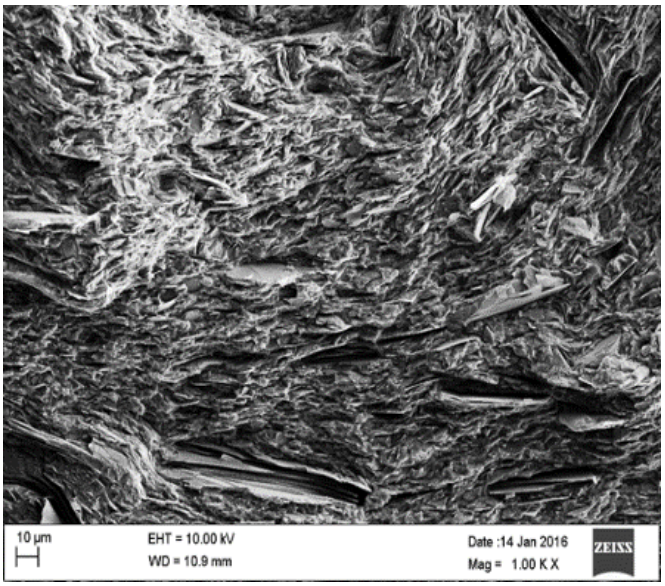

Figure 6-11 Surface of cryogenically fractured G-PA66 30 min Composite at low magnification

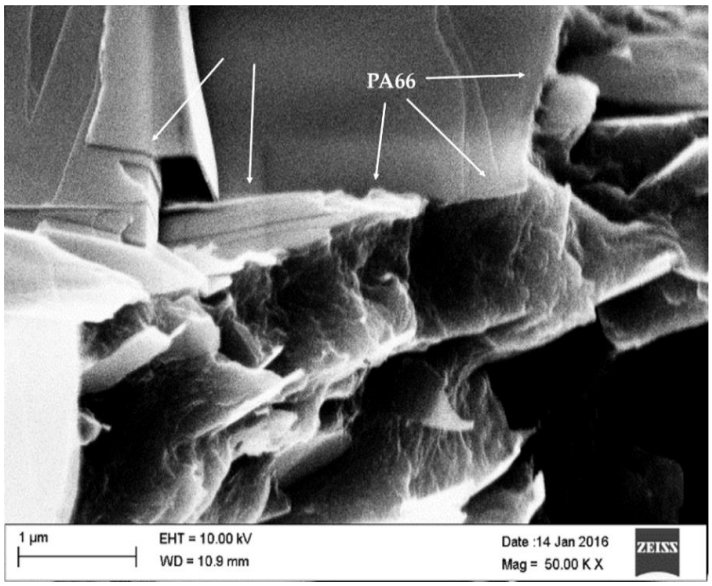

Figure 6-12 Graphitic edge overhanging polymer in G-PA66 30 min Composite

In all stages of the exfoliation process, it is important to note that there exist both few layer and many layer graphene flakes, even though the average graphite domain is calculated to be 14.8 nm. This is suggested, due to the fact that few to many layer graphene crystallites in the (002) direction are weakly diffracted. The weakly diffracted domains make the crystals unresolved from the background. That being said, the first thing to notice is the lack of large flakes of graphite present on the fractured surface. The lack of visibly large flakes suggest that nearly all the graphite were reduced in thickness, but retained relatively large surface area in Figures 6-11 & 6-12. The reduction in graphite flake thickness provides improved dispersion of few to many layer graphene sheets, making it difficult in locating the surfaces of the PA66 matrix. When cryogenically fracturing the extrudate in Figure 6-11, voids are left behind on the surface of the samples. These voids are holes left by the sliding of graphitic sheets not interacting with the matrix, as they are being pulled out from their center. The nature of the pullout structure left behind suggests some flakes are 'locked in'. It is also interesting to note that pulled out sections leave behind corrugated steps at the edges of exfoliate, seen in Figure 6-11.

When looking at Figure 6-12, a more detailed image is shown of the step morphology left by the process. Following along the steps in Figure 6-12 we notice what appears to be a rolled edge, with the direction of rolling applied to the left in the micrograph. The development of this rolled edge structure seen in the image, is presumably caused by frictional forces imposed by the matrix. The peeling leaves behind a nanosheet, which is shown to be ripped at the edge. If you follow the edge where the ripping occurs, you can see PA66 attached or adhered to its surface. This rolled structure with the edged attached

PA66 is an indication of matrix interactions with the nanoflake graphitic structure. The morphology provides clues to the mechanism of exfoliation in this process.

To observe the created graphene in the absence of the extrudate matrix, cryogenic milling was performed on the 30 minute G-PA66. In Figure 6-13, large area few and many layer graphene is shown having what looks like an elongated shape. Focusing on the edges of the newly created flakes, a jagged and then smooth structure is noticed. By following those edges on the right side of the micrograph, the rolled section appears smooth. Comparing this discovery to the previous Figures, this suggests that the other smooth sections are folded over sheets of many layer graphene, created by the frictional force of the molten polymer.

What is interesting in Figure 6-13, is the transparency of the large area flakes to the electron microscope. Folded sections, as previously mentioned, shows the presence of additional wrinkles and folding structures under the layered graphene sheets. The transparency suggests that graphene is being created, otherwise transmission would be extremely difficult for graphite flakes.

What is difficult to find, is a distinct indication of the PA66 with the graphene in Figure 6b. What we do find is that the transparent surfaces of the flake are littered with bright surface and edge features. What these features represent is still not fully known. We do know that given the analysis technique, Insulators/nonconductors in SEM cause charge buildup in their surface. In that this charge buildup presents itself as bright spots in produced micrographs [137]. PA66 is known to have such low conductivity, that it is an electrical insulator. The bright spots are likely to be edges containing PA66, PA66 alone, or a combination of both. Observing the micrographs, we see the pristine surfaces,

which stress the point that our novel exfoliation preserves the in-plane surface structure of graphene. A traditional chemical method of graphene creates surface defects, wrinkles, and holes; which never simply retain such pristine surfaces [138] [139].

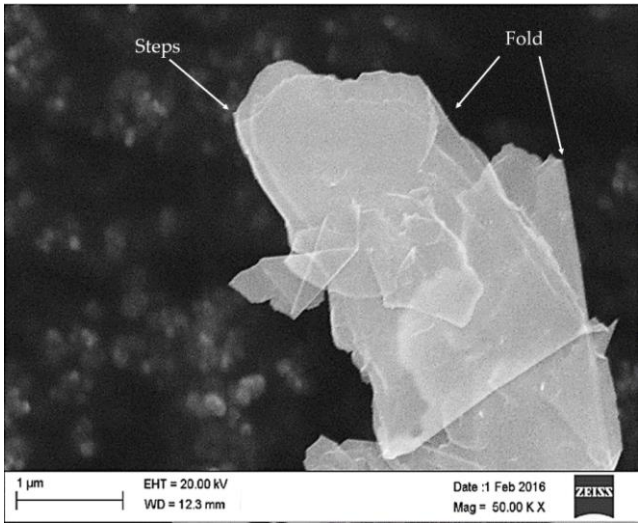

Figure 6-13 Cryogenically milled G-PA66 30 min showing transparency of exfoliated graphene flake, at high magnification

6.4.4.Transmission Electron Microscopy

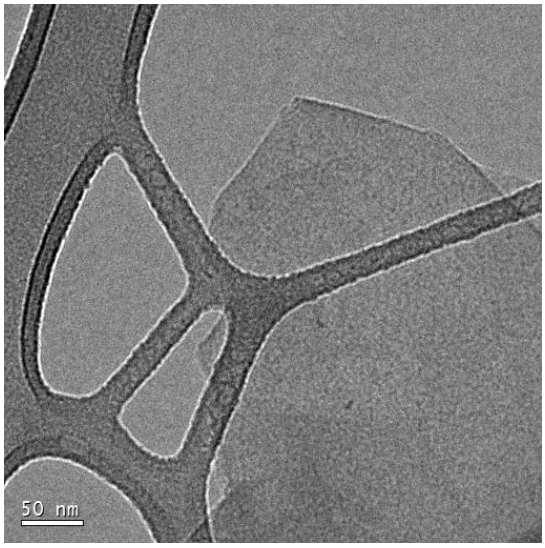

Figure 6-14 Low Magnification micrograph of isolated 30 minute G-PA66 flake on lacey carbon surface.

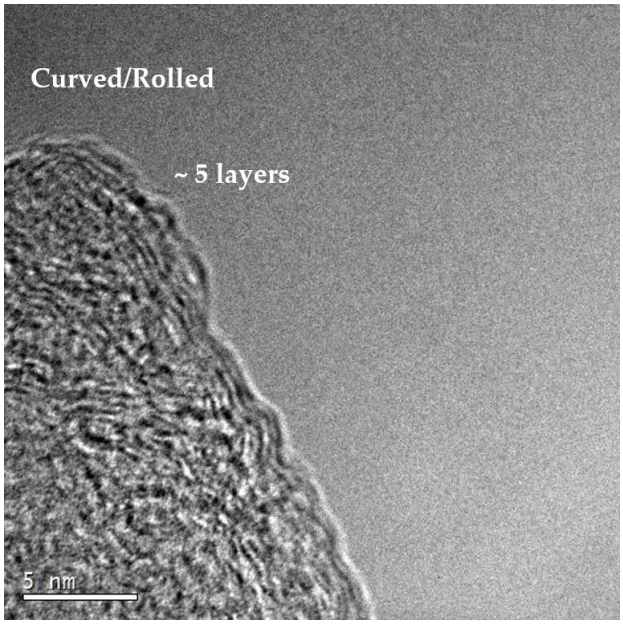

Figure 6-15 High magnification micrograph of rolled edge of many layer graphene.

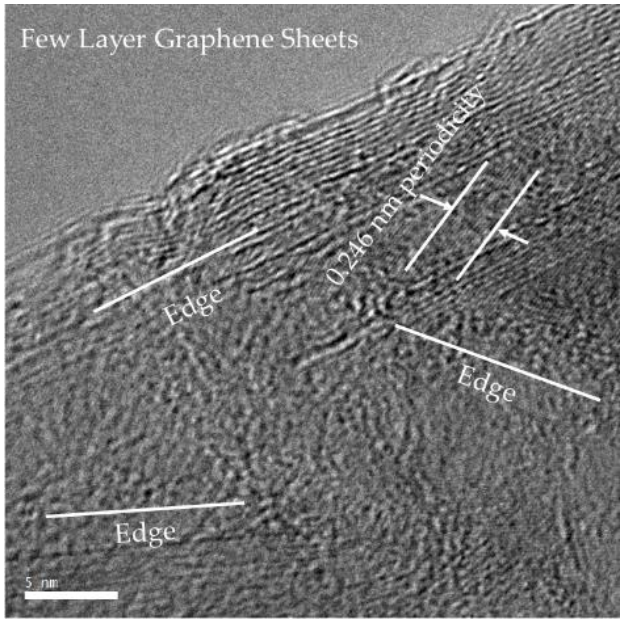

Figure 6-16 High magnification micrograph of edge containing many layer, and few layer graphene

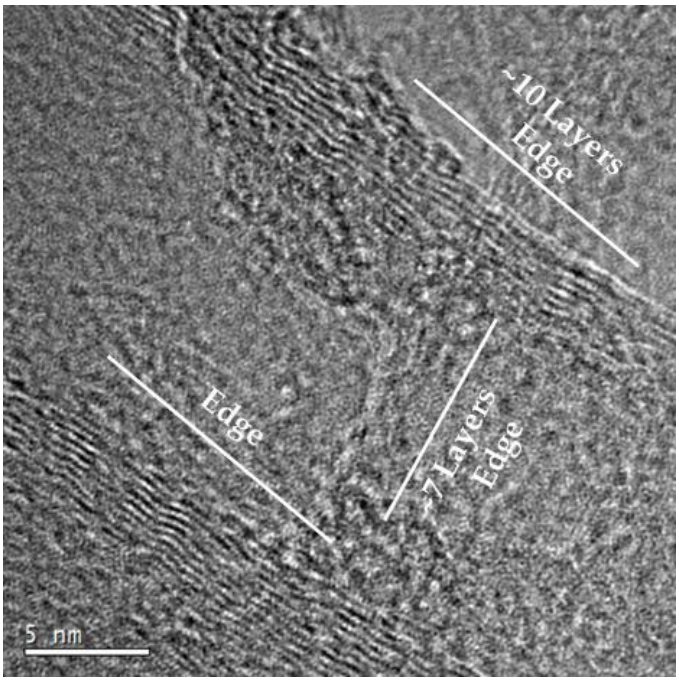

Figure 6-17 High magnification micrograph containing many layer Graphene

The first thing noticed from the HR-TEM analysis is that from the low magnification image, the process produces few and many layer graphene flakes of varying sizes Figure 6-14. Theses sizes consist of a combination of few layer graphene (2 – 5 layers), many layer graphene (≥ 5 layers), and the rest containing many layer graphene of varying sizes (< 50 nm in thickness) [140]. In Figure 6-15, 5 individual layers of graphene sheets are identified, while having the on the edge structure in focus. Following along the same Figure, the sheets are noted to folding upward; representative of a feature inherent to graphene, due to stresses at the edge [141]. Looking closer in Figure 6-16, a continuous structure is noticed on the steps of many layer graphene (the number of counted steps exceeds 10 layers), containing a smaller periodicity on the order of ~0.246 nm in size. 0.246 nm is known to be the lattice parameter of graphite, representing the distance

between carbon atoms along a single direction in the surface of a graphene flake. Given the size of the smaller periodicity, the surface structure is believed to be a 1 to 2 layer graphene sheet draped along the edge. This is an indication from the previous statement that many layer graphene to few layer graphene with a (002) smaller than 14.8 nm exist within the G-PA66 composite. This provides evidence that a multiscale layers of graphene exists within this composite.

Taking a step back and looking at the arrangement of the flakes, multiple many layer graphene size are shown to be orientated in multiple directions in Figure 6-16 & 6-17. These structural disruptions are indicative of turbostratic graphite; where the c-axis stacking sequence is either rotated or completely disrupted. These turbostratic layers are confirmed by the diffraction results; where they exhibit an increase in the c-axis spacing of the graphene layers. In this case, G-PA66 that was characterized, was mixed for 45 minutes; which suggests this to have a spacing of 0.3386 nm; having a 0.0042 nm lattice increase.

6.5 Interfacial analysis for functionalization

6.5.1 X-Ray Phototelectron Spectroscopy

In Figure 6-18 two distinct features occur in our process. The first in Figure 6-18a shows that as the shearing time increases, the binding energy (BE) is reduced. The second is that compared to PA66, G-PA66 has a higher BE in Figure 6-18b. The increased BE shift suggest that G-PA66 20 min produces an oxidized amide group, given by a BE increase of +0.5 eV to 399.8 eV [142]. As shearing increases, oxidation is reduced to 399.3 eV. This BE increase suggests that the graphene functionalized the polymer backbone to cause a shift in BE. Since this is done under an Ar gas blanket, the likelihood of oxygen

related contamination is low, so effects are significantly contributed by the created graphene. The progressive reduction suggests a destabilization of the newly formed functionalite, leading to early onset degradation. Degradation can be a function of trapped water 'unzipping' the PA66 or the delocalization by π bonds leading to depletion of weakly bound species.

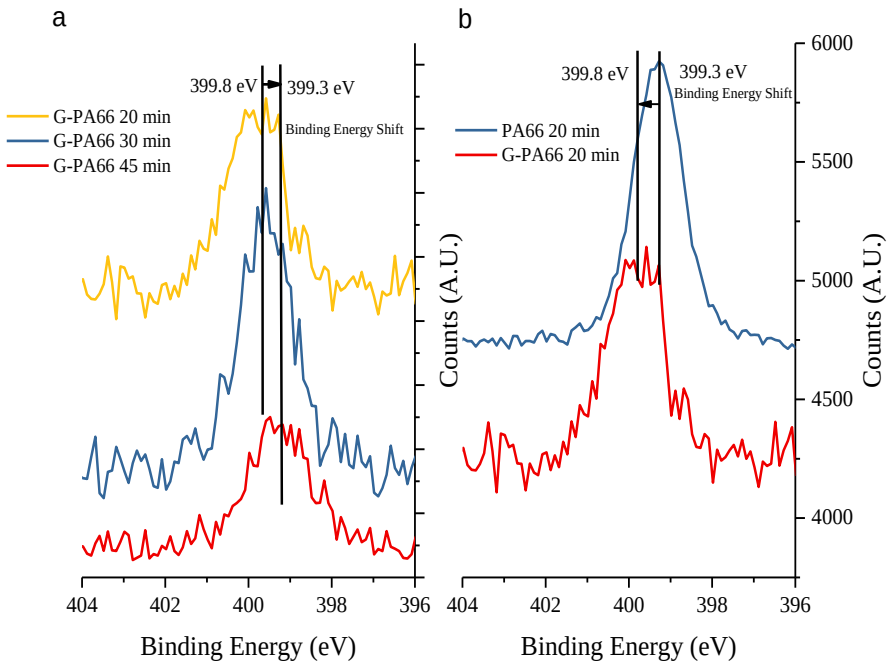

Figure 6-18 XPS Spectra of Nitrogen N1s for (a) G-PA66 sheared for (20, 30, 45 minutes) (b) G-PA66 and PA66 sheared for 20 minutes

6.5.2. Raman Spectroscopy

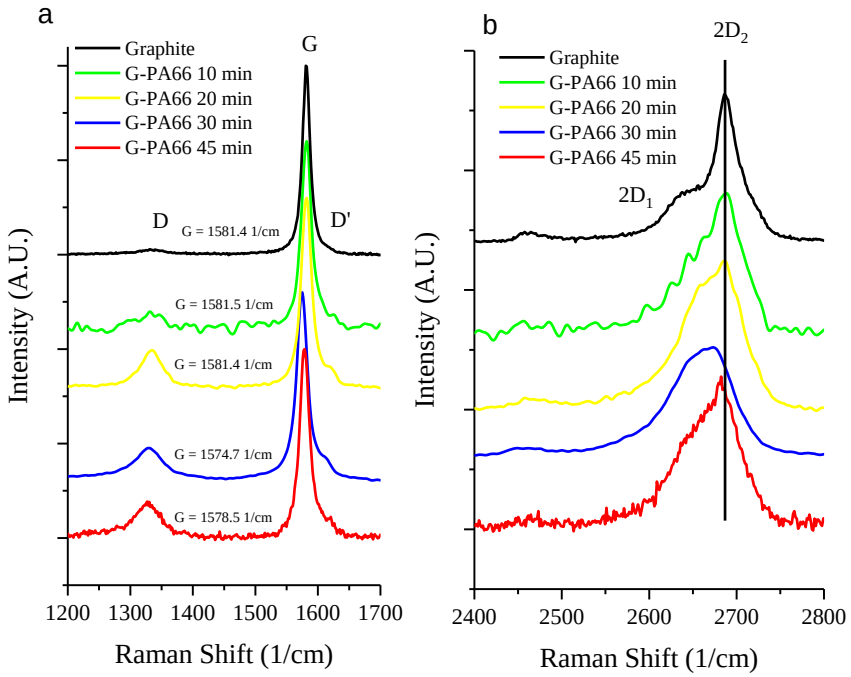

Figure 6-19 (a) Raman spectra of D, G, and D' of graphite, G-PA66 (10, 20, 30, and 45 minutes) (b) Raman spectra of 2D of graphite, G-PA66 (10, 20, 30, and 45 minutes)

In Figure 6-19a, an increase in intensity of the Raman D and D' forms, as the shear time increases. The Raman D band indicate scattering due to the sp^3 carbons on the surface of graphene [143], so an increase in intensity of the D peak relative to the G, suggests the edges are increasingly being functionalized [144]. The G-band in graphite is sensitive to strain and contamination effects in sp^2 carbon systems, and are used to investigate modification in the surface of graphene. In Figure 6-19a, a blue shift in G band occurs for G-PA66 30 and 45 minutes from the Raman signal. This suggests that beyond 20 min of shearing, the PA66 strongly disrupts the graphene surface, providing evidence for good interfacial adhesion of the PA66.

In Figure 6-19b peak intensities for 2D peaks show a significant blue shifts and peak broadening, which correspond to reduction in graphene thickness and a splitting of

phonon modes into $2D_1$ and $2D_2$. The increase and relative intensity of the $2D_1$ mode correlates to a reduction in flake thickess, similar to multilayer graphene spectra [145]. Longer exfoliation times present both peak broadening due to the development of $2D_1$, leading to an ultimate 2D peak shift.

6.5.3. Electron Microscopy for Interfacial Analysis

When looking at the surface of these flakes using HR-TEM Figures 6-20.a-c, three distinct interfacial morphological effects appear. The first in Figure 6-20a displays edge adhesion of PA66 on a preferential edge of graphene. This is displayed by observations of the rigid structure on the left of the same Figure. Graphene has two distinct edge structures; zig-zag and armchair. each of these structures maintain varying reactivity, where zig-zag being known for its reactivity. This makes a zig-zag edge more sensitive to functionalization by the creation of dangling bonds [146]. Edge selectivity is due to the appearance of pristine graphene layers 120° from that section. The second feature in Figure 6-20 is surface adhesion. On Figure 6-20b, we see surface “contaminants” , which appears as blotches on the micrograph. Polymers maintain a larger crystal structures than most inorganic materials. At this magnificaiton, PA66 appear as disordered. Which also is suggested by the shift in Raman G band. The third effect is turbostractic surface variants. When looking at a transparent section of an edge by diffraction, Figure 6-20d, we see the graphene hexagonal lattice structure has been rotated . Its believed this rotation is caused by the shear forces acting on the graphene shifting the interfacing sheets, during processing. Due to the rotation of the created graphene in Figure 6-20 b&c a structure on the order of 2.13 Å is observed on the surface. This structure is believed to be caused by the shift in $\pi - \pi$ bond distance (Figure 6-20e,) creating a pattern along the

surface. The appearance of the pattern in Figure 6-20c suggest we are observing the top layer of a transparent sheet of graphene that drapes the surface. This surface draping is undertaken by the curved over thickness along the edge in the Figure 6-20c.

.

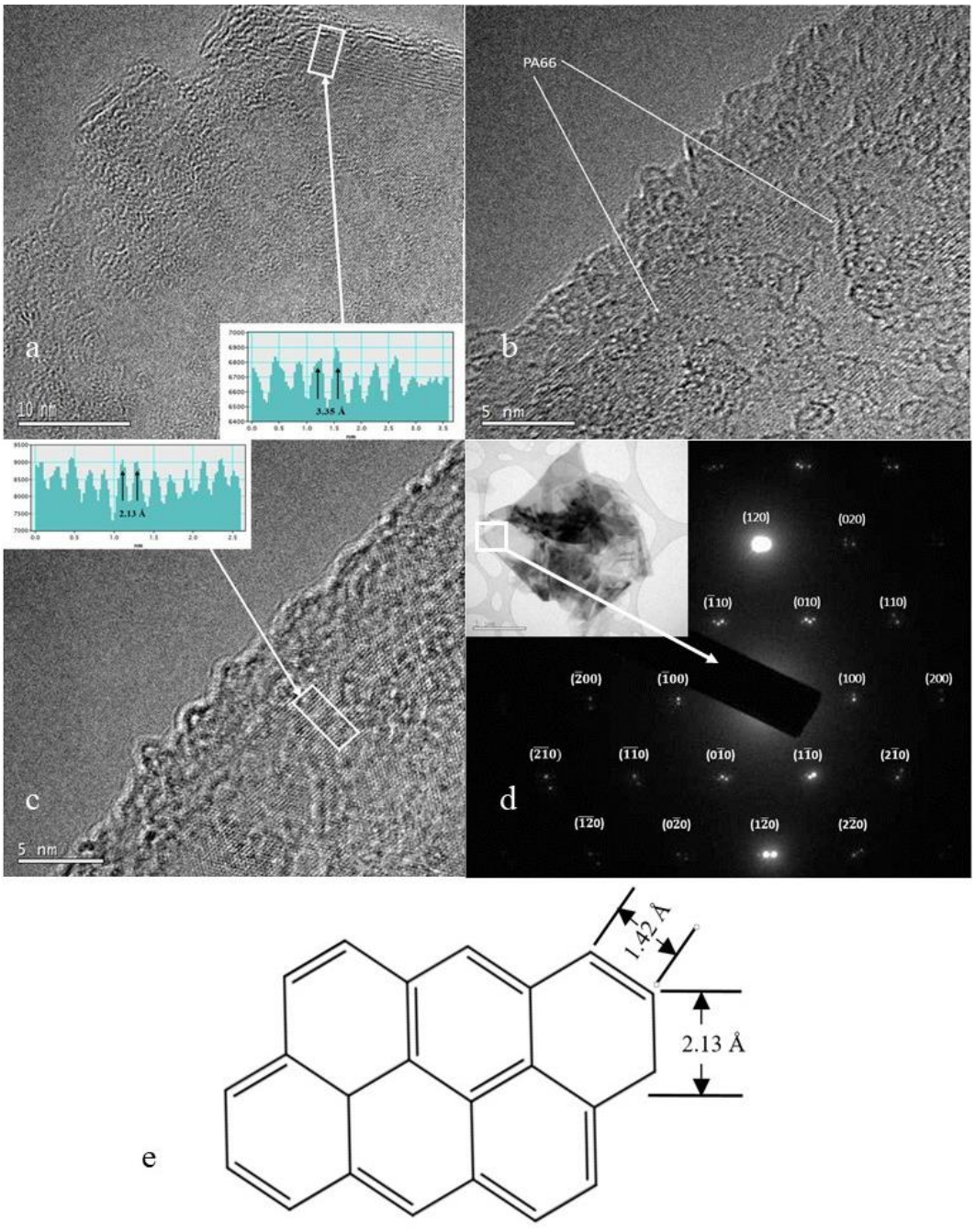

Figure 6-20 (a) Edge of Few layer graphene with 3.35Å graphene c-axis spacing (b) Surface of multilayer graphene with PA66 adhesion. (c) Surface of Graphene with 2.13 Å Carbon conjugated structure on surface (d) Diffraction of transmittable edge of observed area few layer graphene (e) Surface dimensions of graphene

6.6 Bulk Analysis Functionalization

Polyamides are materials of interest that have current use in consumer and automotive applications [147]. Inexpensive and simplified routes for property improvement can act as a huge advantage in new process development. Our method of exfoliation and functionalization has shown that an interaction exists between the matrix of PA66 and the reinforced graphene phase. In Figure 6-22, the G-PA66 shows that there is a ~400% increase in stiffness compared to the pristine PA66. Improvements in modulus (stiffness) act as a characteristic of enhanced interfacial properties between the phases [148] , confirming the result in our previous sections. An added benefit to the increased stiffness is the peak stress improvement by 6 MPa. Diffraction suggests that the orientation of domains correlate with improved stiffness, in addition to our systems having an improved toughness, in Figure 6-21. The toughness improvement is identified by the increase in area of the stress vs strain curve. PA66 without graphite has inherent toughness, however graphite addition aids in a stiffness improvement. In the area under the stress vs strain curve, results were found to be higher in 35 % graphite than 20 % graphite in PA66 (see appendix). In addition to the graphite concentration, it is suggested that this toughness increase was due to the reduction of the graphite and PA66 domains. Results of the curve show that smaller domains lead to an improved toughness. In regards

to the strain to failure, higher graphite concentration leads to a reduction. Graphite concentration increase leads to an increasing interfacial interaction between compositing constituents., creating higher strain energy density [113] [114]. Moreover, higher strain energy density creates highly elongated polymer chains, reducing available plastic deformation for a lower strain to failure.

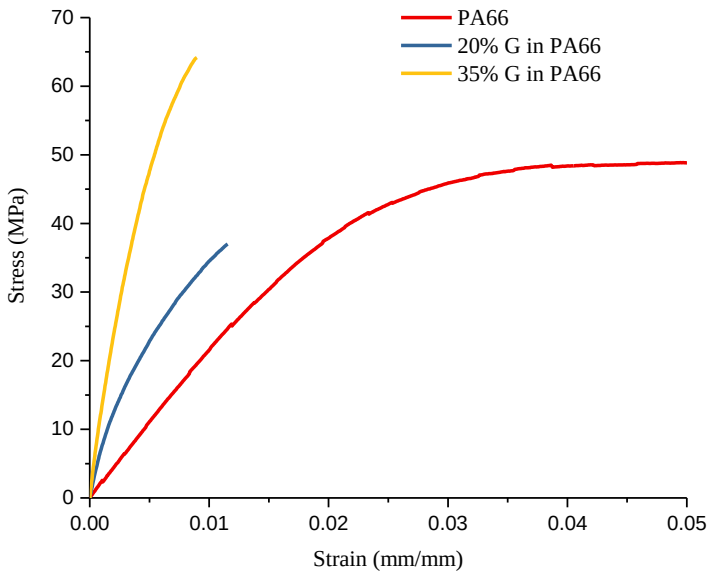

Figure **6-21** Stress vs Strain Curves for PA66 and G-PA66 Composites

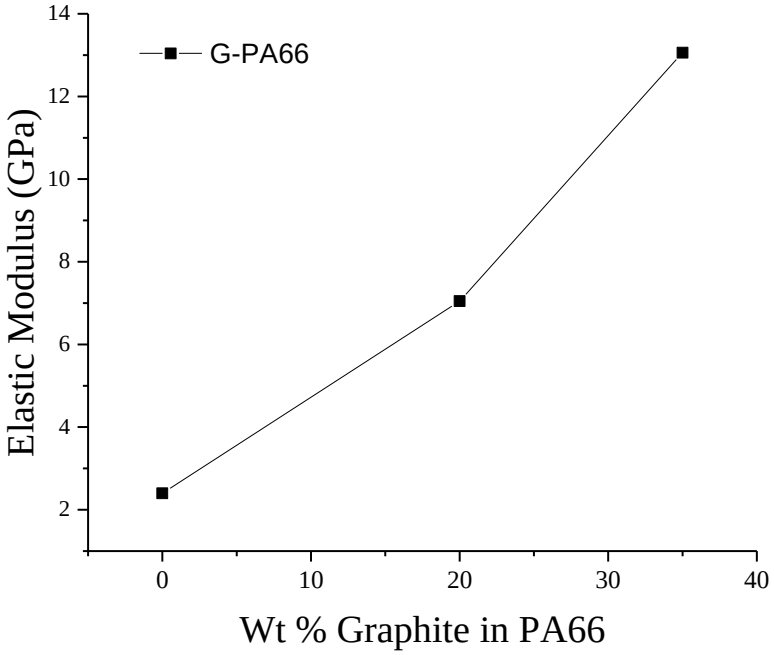

Figure 6-22 Elastic Modulus vs Graphite Concentration in G-PA66

Table 6-4 Mechanical Properties of PA66 and G-PA66

Materials	Wt % Graphite	Peak Strain (%)	Peak Stress	Modulus (GPa)
PA66 (20 min)	0	36.73	55.41	2.40
PA66 (20 min)	20	1.26	38.29	7.05
PA66 (20 min)	35	0.84	61.35	13.06

6.7. Closure

Exfoliating graphite in an elongational PA66 flow field, led to the production of a graphene reinforced polymer composite. From our novel process, multilayer graphene flakes were formed and functionalized continuously. Few to many layer graphene flakes were found, with the upper limit average containing a ~14 nm (002) domain size, by the x-ray diffraction results. High concentrations of graphene flakes smaller than 14 nm, in

the (002) direction, were found utilizing Raman and electron microscopy; leading us to believe that 14 nm represents an upper limit approximation for the crystalline domain size. This approximation is obtain by experimental conditions utilized in our diffraction experiment. Quantifying a higher concentration of graphene flakes would be best obtained using a combination of x-ray source (synchrotron), synthetically derived graphene of known size, or a combination of crystalline standards. Given that our starting materials is naturally derived graphite flake, obtaining the exact plurality of sizes would require a number of additional steps. Regardless, we believe that a high concentration of graphene flakes are captured in in the background due to their smaller crystalline domains and shear exfoliated condition.

Our G-PMCs show that the presence of these graphene flakes resulted in functionalization in G-PA66 by the oxidation of the nitrogen in the amide and the rehybridization of sp2 to sp3 C-C bonds in the graphene surface. The process found both the edge and surface results in bonding; where the zigzag edge plane appears more sensitive to erosion and adhesion to PA66. As the shearing time increased the oxidation of the nitrogen in the backbone was reduced, but the graphene edge and surface defects continued to be rehybridized by the Raman results. This suggests that the nature of functionalization changes by continued exfoliation and shear.

The exfoliation model suggests that having a high shear rate, drives exfoliation to be dominated by diffusion. This is understood by the time dependent diffusion parabolic model. Revisiting results from XRD, suggest that hydrogen bond disruption of PA66 (100) is sensitive to the properties formed. Crystal domains having a high aspect ratio in PA66 (100), have results that are more surface functionalized. Covalent functionalization

is prevalent in PA66 at the amide functional site. Therefore, improved covalent bonding at the amide group, suggests improved mechanical properties, due to improved stress transfer between the matrix and stiff, strong graphene platelets.

A method of graphite exfoliation and functionalization was done in a single batch process. Functionalization and size reduction was conducted without the addition of chemically modifying the graphite surface, producing toxic chemicals as by-products. This produced an environmentally friendly way of converting graphite to graphene in-situ. The ease in processes complexity by having a single step process allows for a lower initial cost to scale and aids in adaptation.

6.8 Appendix

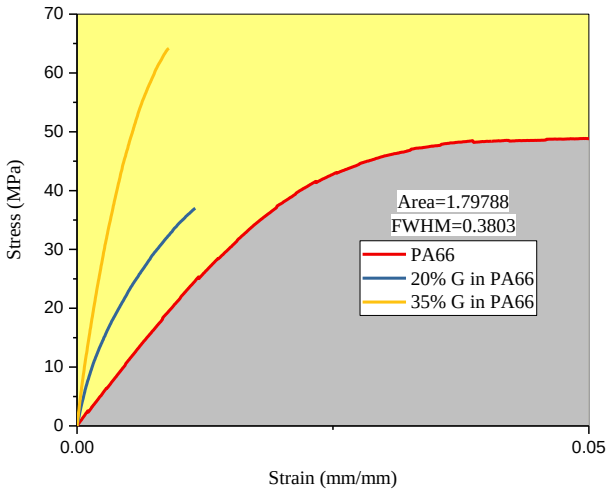
Stress (MPa)
Strain (mm/mm)
Area=1.79788
FWHM=0.3803
PA66
20% G in PA66
35% G in PA66

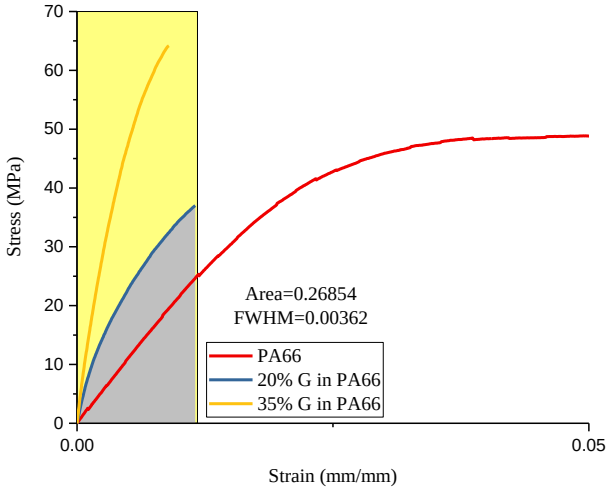
Stress (MPa)
Strain (mm/mm)
Area=0.26854
FWHM=0.00362
PA66
20% G in PA66
35% G in PA66

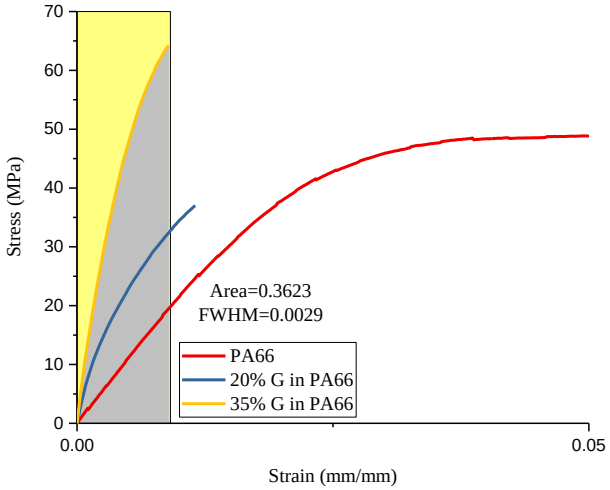
70
60
50
40
30
20
10
0
Stress (MPa)
0.00
0.05
Strain (mm/mm)
Area=0.3623
FWHM=0.0029
PA66
20% G in PA66
35% G in PA66

Chapter 7 Mechanochemical Structural Relationship of Extruded Graphene Reinforced Polysulfone Composite sheets

7.1 Summary

Polysulfone (PSU) is a high glass transition temperature polymer with properties uniquely suited for uses in harsh environments. The diphenylene sulfone group in the PSU backbone, gives the polymer inherent thermal stability, oxidation resistance, and antifouling properties. Graphene, having both exceptional mechanical and conductive properties, behave as a superior reinforcing agent for many emerging polymer composites [149]. The relationship between the mechanical, chemical, and morphological properties attained in a graphene-polymer composites is still not fully understood. However, by attaining a high degree of dispersion and increased interfacial contact by secondary bonds, performance enhancements can be achieved. An investigation of the mechanical-chemical-morphological properties was accomplished by using XRD, DSC, FESEM, Tensile testing, and XPS. PSU and graphite contained PSU was mixed using traditional shear extrusion and a novel high speed extensional flow mixer. The mixtures were extruded into 6" plastic sheets and characterized for property enhancement. The results show a link in the degree of exfoliation to improved adhesion of the PSU in the graphite. The mechanics of adhesion are attributed to the alignment of the polymer, creating soft epitaxy (secondary bonding) on the exfoliated edges. This adds to noncovalent adhesion, leading to improved mechanical properties.

7.2 Structural review of extruded sheets

Polymer sheets are applied in packaging applications, due to light weight and a strong surface barrier. In our work, PSU was a polymer chosen of interest for use as a plastic sheet. Research of this material has been applied in the applications for strain sensors [150] and extensive use as a separation membrane [151-153]. The polymer has the distinctive feature of having a diphenylene sulfone group in its backbone. These groups have a highly oxidized sulfur which draws electrons from the adjacent benzene ring; imparting oxidative resistance [154]. This property makes PSU a thermally resilient polymer.

Compositing graphene with a polymer like PSU provides the opportunity of enhancing a material with inherently superior properties. However, in order to improve upon this polymer, the mechanical-chemical relationship of this proposed composite must be understood. Using graphite as a precursor in PSU, our process creates graphene in-situ. Relating the leaps taken with our process by Nosker [42] in traditional extrusion, a property advancement can be accomplished. Testing the characteristics of extruded graphene reinforced PSU, this mechanochemical relationship can be used to understand future composite sheets and films with graphene enhancements.

Polymer sheets are the simplest shape any plastic product can be formed into. According to ASTM D883 [155], sheets cover thicknesses below 1 mm (1000 μm), but become film once those thicknesses reduce further to 0.25mm (250 μm) [156] . In sheet extrusion, molten polymer is conveyed, then extruded through a sheet or ribbon die. The die forms the width and starting thickness of the sheet. As the molten sheet exits the extruder, it contacts a roller or continue to be thermal formed through extension. Sheet extrusion is a process of interest due to its ease of use, process scalability, and the

simplicity of shapes generated [157]. By keeping in line with process adaptation, instituting modifications to currently processing steps help to establish the applications of a new engineering material.

7.3 Experimental Methodology

Extruded sheets of graphite filled polysulfone and pure polysulfone were produced using 2 processing methods. The first method utilized standard shear extrusion with a 6” sheet die attachment. Films were produced continuously as 100% PSU and 20 % graphite by weight in PSU, Figure 7-1. The second method required the same concentrations to be first exfoliated in a high speed extensional flow mixer (HS) then extruded into 6” sheets by the first method, Figure 7-2. The extruded sheets were tested to understand the mechanochemical relationship improved by using an extensional flow step.

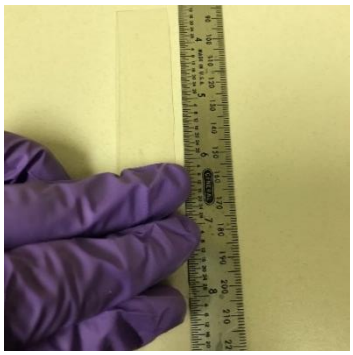

Figure 7-1 Polysulfone extruded sheet BB

Figure 7-2 Graphene in Polysulfone Extruded Sheet HS + BB

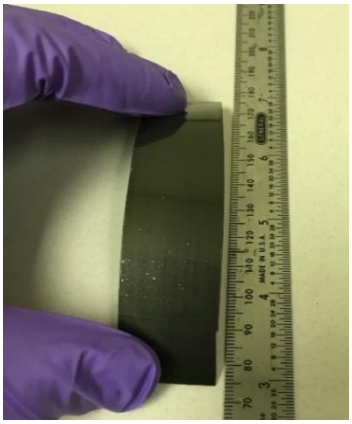

Figure 7-3 Polysulfone Extruded Sheet HS + BB

7.4 Morphological analysis of composite sheets

7.4.1 X-Ray Diffraction (XRD) of Extruded Sheets

Graphite has a natural slip direction, where the planar sheets slide past each other due to the application of shear. Traditional plastic extruders dominated by shear flow have been shown to exfoliate graphite inefficiently [158] [159] . The use of high speed extensional flow demonstrated by Nosker [42], effectively exfoliates graphite, as well as elongates the polymer in-situ. Therefore, using x-ray diffraction, the degree to exfoliation compared to traditional shear flow is identified.

The average domain thickness is identified by analyzing peak intensities in Figure 7-4. By utilizing the Scherrer equation in previous chapters, the FWHM was used to calculate the average (002) crystalline domain of graphite's diffraction pattern. Melt processing is shown to reduce the domain thickness of graphite from the peak intensity in Table 7-1. In a single pass with a traditional plastic extruder, the starting graphite (002) domain size is reduced by 35 %. With two additional passes, the average domain size is reduced by 4 nm. If the process of crystalline domain size reduction had a linear dependence then each pass would reduce the domain by 2 nm. In order to acquire the crystalline domain size for graphene at 3 nm, 23 passes would be required by the extruder. Negating the deficiencies to exfoliation of traditional extruders would be possible, but unrealistic.

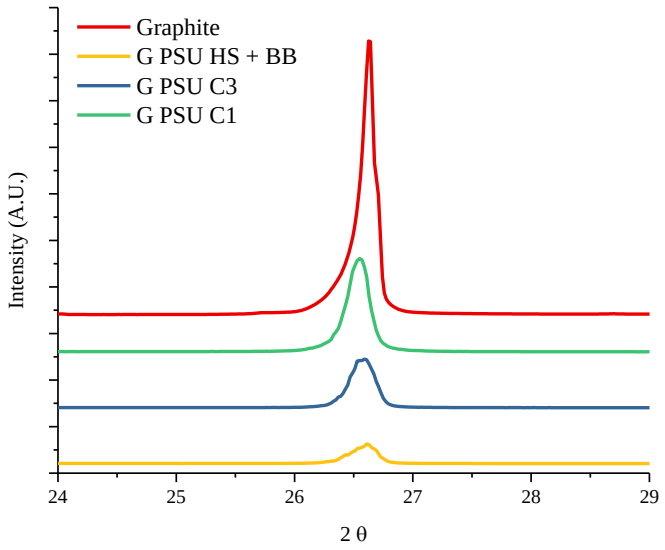

Figure 7-4 X-Ray diffraction patterns of graphite (002) crystalline plane

Table 7-1 Diffraction Results for Graphite in PSU

Materials	2Θ	d(Å)	FWHM (° 2 Θ)	Crystallinity (nm)
Graphite	26.494	3.36	0.135	69
G PSU C1	26.642	3.34	0.208	45
G PSU C3	26.648	3.35	0.229	41
G PSU HS + BB	26.539	3.36	0.249	37

For the sheet extrusion process containing an extensional flow step (G-PSU HS + BB), the size of the (002) domain is reduced by 44 %. The additional processing step has been shown in work by Nosker to efficiently exfoliate graphite to graphene, therefore issues encountered by traditional extruders are not present in this step. Specifically, in the extensional flow processing step (HS), 10 minutes of exfoliation time was used to account for the time dependence to scale a continuous process. For an exfoliation time of 10 minutes, domain size reduction occurs by reducing the number of processing steps. Longer mixing times equates to high exfoliation.

The overall takeaway of the diffraction results is that the process containing the extensional flow step reduces the domain size of the graphite (002) plane with the fewest number of passes. The effectiveness of domain size reduction can be seen by the comparative results in Figure 7-5. Relating these characteristics to the mechano-chemical relationship, we are reminded that in-situ production of an even smaller nanophase is undertaken. The reduction in domain size of graphite results in the increase in surface area and surface interface. Therefore, smaller domains lead to greater interaction. It is also important to note as suggested in other chapters that graphene flakes much smaller than the calculated diffraction domain size exist within the matrix. Due to the characteristics of the x-ray source and experimental setup, detection limits are likely obtained for smaller domain. This is understood by the identification of few to many

layer graphene flakes in previous chapters, by TEM, Raman spectroscopy, and SEM. Since graphene often is extremely small with small domain sizes in (002) direction, concentrations of few to many layer graphene is often not captured by diffraction alone.

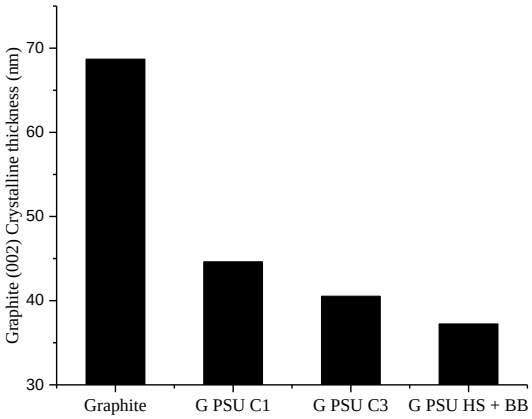

Figure 7-5 Graphite (002) Crystalline Domain Thickness

7.4.2 Differential Scanning Calorimetry (DSC) of Extrudate Sheets

A kinetic study used to determine the activation energy for the glass transition is beneficial in understanding the thermal stability of the extruded sheets. For these materials, the activation energy represents the energy barrier for molecular motion to occur. In chapter 6, we have shown that this energy barrier is sensitive to polymer elongation, which has polymer-polymer chain interactions. By the addition of exfoliating the graphite in-situ, an elongated polymer with exfoliated material, would be expected to cause an additional change in the activation energy.

Table 7-2 Calorimetry result of extruded composite sheets with increasing heating rates

Material	Q	T_g (K)	ln (Q/T_g^2)	$10^3/Tg$
PSU	10	459.24	-9.957	2.177
	20	459.80	-9.266	2.174
	30	460.69	-8.864	2.170
G-PSU C1	10	459.05	-9.956	2.178
	20	460.80	-9.270	2.170
	30	461.32	-8.867	2.167
G-PSU C3	10	459.15	-9.956	2.177
	20	460.96	-9.271	2.169
	30	460.61	-8.864	2.171
PSU HS + BB	10	454.13	-9.934	2.202
	20	453.61	-9.239	2.204
	30	453.55	-8.833	2.204
G-PSU HS + BB	10	457.38	-9.948	2.186
	20	455.69	-9.248	2.194
	30	451.29	-8.823	2.215

Using the results in Table 7-2 and Kissinger equation (1), the activation energy (E_a) for glass transition is obtained [160]. Using the heating rate Q at the equilibrium temperature of transition T, the data in Table 7-2 is plotted. The results are overlaid with a linear fit in Figures 7-6 &7-7, where a linear equation is acquired. The slope of the linear equation, being a rendition of (1), equates to a value of the activation energy divided by R (R = gas constant, 8.314 J/mol). By multiplying these results with the gas constant, the values for activation energy (E_a) are received.

$$\frac{d(\ln\left(\frac{Q}{T_g^2}\right))}{d(\frac{1000}{T_g})} = -\frac{E_a}{R} \quad (1)$$

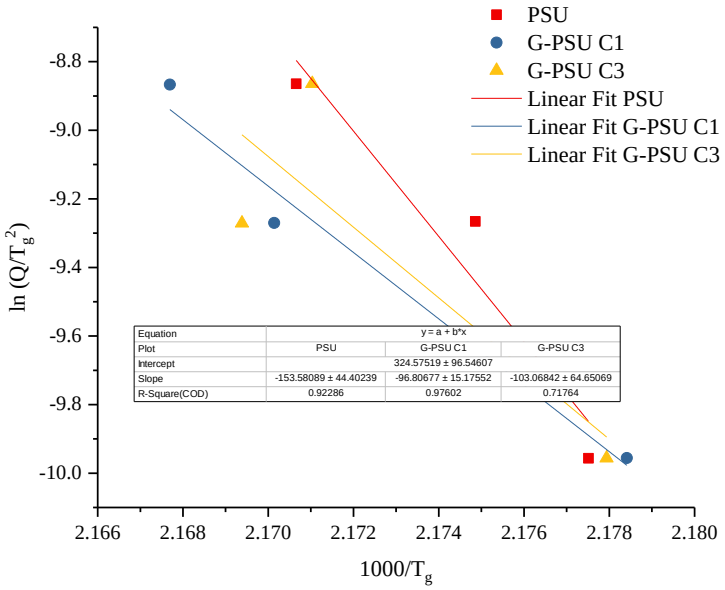

Figure 7-6 Linear fit for activation energy for PSU, G-PSU C1, and G-PSU C3 using the kissinger method

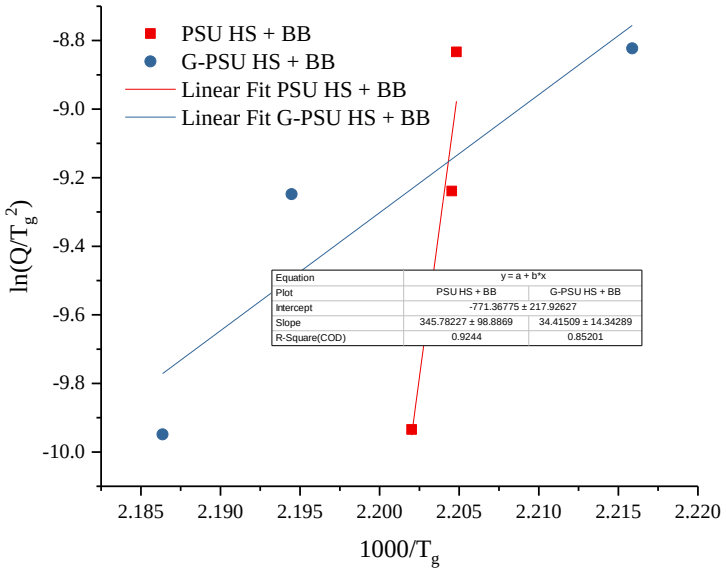

Figure 7-7 Linear fit for activation energy for PSU HS + BB and G-PSU HS + BB using the Kissinger method

Table 7-3 Activation energy for glass transition of PSU (kJ/mol)

Materials	**E_a of Tg for PSU (x 10^{-1})**
PSU	127 (37)
G-PSU C1	80 (13)
G-PSU C3	86 (54)
PSU HS + BB	-287 (82)
G-PSU HS + BB	-29 (12)

From the results in Table 7-3, the addition of graphite in the PSU matrix reduces the activation energy for molecular motion. As the number of passes through the extruder is increased, so does the activation energy. The initial reduction in activation energy, due to the addition of graphite, shows a catalytic effect by reducing the energy barrier to molecular motion. A reason for this is inherent in the deficiencies of traditional extruders. Graphite is a good conductor of heat energy. Thick graphite flakes can easily thermally conduct, due to their bulky size and ability to be interconnected by their large volume. I believe that in a single pass, heat is more easily distributed thought the volume, which reduces the activation barrier. This suggests that as the number of passes increases, re-aggregation occurs. The re-aggregation process is likely driven by inefficient distributive mixing, causing the segregation of graphite and polymer into islands. These segregated islands would lack proper heat distribution, lessening the catalytic effect provided by the graphite.

For the extruded sheets containing an extensional flow step (HS), the activation energy is found to be negative in Table 3. This is fundamentally different than the positive potential energy barrier in the traditional plastic extruder sheets. A negative

activation energy is found when low-energy reactants react faster than high-energy reactants [161]. Although both reactions are occurring, the overall kinetics displays an average negative activation energy. The change in the sign of the activation energy suggest that a stable intermediate phase (I*) is present in (2). The intermediate phase is competing with the rate of decomposition (k_{-1}) against glass transition (k_2). The occurrence of decomposition is proposed by the discoloration of the sheet in Figure 7-3, which includes an extensional flow step. Due to the rate dependence of the activation energy and the average kinetics of the process (k_1, k_{-1}, & k_2) [162] , the overall activation energy is negative (E_a). This all suggests that the PSU HS + BB sheet is decomposing.

$$A \underset{k_{-1}}{\overset{k_1}{\rightleftharpoons}} I^* \xrightarrow{k_2} P \tag{2}$$

In G-PSU HS + BB the negative activation energy has a much smaller energy potential as compared to PSU HS + BB. The sign of the energy potential suggest decomposition is occurring, but the addition of graphite lessens the effects. The reduction in activation potential is dependent on the distribution of exfoliated graphene due to the extensional flow process. The process is able to distribute and reduce the size of graphite, creating an interconnected network of conductive surfaces. This network distributes heat-energy throughout the sheets, but also maintains an intimate contact with the matrix. Activation energy reduction is a catalytic effect that results in efficient energy transfer between PSU and graphite by an increased thermal conductivity in the extruded sheet.

Generally, efficient energy transfer is due to the high surface area exfoliate created and secondary interactions likened to functionalization.

Investigation of the activation energy for extruded composite sheets, suggests that materials containing an extensional flow step may produce uniform exfoliated graphite and many layer graphene. The exfoliated filler has a catalytic effect in reducing the energy potential for glass transition and depressing the rate to degradation. This suggests that the changing kinetics is likened to functionalization of the polymer to the graphitic surface. Although degradation is occurring, it is not important in understanding the benefits of the composite sheets. As degradation appears to be inherent in the extensional flow process, the addition of graphite lessens its effect.

7.4.3 FESEM of G-PSU Composites

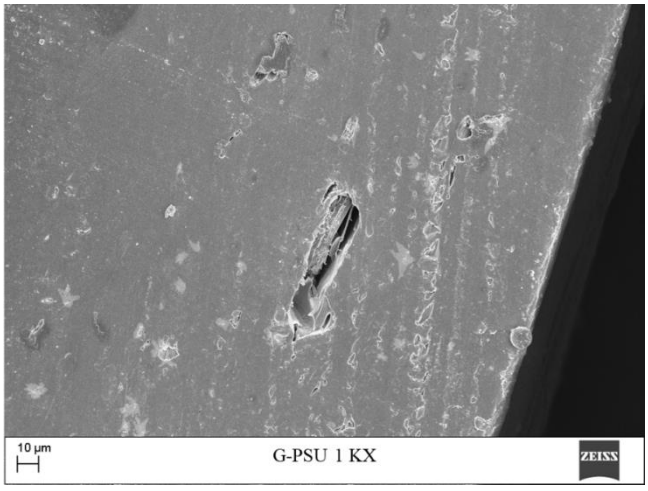

Figure 7-8 SEM micrograph of extruded films of G-PSU HS + BB at 1 KX

In Figure 7-8, the low magnification image shows a smearing of the composite surface due to the cleaving process. A void, left by many layer graphene pullout, is analyzed to identify the interfacial microstructure. When the magnification is increased in

Figure 7-9, graphite sheets are observed with their planes arranged perpendicular to the surface. The graphite in the surface appears to be aligned in the same direction, suggesting orientation imparted by the process. Between the layers of graphite sheets, individual planar slip is seen protruding from the surface. The slip planes in the surface suggest a mechanism of intercalation of the polymer between the graphite flakes, causing size reduction. Diffusion intercalation has been stated as mechanism in chapters 5 & 7 chapter leading to be a consistent theme in extensional exfoliation. A closer look at the edge of the graphite shows a surface texture of polymer. Edge texturing is a method of functionalization but it is unclear whether this is driven by covalent or noncovalent bonding. If this is due to noncovalent bonding, then adhesion is likely driven by soft epitaxy [149, 163] of the polymer within the slipped edges of the graphite.

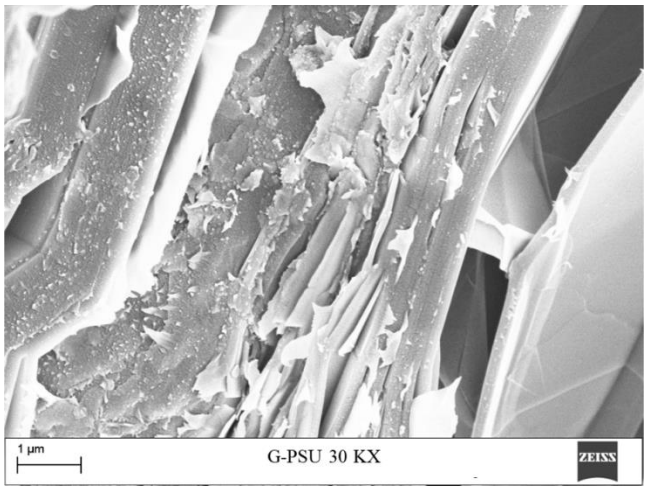

Figure 7-9 SEM micrograph of extruded films of G-PSU HS + BB at 30 KX

7.5 Mechanical Properties of Composite Sheets

7.5.1 ASTM D882 Tensile Strength of Composite Sheets

Tensile testing is an ideal technique to display the level of adhesion and dispersion of exfoliated graphite and many layer graphene within the composite sheets. This test is a strong indicator of the more applicable structural properties needed for sheets and films. In Table 7-4, the first characteristic to notice is the average thickness for each of the extruded sheets. The thicknesses recorded in Table 7-4 are the smallest continuous sheets that can be produced. For extrudate without graphite, thinner sheets are easy to create, while filled materials require thicker extrudate. As PSU is loaded with graphite, smaller continuous thicknesses are harder to produce, but an increased number of passes through our lab scale process makes this possible. For the 2 step process, the same thickness limits exist, unrelated to degradation. Degradation may shorten the polymer chains and reduce extension in the forming process. This extension does not compare to values of PSU for strain at break, since the average sheet thickness is lower.

Table 7-4 Mechanical Properties of extruded G-PSU and PSU Sheets

Material	Thickness (mm)	Peak Stress (MPa)	Strain At Break (%)	Modulus (GPa)
PSU BB	236	16.49	3.31	0.99
G PSU C1	728	15.15	1.30	1.34
G PSU C3	429	21.08	1.10	2.40
PSU HS + BB	693	67.29	3.86	2.45
G PSU HS + BB	719	34.93	0.99	4.63

In the traditional extrusion process, the higher the number of passes increases the peak stress and modulus. The mechanical properties coincide with the idea that the smaller domain sizes of the graphite, creates higher surface area. This creates more interfacial contact of the matrix and the filler. Greater interfacial interactions lead to an

increase in modulus. The increased modulus attributes to greater stress transfer, elevating peak stress.

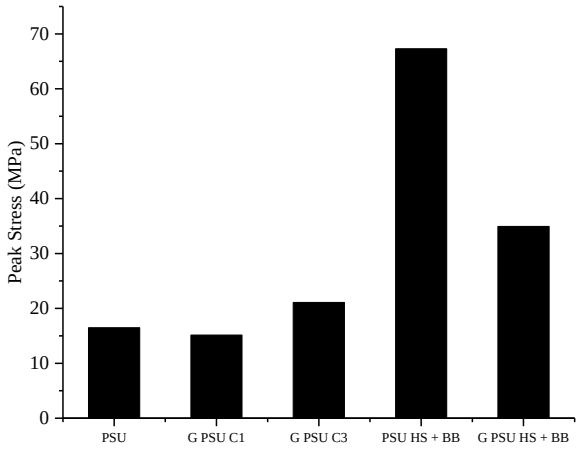

Figure 7-10 Peak stress of extruded G-PSU and PSU Sheets

A greater modulus, peak stress, and strain at break is found in PSU HS + BB compared to traditionally extruded sheets. The extrusion process, after extensional flow, eliminates the previous thermal history of the polymer. Changes in the mechanical properties are probably due to instances of crosslinking by the partial degradation within the PSU matrix. Applying this thinking to the graphite filled sheets, an increase in modulus and decrease in peaks stress is seen. Because of a modulus increase, functionalization is occurring in the matrix by an increase stress transfer. When comparing this to the sheet with multiple passes, the 2 step process has a 40 % increase in break stress and 48 % increase in modulus. This increase is dependent on both the increase in surface area and the creation of secondary functionalization. These 2 complementary features allow for better stress transfer.

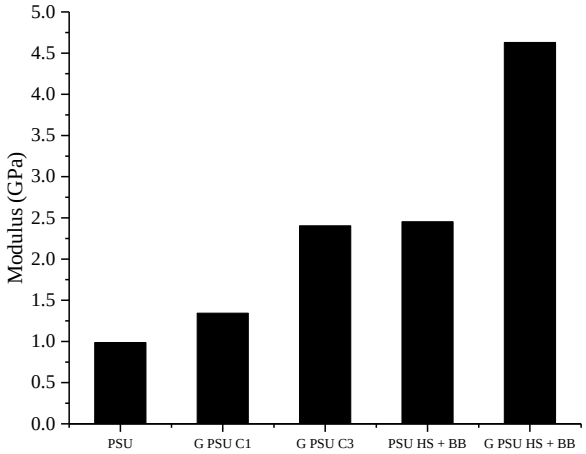

Figure 7-11 Bulk modulus of extruded G-PSU and PSU Sheets

7.6 Interfacial analysis for functionalization

7.6.1 X-ray Photoelectron Spectroscopy (XPS) of Extruded Sheets

XPS is the strongest technique to use for identifying the interfacial characteristics of extruded sheets. The results would indicate whether functionalizable groups in the polymer backbone are either oxidized or reduced due to effectiveness of the process. Looking at the extruded sheets without graphite, we see that the thinnest sheets of extruded PSU has both a strong hydroxyl and C-O-C binding energy peaks in Figure 7-12, corresponding to 167.62 eV and 531.57 eV. In the same Figure, PSU (PSU pellets) and PSU HS + BB (thick PSU sheet) are thicker than the PSU- BB film, suggesting these intensities are sensitive to orientation. Increased intensity of the peaks suggests alignment equates to increase number of characteristic species at the surface. This would increase the observed intensity in the XPS spectra.

Comparing the binding energies of extruded PSU to pellets, oxidation of sulfur and oxygen binding energies do occur, (Figure 7-1.) In sulfur SO_2, 0.1 eV, the binding

energy increase is observed in PSU BB but no change in binding energy for PSU HS + BB. This increase suggests this peak is sensitive to orientation and thickness of the film. This is apparent, since sulfur is unique to PSU and is a primary component in the backbone of the polymer chain. The overall process suggests that oxidation is occurring due to the binding energy increase of all the PSU extrudate. The increase suggests that both sheets are being oriented and oxidized, but show no sign of oxidative degradation in the extensional flow process. The interpretation is that PSU HS + BB sheets are thicker, so oxidation is not at the surface. Because XPS is surface characterization method, a depletion layer is being characterized. The depletion layer still is oxidized but lacks a change occurring in the outside layer.

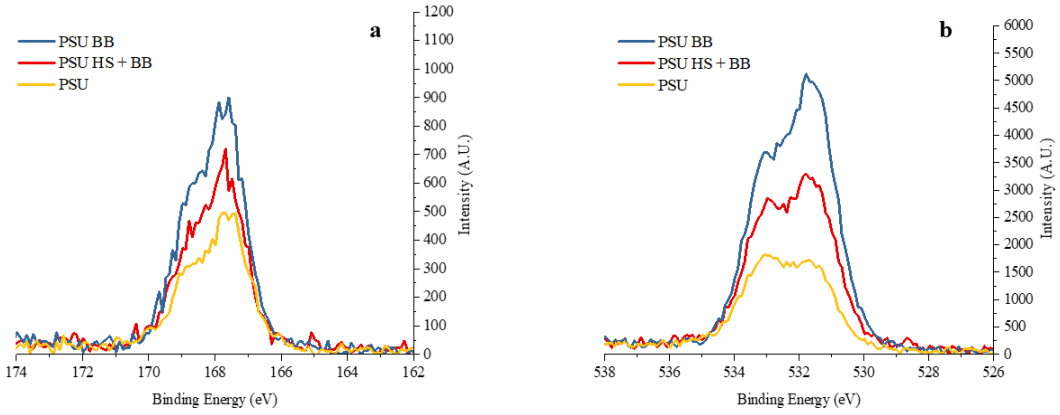

Figure 7-12 XPS spectra of PSU BB, PSU HS + BB, and PSU (a) sulfur and (b) oxygen binding energy

Table 7-5 XPS spectra of PSU BB, PSU HS + BB, and PSU sulfur and oxygen binding energy

Material	SO_2 (Sulfur, eV)	Hydroxyl - SO_2 (Sulfur, eV)	SO_2 (Oxygen, eV)	C-O-C (Oxygen, eV)
PSU BB	168.84	167.62	533.14	531.57
PSU	168.74	167.47	532.98	531.40
PSU HS + BB	168.74	167.56	533.10	531.53

For the composite sheets, the sulfur elemental peak is analyzed for contrast of the process. The previous spectra in Figure 7-1 suggested that the peak intensity was due to the orientation and presence of a thin PSU film in the surface. In Figure 7-13, the film orientation in the top surface relates to the concentration of graphite, making this more of a characterization of the degree of dispersion of graphite in the outer layer. This means that low intensity corresponds to high dispersion.

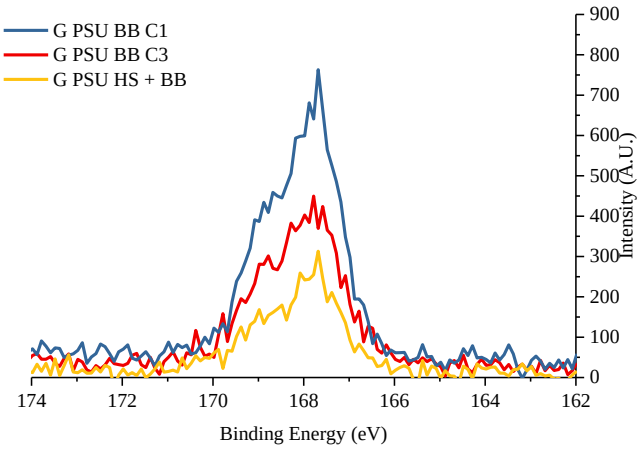

Figure 7-13 XPS spectra of G-PSU BB C1, G-PSU BB C3, and G-PSU HS + BB sulfur binding energy

For the binding energy in the exfoliation process, a single pass containing graphite, creates an oxidation in SO_2 and the hydroxyl functionalite. As the number of passes increase, the binding energy is reduced. A binding energy reduction is equated to a chemical reduction in the SO_2 functional group. In this multistep process, a reduction from results in Table 7-6 suggests electron withdrawal from the sulfur going to the π-π bond interaction at the aromatic group. This π-bond interaction is likely dominated by the lower degree of entanglement of the PSU given by extensional flow, which was defined in chapter 6. Entangled polymer chains have a higher binding energy due to proximity

effects of chain-chain interactions. Once these interactions are eliminated, polymer-graphite interactions become dominant. This allow a 0.1 eV binding energy increase in G PSU HS + BB. In terms of the Hydroxyl - SO_2, there is a 0.06 eV reduction in binding energy, but mostly due to trapped water forming the hydroxyl species. The increased number of passes aids to its reduction/elimination, but likely only due to water migration.

The takeaway from XPS is that covalent functionalization in sheets is not found in the sulfur or oxygen backbone, given by reduction of the SO_2 binding energy. Previously, we've found that the backbone of PSU is very stiff and noncompliant. In addition to that, the diphenylene sulfide group is a strong electron withdrawer, which prevents thermal degradation of the aromatic group in the backbone. This makes reduction, a secondary response to the oxidation of benzene, causing a strong electron withdrawing effect. The possibility of π-π interactions are a noncovalent interaction that can provide mechanical property improvements. In addition, the detection of covalent functionalization through carbon linkages is possible. What was observed, is that oriented films of PSU produce a strong XPS peak. As the degree of exfoliation is increases, peak intensity is decreased, due to availability or absorption by graphite. The process of the hydroxyl peak in the sulfur shows a higher binding energy with graphite. Alternatively, increasing in exfoliation shows only moderate to no oxidation, suggesting to π-π interactions in this composite system. This leads to detanglement, supported by noncovalent functionalization is a dominant factor in adhesion.

Table 7-6 XPS spectra of G-PSU BB C1, G-PSU BB C3, and G-PSU HS + BB sulfur and oxygen binding energy

Material	SO_2 (Sulfur, eV)	Hydroxyl - SO_2 (Sulfur, eV)

G PSU C1	168.95	167.71
G PSU C3	168.22	167.65
G PSU HS + BB	168.33	167.66

7.7 Closure

Extensional flow exfoliation leads to noncovalent functionalization of graphite and many layer graphene with polysulfone. The XPS results show a depletion of the sulfur and oxygen species, suggesting an electron withdrawing effect created by the π-π bond secondary chemical interactions. Functionalization allows for better stress transfer of matrix to filler, leading to increased stiffness and breaking stress. The size reduction process creates high surface area of the graphene exfoliate, while disrupting the alignment of stacked graphene sheets. The planar disruption in the graphitic stack, creates nano-grooves in the edge. By the exfoliation process, the nano-grooves create structures where soft epitaxy is dominant. This causes edge adhesion of PSU to the many layer graphene and graphite.

The extensional flow step in a scalable process causes degradation, but its effects are reduced by the presence of graphene in general. The mechanical property results suggest that even though there is presence of degradation, it has no detrimental effect to mechanical performance of a graphene containing composite sheet. The mechanochemical relationship suggests a property improvement by increasing surface area, causing soft epitaxy of polymer on nano-filler. Soft epitaxy is fortified by the creation of noncovalent functionalization at the interface of an extended polymer, creating π- π bond interactions. Those combined effects with the anisotropy of the

microstructure causes improved stress transfer, by collective noncovalent functionalization.

7.8 Appendix

7.8.1 Differential Scanning Calorimetry

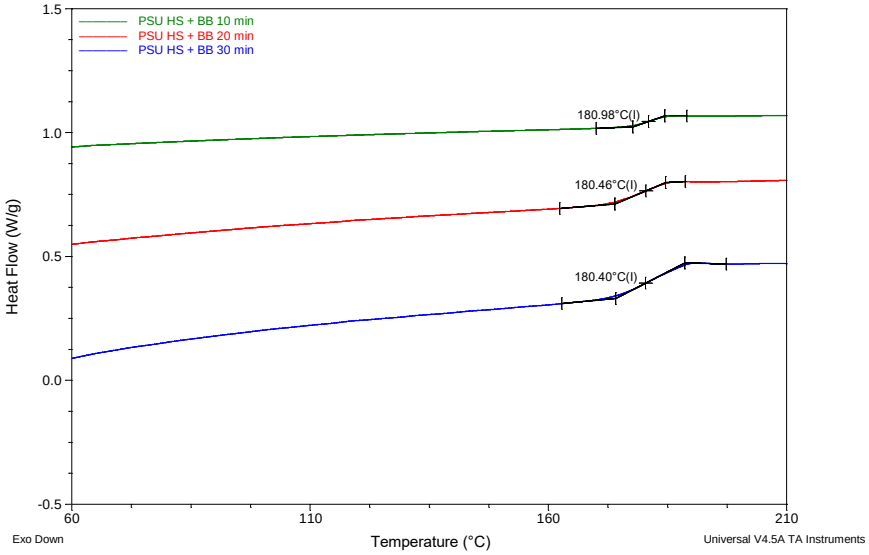

Figure 7-14 DSC of PSU HS + BB 10, 20, 30 min/°C

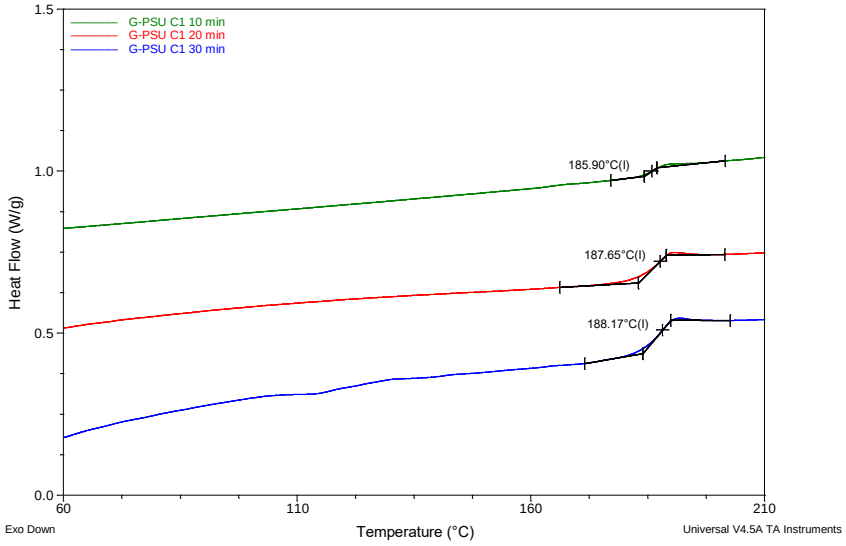

Figure 7-15 DSC of G-PSU C1 10, 20, 30 min/°C

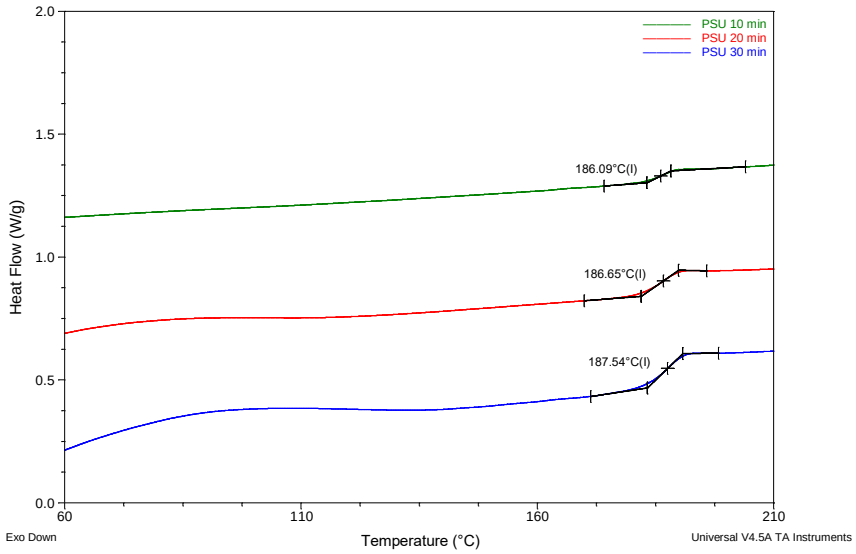

Figure 7-16 DSC of PSU 10, 20, 30 min/°C

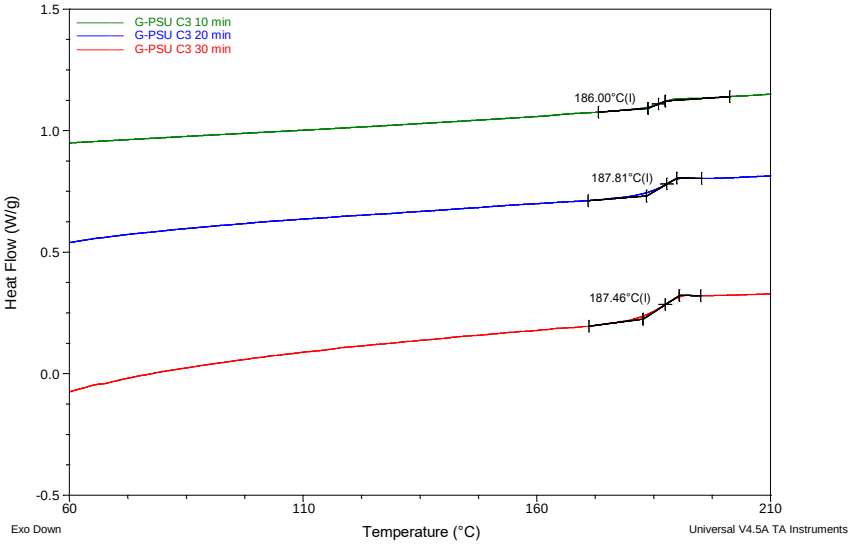

Figure 7-17 DSC of G-PSU C3 10, 20, 30 min/°C

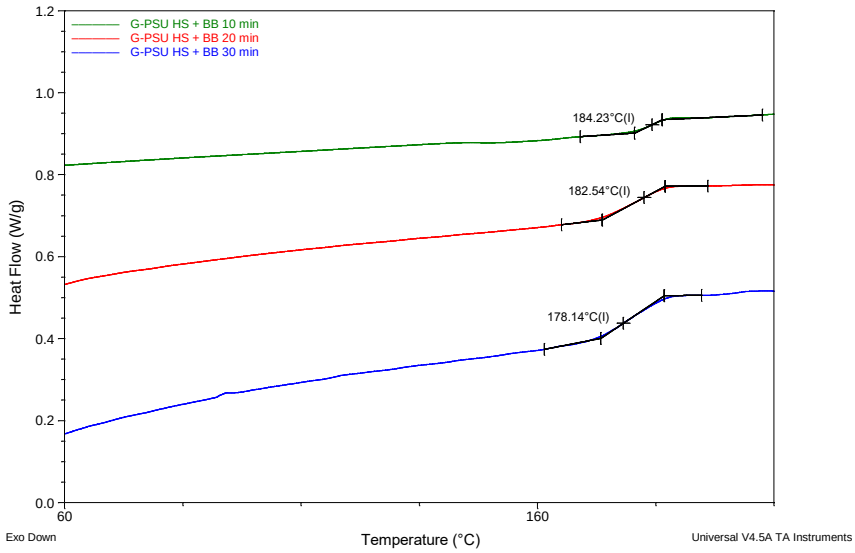

Figure 7-18 DSC of G-PSU HS + BB 10, 20, 30 min/°C

7.7.2 Mechanical Properties

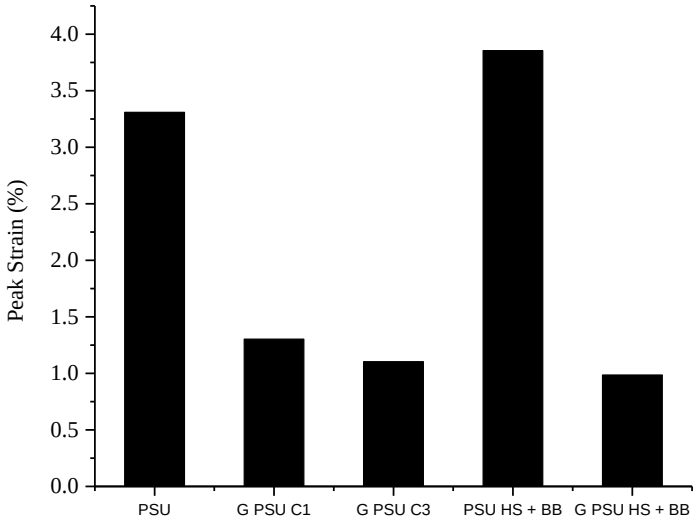

Figure 7-19 Peak strain of extruded G-PSU and PSU Sheets

Table 7-7 Standard deviation of mechanical properties of extruded sheets

Material	Thickness	Peak Stress	Strain At Break	Modulus
PSU	9	2.18	0.58	0.07
G PSU C1	82	4.57	0.30	0.30
G PSU C3	98	7.58	0.32	0.50

PSU HS + BB	180	10.54	0.73	0.43
G PSU HS + BB	73	8.56	0.27	0.60

7.7.3 XPS Fit Peak

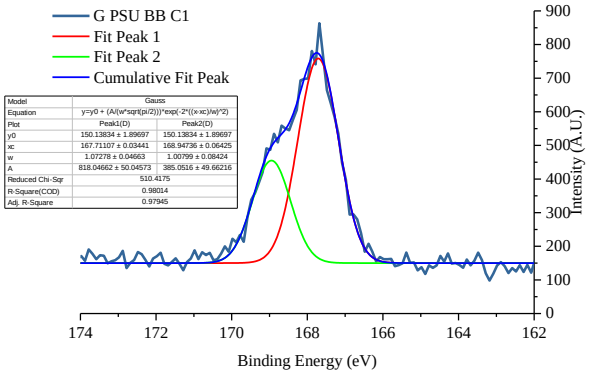

Figure 7-20 XPS of sulfur 1s G-PSU BB C1 Peak fitting

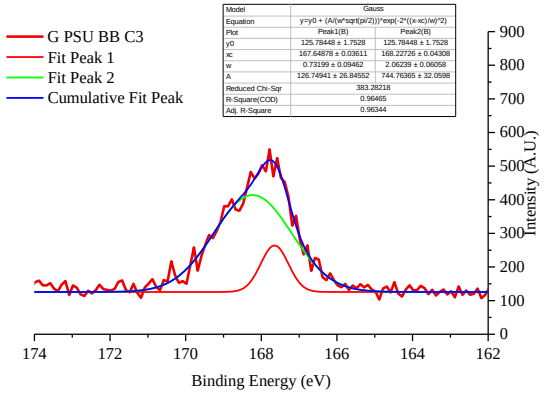

Figure 7-21 XPS of sulfur 1s G-PSU BB C3 Peak fitting

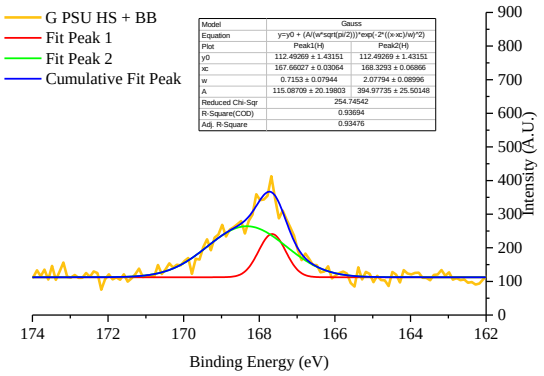

Figure 7-22 XPS of sulfur 1s G-PSU BB HS + BB peak fitting

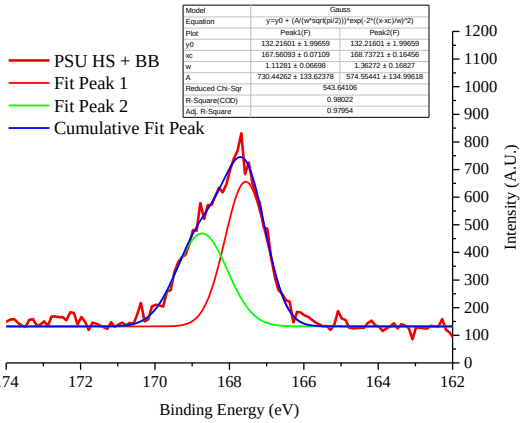

Figure 7-23 XPS of sulfur 1s PSU HS + BB peak fitting

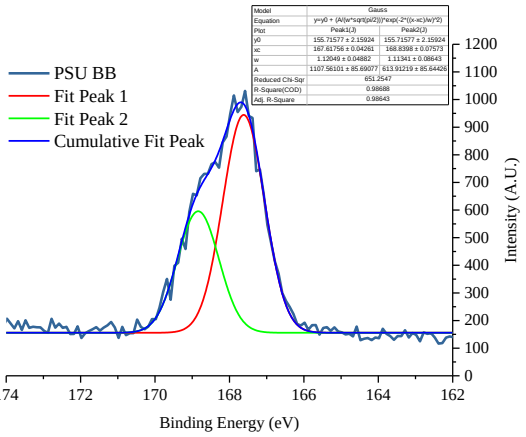

Figure 7-24 XPS of sulfur 1s PSU BB peak fitting

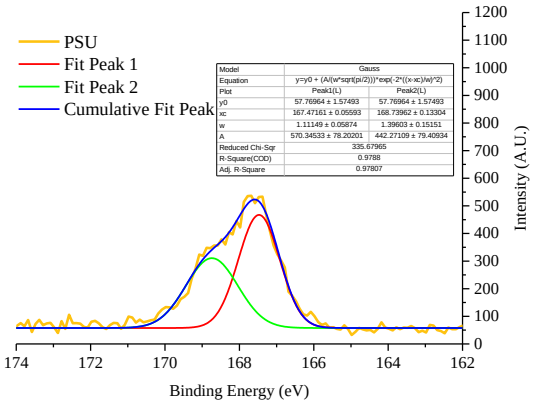

Figure 7-25 XPS of sulfur 1s PSU peak fitting

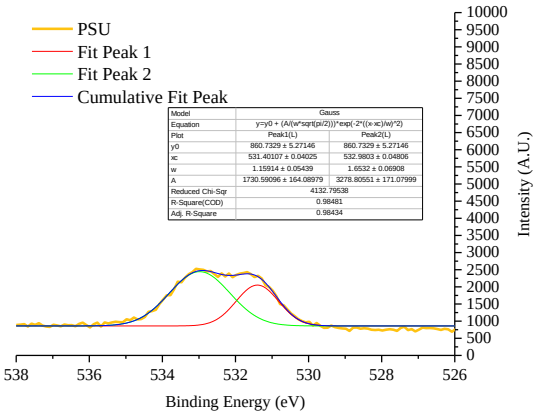

Figure 7-26 XPS of oxygen 1s PSU peak fitting

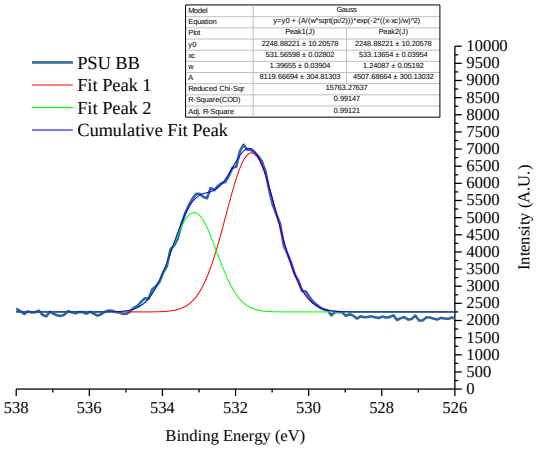

Figure 7-27 XPS of oxygen 1s PSU BB peak fitting

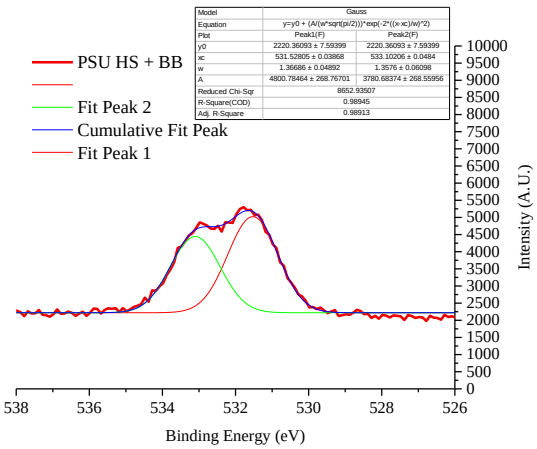

Figure 7-28 XPS of oxygen 1s PSU HS + BB peak fitting

Chapter 8 Conclusion and Recommendations

8.1 Summary

A novel process that creates graphene from flake graphite in-situ was investigated. Graphite was reduced to few and many layer graphene by a process that caused large scale fragmentation through planar sheet ripping and surface erosion. Fragmentation was dominated by external fluid stress in the outer layers of flake graphite. The stress induced top layer disruption of the exfoliated graphene flake, causing stacking faults and misalignment of the graphitic layers (turbostratic graphite). Surface free radicalization was dominated by activation on the graphene zig-zag edge, creating dangling bonds in-situ. A third process was likely diffusion assisted exfoliation, which further reduce the size of graphite. Diffusive exfoliation was found when the shear strain rate was increased by 3x creating a plurality of graphene layers. This exfoliation created smaller graphitic domains, leading to an increase in exfoliation. As we mentioned early, these crystalline domains were calculated to be ~14 nm in size and representing an upper limit approximation to the domain size in the (002) direction. This approximation is obtain by experimental conditions utilized in our diffraction experiment. The resulting fewer layer flakes of graphene were found not resolvable, given the experimental conditions. Quantifying a higher concentration of few layer graphene flakes would be best obtained using a combination of x-ray source (synchrotron), synthetically derived graphene of known size, or a combination of crystalline standards. Due to this fact, we believe that a plurality of graphene flakes sizes exist in a high concentration but are

captured in the background due to their smaller crystalline domains and shear exfoliated condition.

Under the same exfoliation conditions, high-speed extensional flow was found to elongate the polymer, creating a proposed 1D high potential energy surface. Under high elongation, semi-crystalline polymers chains are believed to be closer, given by their alteration in radius of gyration leading to low steric hindrances via conformation changes. Amorphous polymers were driven to detangle at the interface, providing lower interaction between polymer chain by their smaller activation energy and lack of steric hindrances.

Through the characterization of these exfoliated composites, the polymer crystalline domain size was found to infer the type of exfoliation and degree of functionalization. The aspect ratio of these domains was used to differentiate secondary and primary bonding that was formed. For crystallite domains with anisotropy domains elongated in (100) direction for PA66, edge and surface functionalization was suggested to occur. This lead to oxidation of nitrogen in the amide of PA66 and the conversion of sp2 to sp3 carbon in the graphite edge surface (covalent

The process has shown that for sulfur contain aromatic polymers (PPS and PSU), the addition of graphene has led to antioxidant effect in the composite. This antioxidation was supported by noncovalent functionalization by aromatic rings in the polymer backbone creating π-π bond stacking at the interface. This lead to apparent binding energy reduction by surface characterization. The increase in the degree of exfoliation has also found that the glass transition temperature and melting temperature were reduced. The reduction of thermal properties to degree of exfoliation has suggested improved heat distribution to catalyze the melting process. This catalytic heating in the

presence of the graphite was supported by oriented polymer crystalline domains, hydrogen bond disruption, and polymer chain extension.

These combined effects have lead to graphene reinforced composites with improved mechanical properties by their increase in modulus. For the difference in resulting functionalization, primary and secondary bonding lead to improved break stress and modulus of the resulting composite. Noncovalent bonding supported by π-π stacking from the aromatic group in the polymer backbone improved mechanical properties due to its retention of graphene's structure. This lead to better stress transfer between graphene to the polymer matrix, creating a composite with improved properties due to graphene reinforcement.

8.2 Future Work

Through researching these systems, we've found that diffusion assisted exfoliation played a major role in extensional flow. The high anisotropic flow created by the mixing process lead to the discovery of a gap in our understanding of non-fickian diffusion. How we interpret the intercalation of polymeric molecules through graphitic galleries is still in it earlier stage, given by own models in the supporting chapters. This leaves an opening to the idea that in a continuous process, the boundary (interface) between compositing materials can be highly active to surface assisted reactions. This discovery may be interesting to apply in other complex composite systems that may be augmented without the addition of prior chemical modification. Likewise, high shear rate mixing may aid in producing more efficient large scale continuous extruders. This would increase the throughput for large scale nanosdomain composites.

Additionally, it would be interesting to tailor the exfoliation of other types of 2D filler in sol gels, to create unique interfacial structures. Mixing with boron nitride (BN), Tungsten disulfide (WS2), Molybdenum disulfide (MoS2), or other 1D/2D/3D covalent organic framework may lead to scalable production of composites (polymer or preceramic) with exotic properties.

Chapter 9 Bibliography

1. Yan, Z., D.L. Nika, and A.A. Balandin, *Thermal properties of graphene and few-layer graphene: applications in electronics.* IET Circuits, Devices & Systems, 2015. **9**(1): p. 4-12.
2. Miculescu, M., et al., *Graphene-based polymer nanocomposite membranes: a review.* Polymers for Advanced Technologies, 2016. **27**(7): p. 844-859.
3. Kim, H., A.A. Abdala, and C.W. Macosko, *Graphene/Polymer Nanocomposites.* Macromolecules, 2010. **43**(16): p. 6515-6530.
4. Perreault, F., A.F. de Faria, and M. Elimelech, *Environmental applications of graphene-based nanomaterials.* Chemical Society Reviews, 2015. **44**(16): p. 5861-5896.
5. Talat, M. and O. Srivastava, *Deployment of New Carbon Nanostructure: Graphene for Drug Delivery and Biomedical Applications*, in *Advances in Nanomaterials*. 2016, Springer. p. 383-395.
6. Hao, F., D. Fang, and Z. Xu, *Mechanical and thermal transport properties of graphene with defects.* Applied Physics Letters, 2011. **99**(4): p. 041901.
7. Chen, Y., et al., *Two-dimensional graphene analogues for biomedical applications.* Chemical Society Reviews, 2015. **44**(9): p. 2681-2701.
8. Frank, I.W., et al., *Mechanical properties of suspended graphene sheets.* Journal of Vacuum Science & Technology B: Microelectronics and Nanometer Structures, 2007. **25**(6): p. 2558.
9. Yang, S., et al., *Organic radical-assisted electrochemical exfoliation for the scalable production of high-quality graphene.* Journal of the American Chemical Society, 2015. **137**(43): p. 13927-13932.
10. Bélanger, D. *One-Pot Electrochemical Exfoliation and Functionalization of Graphene Sheets*. in *229th ECS Meeting (May 29-June 2, 2016)*. 2016. Ecs.
11. Wassei, J.K. and R.B. Kaner, *Oh, the Places You'll Go with Graphene.* Accounts of Chemical Research, 2013. **46**(10): p. 2244-2253.
12. Chua, C.K. and M. Pumera, *Chemical reduction of graphene oxide: a synthetic chemistry viewpoint.* Chemical Society Reviews, 2014. **43**(1): p. 291-312.
13. Manna, K., et al., *Graphene and graphene-analogue nanosheets produced by efficient water-assisted liquid exfoliation of layered materials.* Carbon, 2016.
14. Haar, S., et al., *A Supramolecular Strategy to Leverage the Liquid-Phase Exfoliation of Graphene in the Presence of Surfactants: Unraveling the Role of the Length of Fatty Acids.* Small, 2015. **11**(14): p. 1691-1702.
15. Vicarelli, L., et al., *Controlling Defects in Graphene for Optimizing the Electrical Properties of Graphene Nanodevices.* ACS Nano, 2015. **9**(4): p. 3428-3435.
16. McCrum, N.G., C.P. Buckley, and C.B. Bucknall, *Principles of Polymer Engineering*. 1997: Oxford University Press.
17. Tadmor, Z. and C.G. Gogos, *Principles of Polymer Processing*. 2013: Wiley.
18. Wilkinson, A.N. and A.J. Ryan, *Polymer Processing and Structure Development*. 1998: Springer Netherlands.
19. Ray, S.S., *Clay-Containing Polymer Nanocomposites: From Fundamentals to Real Applications*. 2013: Elsevier Science.

20. Quigley, J.P. and D.G. Baird, *Improved mechanical properties of organoclay/nylon 6 nanocomposites prepared via a supercritical carbon dioxide-aided, melt blending method.* Polymer Composites, 2015. **36**(3): p. 527-537.
21. Dolez, P.I., *Nanoengineering: Global Approaches to Health and Safety Issues*. 2015: Elsevier Science.
22. Crompton, T.R., *Plastics Reinforcement and Industrial Applications*. 2015: CRC Press.
23. Airale, A.G., et al., *Moisture effect on mechanical properties of polymeric composite materials.* AIP Conference Proceedings, 2016. **1736**(1): p. 020020.
24. Gu, J., et al., *Thermal conductivities, mechanical and thermal properties of graphite nanoplatelets/polyphenylene sulfide composites.* RSC Advances, 2014. **4**(42): p. 22101-22105.
25. Yang, S.Y., et al., *Nanoporous membranes with ultrahigh selectivity and flux for the filtration of viruses.* Advanced materials, 2006. **18**(6): p. 709-712.
26. Kim, S. and E. Marand, *High permeability nano-composite membranes based on mesoporous MCM-41 nanoparticles in a polysulfone matrix.* Microporous and Mesoporous Materials, 2008. **114**(1-3): p. 129-136.
27. Pawlowski, L., *Physicochemical Methods for Water and Wastewater Treatment*. 1982: Elsevier Science.
28. Morelos-Gomez, A., et al., *Effective NaCl and dye rejection of hybrid graphene oxide/graphene layered membranes.* Nature Nanotechnology, 2017. **12**: p. 1083.
29. Khaled, S., et al., *Synthesis of TiO2− PMMA nanocomposite: Using methacrylic acid as a coupling agent.* Langmuir, 2007. **23**(7): p. 3988-3995.
30. Kumar, S., et al., *Fibers from polypropylene/nano carbon fiber composites.* Polymer, 2002. **43**(5): p. 1701-1703.
31. Kenny, J. and A. Maffezzoli, *Crystallization kinetics of poly (phenylene sulfide)(PPS) and PPS/carbon fiber composites.* Polymer Engineering & Science, 1991. **31**(8): p. 607-614.
32. Zare, Y., *New models for yield strength of polymer/clay nanocomposites.* Composites Part B: Engineering, 2015. **73**: p. 111-117.
33. Chen, B. and J.R. Evans, *Elastic moduli of clay platelets.* Scripta materialia, 2006. **54**(9): p. 1581-1585.
34. Mark, J.E., *Physical properties of polymers handbook*. Vol. 1076. 2007: Springer.
35. Fu, X. and S. Qutubuddin, *Polymer–clay nanocomposites: exfoliation of organophilic montmorillonite nanolayers in polystyrene.* Polymer, 2001. **42**(2): p. 807-813.
36. Choi, Y.S., M. Xu, and I.J. Chung, *Synthesis of exfoliated acrylonitrile–butadiene–styrene copolymer (ABS) clay nanocomposites: role of clay as a colloidal stabilizer.* Polymer, 2005. **46**(2): p. 531-538.
37. Farahanchi, A., R.A. Malloy, and M.J. Sobkowicz, *Extreme shear processing for exfoliating organoclay in nanocomposites with incompatible polymers.* Polymer, 2018. **145**: p. 117-126.
38. Schwarz, J.A., C.I. Contescu, and K. Putyera, *Dekker Encyclopedia of Nanoscience and Nanotechnology*. 2004: M. Dekker.
39. Koratkar, N.A., *Graphene in composite materials: synthesis, characterization and applications*. 2013: DEStech Publications, Inc.
40. Wolf, E.L., *Graphene: A New Paradigm in Condensed Matter and Device Physics*. 2013: OUP Oxford.

41. Thakur, V.K. and M.K. Thakur, *Chemical Functionalization of Carbon Nanomaterials: Chemistry and Applications*. 2015: CRC Press.
42. Nosker, T.S., NJ, US), Lynch, Jennifer K. (Franklin Park, NJ, US), Kear, Bernard (Whitehouse Station, NJ, US), Hendrix, Justin (Washington, DC, US), Chiu, Gordon (Summit, NJ, US), *Graphene-Reinforced Polymer Matrix Composites*. 2017, Rutgers, The State University of New Jersey (New Brunswick, NJ, US): United States.
43. Taylor, G.I., *The Formation of Emulsions in Definable Fields of Flow.* Proceedings of the Royal Society of London. Series A, Containing Papers of a Mathematical and Physical Character, 1934. **146**(858): p. 501-523.
44. Rumscheidt, F.D. and S.G. Mason, *Particle motions in sheared suspensions XII. Deformation and burst of fluid drops in shear and hyperbolic flow.* Journal of Colloid Science, 1961. **16**(3): p. 238-261.
45. Aguilera, J.M., et al., *Food Engineering Interfaces*. 2010: Springer New York.
46. Grace†, H.P., *DISPERSION PHENOMENA IN HIGH VISCOSITY IMMISCIBLE FLUID SYSTEMS AND APPLICATION OF STATIC MIXERS AS DISPERSION DEVICES IN SUCH SYSTEMS.* Chemical Engineering Communications, 1982. **14**(3-6): p. 225-277.
47. Sing, C.E. and A. Alexander-Katz, *Globule–Stretch Transitions of Collapsed Polymers in Elongational Flow Fields.* Macromolecules, 2010. **43**(7): p. 3532-3541.
48. Stone, P.A., et al., *Dynamics of Wormlike Micelles in Elongational Flows.* Macromolecules, 2006. **39**(20): p. 7144-7148.
49. De Gennes, P.G., *Coil-stretch transition of dilute flexible polymers under ultrahigh velocity gradients.* The Journal of Chemical Physics, 1974. **60**(12): p. 5030-5042.
50. Smith, D.E. and S. Chu, *Response of Flexible Polymers to a Sudden Elongational Flow.* Science, 1998. **281**(5381): p. 1335-1340.
51. Grosberg, A.I.U., A.R. Khokhlov, and P.G. de Gennes, *Giant Molecules: Here, There, and Everywhere*. 2011: World Scientific.
52. Nguyen, T.Q. and H.H. Kausch, *Flexible Polymer Chains in Elongational Flow: Theory and Experiment*. 2012: Springer Berlin Heidelberg.
53. Marrucci, G., *The Free Energy Constitutive Equation for Polymer Solutions from the Dumbbell Model.* Transactions of the Society of Rheology, 1972. **16**(2): p. 321-330.
54. Gordon, N.D., et al., *Stream Hydrology: An Introduction for Ecologists*. 2013: Wiley.
55. Levine, A.J., T.B. Liverpool, and F.C. MacKintosh, *Mobility of extended bodies in viscous films and membranes.* Physical Review E, 2004. **69**(2): p. 021503.
56. Wilkinson, K.J. and J.R. Lead, *Environmental Colloids and Particles: Behaviour, Separation and Characterisation*. 2007: Wiley.
57. Livadaru, L., R.R. Netz, and H.J. Kreuzer, *Stretching Response of Discrete Semiflexible Polymers.* Macromolecules, 2003. **36**(10): p. 3732-3744.
58. Stephanou, P.S., I.C. Tsimouri, and V.G. Mavrantzas, *Flow-Induced Orientation and Stretching of Entangled Polymers in the Framework of Nonequilibrium Thermodynamics.* Macromolecules, 2016. **49**(8): p. 3161-3173.
59. Vassileva, N.D., et al., *Restructuring and Break-Up of Two-Dimensional Aggregates in Shear Flow.* Langmuir, 2006. **22**(11): p. 4959-4967.
60. Start, P.R., et al., *Breakup of carbon nanotube flocs in microfluidic traps.* Journal of Colloid and Interface Science, 2006. **297**(2): p. 631-636.

61. Vilaverde, C., et al., *Dispersion and re-agglomeration of graphite nanoplates in polypropylene melts under controlled flow conditions.* Composites Part A: Applied Science and Manufacturing, 2015. **78**: p. 143-151.
62. Paul, D.R. and L.M. Robeson, *Polymer nanotechnology: Nanocomposites.* Polymer, 2008. **49**(15): p. 3187-3204.
63. Borse, N.K. and M.R. Kamal, *Estimation of stresses required for exfoliation of clay particles in polymer nanocomposites.* Polymer Engineering & Science, 2009. **49**(4): p. 641-650.
64. Giannelis, E.P., *Polymer Layered Silicate Nanocomposites.* Advanced Materials, 1996. **8**(1): p. 29-35.
65. Georgakilas, V., *Functionalization of Graphene*. 2014: Wiley.
66. Yang, N., *The Preparation of Nano Composites and Their Applications in Solar Energy Conversion*. 2016: Springer Berlin Heidelberg.
67. Georgakilas, V., et al., *Functionalization of Graphene: Covalent and Non-Covalent Approaches, Derivatives and Applications.* Chemical Reviews, 2012. **112**(11): p. 6156-6214.
68. Boukhvalov, D.W. and M.I. Katsnelson, *Chemical Functionalization of Graphene with Defects.* Nano Letters, 2008. **8**(12): p. 4373-4379.
69. Boukhvalov, D.W. and M.I. Katsnelson, *Chemical functionalization of graphene.* Journal of Physics: Condensed Matter, 2009. **21**(34): p. 344205.
70. Kutz, M., *Applied Plastics Engineering Handbook: Processing, Materials, and Applications*. 2016: Elsevier Science.
71. Mallick, P.K., *Processing of Polymer Matrix Composites: Processing and Applications*. 2017: CRC Press.
72. Vogel, H.C. and C.M. Todaro, *Fermentation and Biochemical Engineering Handbook: Principles, Process Design and Equipment*. 1996: Elsevier Science.
73. Yin, J., G. Zhu, and B. Deng, *Multi-walled carbon nanotubes (MWNTs)/polysulfone (PSU) mixed matrix hollow fiber membranes for enhanced water treatment.* Journal of membrane science, 2013. **437**: p. 237-248.
74. Kricheldorf, H.R., *Handbook of Polymer Synthesis: Part B (In Two Parts)*. 1991: Taylor & Francis.
75. ASTM, D., *638-03: Standard Test Method for Tensile Properties of Plastics.* Current edition approved Apr, 2008. **1**: p. 1-16.
76. Goldstein, J.I., et al., *Scanning Electron Microscopy and X-Ray Microanalysis*. 2017: Springer New York.
77. Kotz, J., P. Treichel, and J. Townsend, *Chemistry and Chemical Reactivity*. 2008: Cengage Learning.
78. Carter, C.B. and D.B. Williams, *Transmission Electron Microscopy: Diffraction, Imaging, and Spectrometry*. 2016: Springer International Publishing.
79. Lewandowski, Z. and H. Beyenal, *Fundamentals of Biofilm Research, Second Edition*. 2013: CRC Press.
80. Jackson, S.D. and J.S.J. Hargreaves, *Metal Oxide Catalysis*. 2009: Wiley.
81. Koster, G. and G. Rijnders, *In Situ Characterization of Thin Film Growth*. 2011: Elsevier Science.
82. Chung, Y.W., *Practical Guide to Surface Science and Spectroscopy*. 2012: Elsevier Science.

83. Liengen, T., et al., *Understanding Biocorrosion: Fundamentals and Applications*. 2014: Elsevier Science.
84. Lou, L., *Introduction to Phonons and Electrons*. 2003: World Scientific.
85. Ooi, L., *Principles of X-ray Crystallography*. 2010: OUP Oxford.
86. Gedde, U., *Polymer Physics*. 1995: Springer Netherlands.
87. Zhao, Y. and J. Zhang, *Microstrain and grain-size analysis from diffraction peak width and graphical derivation of high-pressure thermomechanics.* Journal of Applied Crystallography, 2008. **41**(6): p. 1095-1108.
88. Kumar, C.S.S.R., *Raman Spectroscopy for Nanomaterials Characterization*. 2012: Springer.
89. Jorio, A., et al., *Raman Spectroscopy in Graphene Related Systems*. 2011: Wiley.
90. Mohiuddin, T.M.G., et al., *Uniaxial strain in graphene by Raman spectroscopy: G peak splitting, Gr\"uneisen parameters, and sample orientation.* Physical Review B, 2009. **79**(20): p. 205433.
91. Yang, X.X., et al., *Raman spectroscopic determination of the length, strength, compressibility, Debye temperature, elasticity, and force constant of the C–C bond in graphene.* Nanoscale, 2012. **4**(2): p. 502-510.
92. Inés, S.-E., et al., *The nature of graphene–metal bonding probed by Raman spectroscopy: the special case of cobalt.* Journal of Physics D: Applied Physics, 2016. **49**(10): p. 105301.
93. Lu, P., et al., *Suppression of fluorescence in raman spectroscopy of chromophore-containing polymer samples.* Macromolecular Rapid Communications, 1994. **15**(11): p. 835-840.
94. Friedrich, K., S. Fakirov, and Z. Zhang, *Polymer Composites: From Nano- to Macro-Scale*. 2005: Springer US.
95. Worgull, M., *Hot Embossing: Theory and Technology of Microreplication*. 2009: Elsevier Science.
96. Scheirs, J., *Compositional and Failure Analysis of Polymers: A Practical Approach*. 2000: Wiley.
97. Kissinger, H.E., *Reaction Kinetics in Differential Thermal Analysis.* Analytical Chemistry, 1957. **29**(11): p. 1702-1706.
98. Chung, D.D.L., *Composite Materials: Science and Applications*. 2010: Springer London.
99. Barun, D., et al., *Nano-indentation studies on polymer matrix composites reinforced by few-layer graphene.* Nanotechnology, 2009. **20**(12): p. 125705.
100. Acton, Q.A., *Issues in Materials and Manufacturing Research: 2011 Edition*. 2012: ScholarlyEditions.
101. Zhang, G., et al., *Preparation of polymer/clay nanocomposites via melt intercalation under continuous elongation flow.* Composites Science and Technology, 2017. **145**: p. 157-164.
102. Ali, Z., et al., *Nanoclay exfoliation in rubber compounds characterized by online measurements of electrical conductance.* Journal of Applied Polymer Science, 2009. **113**(1): p. 667-677.
103. Kreczak, H., R. Sturman, and M.C. Wilson, *Deceleration of one-dimensional mixing by discontinuous mappings.* Physical Review E, 2017. **96**(5): p. 053112.
104. Tabor, B.J., E.P. Magré, and J. Boon, *The crystal structure of poly-p-phenylene sulphide.* European Polymer Journal, 1971. **7**(8): p. 1127-1133.

105. Qian, X.J., S.E. Rickert, and J.B. Lando, *Epitaxial crystallization of polyphenylene sulfide on sodium chloride.* Journal of Materials Research, 2011. **4**(4): p. 996-1004.
106. Hay, J.N. and D.A. Luck, *The conformation of crystalline poly(phenylene sulphide).* Polymer, 2001. **42**(19): p. 8297-8301.
107. Liu, F., et al., *Folded Structured Graphene Paper for High Performance Electrode Materials.* Advanced Materials, 2012. **24**(8): p. 1089-1094.
108. Tayran, C., et al., *Optimizing Electronic Structure and Quantum Transport at the Graphene-Si(111) Interface: An Ab Initio Density-Functional Study.* Physical Review Letters, 2013. **110**(17): p. 176805.
109. Louette, P., F. Bodino, and J.-J. Pireaux, *Poly (phenylene sulfide)(PPS) XPS Reference Core Level and Energy Loss Spectra.* Surface Science Spectra, 2005. **12**(1): p. 169-173.
110. Xing, J., Z. Xu, and B. Deng, *Enhanced Oxidation Resistance of Polyphenylene Sulfide Composites Based on Montmorillonite Modified by Benzimidazolium Salt.* Polymers, 2018. **10**(1): p. 83.
111. Amend, J.P., K.J. Edwards, and T.W. Lyons, *Sulfur Biogeochemistry: Past and Present*. 2004: Geological Society of America.
112. Schrader, G.F. and A.K. Elshennawy, *Manufacturing Processes and Materials, Fourth Edition*. 2000: Society of Manufacturing Engineers.
113. Mark, H.F., *Encyclopedia of Polymer Science and Technology, Concise*. 2013: Wiley.
114. Hoa, S.V., *Design and Manufacturing of Composites, Second Edition*. 1998: Taylor & Francis.
115. Altmann, J., *Military Nanotechnology: Potential Applications and Preventive Arms Control*. 2007: Taylor & Francis.
116. Perkins, T.T., D.E. Smith, and S. Chu, *Single Polymer Dynamics in an Elongational Flow.* Science, 1997. **276**(5321): p. 2016-2021.
117. Gennes, P.G.D., *Coil-stretch transition of dilute flexible polymers under ultrahigh velocity gradients.* The Journal of Chemical Physics, 1974. **60**(12): p. 5030-5042.
118. Sperling, L.H., *Introduction to Physical Polymer Science*. 2015: Wiley.
119. Boyer, R.F., *Dependence of mechanical properties on molecular motion in polymers.* Polymer Engineering & Science, 1968. **8**(3): p. 161-185.
120. Kissinger, H.E., *Variation of peak temperature with heating rate in differential thermal analysis.* Journal of research of the National Bureau of Standards, 1956. **57**(4): p. 217-221.
121. Wellen, R.M.R. and E.L. Canedo, *On the Kissinger equation and the estimate of activation energies for non-isothermal cold crystallization of PET.* Polymer Testing, 2014. **40**: p. 33-38.
122. Nosker, T.J., *Rate-dependence of the glass transition pressure on poly (vinylidiene fluoride) and poly (methyl methacrylate).* 1989.
123. Di Bernardo, A., et al., *p-wave triggered superconductivity in single-layer graphene on an electron-doped oxide superconductor.* Nature Communications, 2017. **8**: p. 14024.
124. Schadler, L.S., S.C. Giannaris, and P.M. Ajayan, *Load transfer in carbon nanotube epoxy composites.* Applied Physics Letters, 1998. **73**(26): p. 3842-3844.
125. Quiles-Díaz, S., et al., *Influence of the chemical functionalization of graphene on the properties of polypropylene-based nanocomposites.* Composites Part A: Applied Science and Manufacturing, 2017. **100**(Supplement C): p. 31-39.

126. Ragoussi, M.-E., et al., *Electron-Donating Behavior of Few-Layer Graphene in Covalent Ensembles with Electron-Accepting Phthalocyanines.* Journal of the American Chemical Society, 2014. **136**(12): p. 4593-4598.
127. Xiao, T., J. Liu, and H. Xiong, *Effects of different functionalization schemes on the interfacial strength of carbon nanotube polyethylene composite.* Acta Mechanica Solida Sinica, 2015. **28**(3): p. 277-284.
128. Buzanowski, M.A. and R.T. Yang, *Approximations for intraparticle diffusion rates in cyclic adsorption and desorption.* Chemical Engineering Science, 1991. **46**(10): p. 2589-2598.
129. Jones, N.A., E.D.T. Atkins, and M.J. Hill, *Investigation of solution-grown, chain-folded lamellar crystals of the even-even nylons: 6 6, 8 6, 8 8, 10 6, 10 8, 10 10, 12 6, 12 8, 12 10, and 12 12.* Journal of Polymer Science Part B: Polymer Physics, 2000. **38**(9): p. 1209-1221.
130. Starr, F.W., T.B. Schrøder, and S.C. Glotzer, *Molecular Dynamics Simulation of a Polymer Melt with a Nanoscopic Particle.* Macromolecules, 2002. **35**(11): p. 4481-4492.
131. Lopes dos Santos, J.M.B., N.M.R. Peres, and A.H. Castro Neto, *Graphene Bilayer with a Twist: Electronic Structure.* Physical Review Letters, 2007. **99**(25): p. 256802.
132. Haberkorn, H., K.H. Illers, and P. Simak, *Molekülordnung und Kristallinität in Polyhexamethylenadipamid.* Colloid and Polymer Science. **257**(8): p. 820-840.
133. Khanna, Y.P., *Overview of transition phenomenon in nylon 6.* Macromolecules, 1992. **25**(12): p. 3298-3300.
134. Zhang, F., et al., *Isothermal crystallization kinetics of in situ Nylon 6/graphene composites by differential scanning calorimetry.* Polymer Engineering & Science, 2014. **54**(11): p. 2610-2616.
135. Aoyama, S., et al., *Melt crystallization of poly(ethylene terephthalate): Comparing addition of graphene vs. carbon nanotubes.* Polymer, 2014. **55**(8): p. 2077-2085.
136. Kim, S., et al., *Thermal diffusivity of in-situ exfoliated graphite intercalated compound/polyamide and graphite/polyamide composites.*
137. Sawyer, L.C., *Polymer Microscopy*. 2012: Springer Netherlands.
138. Stankovich, S., et al., *Synthesis of graphene-based nanosheets via chemical reduction of exfoliated graphite oxide.* carbon, 2007. **45**(7): p. 1558-1565.
139. Eda, G., G. Fanchini, and M. Chhowalla, *Large-area ultrathin films of reduced graphene oxide as a transparent and flexible electronic material.* Nature nanotechnology, 2008. **3**(5): p. 270.
140. Bianco, A., et al., *All in the graphene family – A recommended nomenclature for two-dimensional carbon materials.* Carbon, 2013. **65**(Supplement C): p. 1-6.
141. Shenoy, V.B., C.D. Reddy, and Y.-W. Zhang, *Spontaneous Curling of Graphene Sheets with Reconstructed Edges.* ACS Nano, 2010. **4**(8): p. 4840-4844.
142. Elaissari, A., *Colloidal Polymers: Synthesis and Characterization*. 2003: CRC Press.
143. Kudin, K.N., et al., *Raman Spectra of Graphite Oxide and Functionalized Graphene Sheets.* Nano Letters, 2008. **8**(1): p. 36-41.
144. Fang, M., et al., *Covalent polymer functionalization of graphene nanosheets and mechanical properties of composites.* Journal of Materials Chemistry, 2009. **19**(38): p. 7098-7105.
145. Das, A., B. Chakraborty, and A.K. Sood, *Raman spectroscopy of graphene on different substrates and influence of defects.* Bulletin of Materials Science, 2008. **31**(3): p. 579-584.

146. Jiang, D.-e., B.G. Sumpter, and S. Dai, *Unique chemical reactivity of a graphene nanoribbon's zigzag edge.* The Journal of Chemical Physics, 2007. **126**(13): p. 134701.
147. Salit, M.S., et al., *Manufacturing of Natural Fibre Reinforced Polymer Composites*. 2015: Springer International Publishing.
148. Velasco-Santos, C., et al., *Improvement of Thermal and Mechanical Properties of Carbon Nanotube Composites through Chemical Functionalization.* Chemistry of Materials, 2003. **15**(23): p. 4470-4475.
149. Dasari, A., Z.Z. Yu, and Y.W. Mai, *Polymer Nanocomposites: Towards Multi-Functionality*. 2016: Springer London.
150. Bautista-Quijano, J., et al., *Strain sensing capabilities of a piezoresistive MWCNT-polysulfone film.* Sensors and Actuators A: Physical, 2010. **159**(2): p. 135-140.
151. Fei, B., D.-L. Lu, and Q. Shen, *Formation of honeycomb polysulfone film with controlled wettability by surfactant-assisted electric breath figure.* Journal of Adhesion Science and Technology, 2017: p. 1-6.
152. Pinnau, I. and W.J. Koros, *Structures and gas separation properties of asymmetric polysulfone membranes made by dry, wet, and dry/wet phase inversion.* Journal of applied polymer science, 1991. **43**(8): p. 1491-1502.
153. Koehler, J.A., M. Ulbricht, and G. Belfort, *Intermolecular forces between a protein and a hydrophilic modified polysulfone film with relevance to filtration.* Langmuir, 2000. **16**(26): p. 10419-10427.
154. Black, J. and G. Hastings, *Handbook of Biomaterial Properties*. 1998: Springer US.
155. *Standard Terminology Relating to Plastics*.
156. Mitchell, P. and S.M. Engineers, *Tool and Manufacturing Engineers Handbook: Plastic Part Manufacturing*. 1996: Society of Manufacturing Engineers.
157. Cheremisinoff, N.P., *Condensed Encyclopedia of Polymer Engineering Terms*. 2012: Elsevier Science.
158. Dong, Y., R. Umer, and A.K.T. Lau, *Fillers and Reinforcements for Advanced Nanocomposites*. 2015: Elsevier Science.
159. Utracki, L.A. and R.T. Limited, *Clay-containing Polymeric Nanocomposites*. 2004: Rapra Technology Limited.
160. Bai, Y. and T. Keller, *High Temperature Performance of Polymer Composites*. 2014: Wiley.
161. Mozurkewich, M. and S.W. Benson, *Negative activation energies and curved Arrhenius plots. 1. Theory of reactions over potential wells.* The Journal of Physical Chemistry, 1984. **88**(25): p. 6429-6435.
162. Clugston, M. and R. Flemming, *Advanced Chemistry*. 2000: OUP Oxford.
163. Yan, C., et al., *Surface-induced anisotropic chain ordering of polycarprolactone on oriented polyethylene substrate: Epitaxy and soft epitaxy.* Macromolecules, 2006. **39**(23): p. 8041-8048.